Master's Thesis

Prospects of Sterile Neutrino Search with the FCC-*ee*

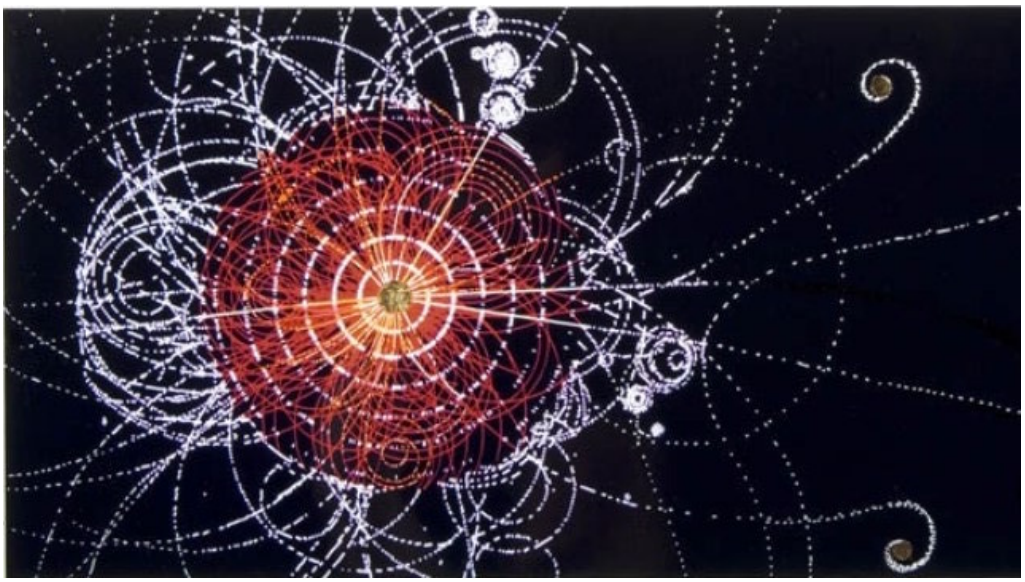

Sissel Bay Nielsen

"The important thing is not to stop questioning. Curiosity has its own reasons for existence. One cannot help but be in awe when he contemplates the mysteries of eternity, of life, of the marvelous structure of reality. It is enough if one tries merely to comprehend a little of this mystery each day. Never lose a holy curiosity."

- Albert Einstein, 1879-1955

Prospects of Sterile Neutrino Search with the FCC-*ee*

Author Sissel Bay Nielsen
Advisor Associate Professor Mogens Dam

A thesis submitted in fulfillment of the requirements for the degree of Master of Science in Physics

Research Group

Discovery - Center for Particle Physics

Niels Bohr Institute

Submitted to
the University of Copenhagen
December 10, 2017

Acknowledgements

First and foremost, I would like to give a huge thanks to my supervisor, Mogens Dam, for devoting an enormous amount of time and patience, guiding, teaching, and discussing with me. I am grateful that Mogens introduced me to the FCC-ee community, CERN and various conferences, and lastly for his honesty and humour - Mogens, it has been a pleasure to work with you.

I would like to give a great thanks to Oleg Ruchayskiy for his patience answering my questions regarding the theoretical aspects of the project, to Oliver Fischer for his help with WHIZARD, Alain Blondel for inspiring discussions, Colin Bernet for his help with PAPPAS, and to Troels Petersen for statistical advices. A great thanks to Peter Skands, who has been very helpfull with PYTHIA and guidance to implement matrix elements in PYTHIA.

I am grateful to have been part of the HEP group, who facilitates good discussions, a nice atmosphere and workspace, as well as financial support at conferences and trips. I would as well like to thank my office colleagues: Fabian, Morten and Simon, who always created a good atmosphere, and to Gorm for valuable inputs on the figures.

A warm thanks to both Kader and Lisbeth, who have always been helpful with researching literature at the library. I would also like to thank Solvej, Mikkel, Alexandra, and Erik for good laughs and talks at lunch, and to my prof-readers: Freja, Anine, Bjarke, Rosanna, Étienne, and Craig. A 'namaste' to Heather, my yoga teacher, for helping me keep my focus every day.

Lastly of course, I am very grateful for my friends, *Undergangen*: my corridor and bonus-family, Andreas, and my brother, mother, and father for being supportive throughout the last year.

Contents

Abstract

A proposed future circular e^+e^- collider, the FCC-ee, is suggested to search for sterile neutrinos. The Neutrino Minimal Standard Model, *νMSM*, is a model of sterile neutrinos, that accommodates explanations for several phenomena of physics beyond the Standard Model. This thesis presents an overview of the theoretical motivation for *νMSM*, an outline of the experimental conditions at the FCC-ee, and a review of previous accelerator bounds for sterile neutrinos.

Two studies of sterile neutrinos with masses at the electroweak scale are introduced, an analysis of long lived sterile neutrinos, and an analysis of short lived sterile neutrinos. Both analyses include background studies and sensitivity estimates for the FCC-ee detector.

The study of long lived sterile neutrinos is based on a search for detectable displaced vertices with 10^{12} Z decays, obtaining a search reach on the mixing angle $|\theta|^2$ as small as 10^{-11}. The study of short lived sterile neutrinos is a Monte Carlo study with a cut-based analysis, where a detector parametrisation of the FCC-ee detector, inspired by the CLIC detector design, is used. Background events were generated corresponding to a total number of $1.43 \cdot 10^8$ Z events, corresponding to a luminosity of $L = 3.33$ fb^{-1}. A search reach on the mixing angle with coupling to the muon neutrino on $|\theta_{\mu N}|^2 \sim 10^{-7} - 10^{-6}$ was achieved for sterile neutrino masses from 10 to 80 GeV.

CHAPTER 1

INTRODUCTION

THE present knowledge and understanding of the most fundamental substance of the Universe, elementary particles, and their interactions, are built on several decades of theoretical as well as experimental research. To give a profound review would require a study dedicated for the purpose, hence just few highlights are outlined.

The first discovered elementary particle, the electron, was measured in the end of the 19th century. In the early 1900s, quantum mechanics was born, and a new understanding of the atomic structure and its nature was established. In 1930 Pauli postulated the existence of the neutrino to explain the continuous energy spectrum in beta decays.[1] From around 1950 and onwards, an proliferation of new particles were discovered, including the electron neutrino. They were later organized in what is known as the Standard Model, a theoretical framework describing the elementary particles and their interactions, developed in the 1960s and 1970s. The Higgs boson predicted in the 1960s was discovered half a century later, in 2012 at CERN; the largest particle physics laboratory on earth, operated by a large international collaboration between many nations and thousands of scientists and engineers.

The Standard Model (the SM) has successfully been tested over time to a very high precision. It is outstanding in describing the observed elementary particles and their interactions, and has as well accomplished predicting phenomena and particles. However, the SM leaves unanswered questions, since it lacks explanations of well-established observed phenomena, such

[1] *"I have done a terrible thing, I have postulated a particle that cannot be detected."* - Wolfgang Pauli.

as dark matter, neutrino oscillations, and matter-antimatter asymmetry in the Universe, referred to as Baryon Asymmetry of the Universe (BAU).

Several extensions to the SM have been developed, each suggesting a solution to the yet not explained phenomena. This thesis has its focus on the Neutrino Minimal Standard Model, *νMSM*, which extends the SM by three right-handed heavy neutrinos (also called sterile neutrinos or heavy neutral leptons). The *νMSM* encompasses explanations of neutrino oscillations, dark matter, as well as the BAU.

A prior search for sterile neutrinos at masses higher than a few GeV was performed at the DELPHI experiment[1] at the former Large Electron Positron Collider (LEP) located at CERN, and those results are yet governing the best limit so far. A future 100 km long electron-positron collider, Future Circular Collider (FCC-ee), has been proposed to be built at CERN, followed by a high energy proton-proton collider (FCC-hh).

FCC-ee is planned to run as a high precision machine, following the treads of LEP, yet with many orders of magnitude higher statistics, which is reachable due to new technology. With this amount of statistics, very rare decays can be examined, such as sterile neutrinos.

This thesis presents a study of new hypothetical particles referred to as sterile neutrinos, in the proposed FCC-ee experiment. In the first part, a theoretical background is outlined followed by a description of the experimental conditions. The second part contains two analyses; a reproduced study of the FCC-ee detector sensitivity of detached vertices originated from sterile neutrino with long lifetime, and a Monte Carlo study of sterile neutrinos with short lifetime. The purpose of the Monte Carlo study is to estimate a limit for the FCC-ee sensitivity, and to gain a better estimated limit than the former established DELPHI limit.

Part I

THEORETICAL BACKGROUND OF STERILE NEUTRINOS AND EXPERIMENTAL CONDITIONS OF THE FCC-*ee*

CHAPTER 2

THEORETICAL BACKGROUND

In this chapter the Standard Model and its successes is introduced briefly to serve as background for the following presentation of the shortcomings of the model, since the introduction of sterile neutrinos mends some of these deficiencies. The Neutrino Minimal Standard Model, *νMSM*, and the predictions of the model is described and finally the phenomenology of the sterile neutrino is presented.

2.1 Standard Model

The Standard Model (SM) [2], [3], [4] is a model of the most fundamental substance of Nature, elementary particles and their interactions, tested to very high precision. The theoretical framework is based on quantum field theory with the underlying gauge groups $SU(3)\times SU(2)\times U(1)$. Elementary particles carry intrinsic quantum numbers such as electric charge, colour charge, weak isospin, and weak hypercharge. The SM incorporates an unified description of the electromagnetic and the weak force, which combined is referred to as the electroweak force. The electroweak symmetry is based on $SU(2) \times U(1)$, for which the weak isospin I_3, and the weak hypercharge Y_W are related by the electric charge $Q = I_3 + \frac{1}{2}Y_W$, which is always conserved. Colour charge is related to the strong interaction based on $SU(3)$, where particles are bound in so-called colourless states.

The SM describes three of the four known fundamental forces; the strong, the weak and the electromagnetic force mediated by the force carrying

particles, gauge bosons. Gravity is not described within the SM. The SM constitutes two type of particles: fermions, the matter particles, and bosons, the force-carrying particles. Every particle in the SM, is associated with an anti-particle of the same mass, but with opposite physical charge, except of the photon γ, the Z boson, and the Higgs boson, which are their own anti-particles.

The fermions, are spin-1/2 particles and are divided into two groups; leptons and quarks. Leptons inhere three charged leptons; the electron, e, the muon, μ, and the tau, τ, and three neutral leptons, the neutrinos with the corresponding flavours; ν_e, ν_μ, and ν_τ. All fermions, occur in three flavour families, or generations, each with left-handed $SU(2)$ doublets and right-handed $SU(2)$ singlets. An exception to this appears to be the neutrinos, which seem to occur only as left-handed. The first generation of fermions contains the up- and down-type quarks, u and d, the electron, e, and the electron neutrino, ν_e; grouped in the left-handed doublets $(u, d)_L$ and $(e, \nu_e)_L$ and the right-handed singlets $u_R,\ d_R,\ e_R$, with ν_R left out. Here L and R refers to the left- and right-handed components, or the left- and right-handed chiral states, obtained by the chiral projection operator acting on a Dirac wave function ψ, by:

$$\psi_{R,L} = P_{R,L}\psi = \frac{1 \pm \gamma^5}{2}\psi \tag{2.1}$$

The distinction arise from the experimental evidence, that the charged current interaction, mediated by the W-boson, exclusively couples to left-handed (LH) particles and right-handed (RH) anti-particles. The fermions, their charge, spin and masses are listed in table 2.1. The limits on neutrino masses in table 2.1 are based on direct measurements and do not include data on neutrino oscillations.

The leptons, electrons, muons and taus, with their respective neutrinos, all interact via the weak interaction, mediated by the Z- and W-boson. All leptons, except the neutrinos, interact electromagnetically governed by quantum electro dynamics (QED), mediated by the photon, γ. All quarks; u, d, c, s, t, b carry colours, red, green, blue. Anti-quarks carry anti-colours. Quarks interact both via the electromagnetic force, the weak force, and via the strong force, which is governed by quantum chromo dynamics (QCD), and mediated by the eight gluons, g. As for the quarks, the gluons carry colour charge, which is why the gluon is self-interacting contrary to the photon. The strong coupling constant, α_s, decreases as energy increases, known as asymptotic freedom. The opposite phenomena, when energy decreases causes an increase of α_s, and is defined as colour confinement. Due to colour confinement, quarks are bound in colourless states called

hadrons, which include mesons (quark-anti-quark pairs, $q\bar{q}$) and baryons (qqq or $\bar{q}\bar{q}\bar{q}$). Hadronization is the process of hadron formation, which in high-energy processes produces jets; tight cones of particles created by hadronization.

All fermions (leptons and quarks) interact with the Higgs boson, and the couplings are proportional to the fermion mass. The Higgs boson is an excitation of the Higgs field, which is responsible for the fermion masses as well as the mass of the Z- and W- boson, through spontaneous symmetry breaking. All force carrying particles, and the Higgs boson are listed, with their charge, spin and mass in table 2.2.

Helicity is an important property in the SM, since the SM distinguish between LH and RH particles. Helicity describes whether a particle's spin and momentum are in same direction, defined by: $h \equiv \frac{\boldsymbol{s}\cdot\boldsymbol{p}}{p}$. If momentum and spin are in the same direction, the helicity is positive, if momentum and spin are pointing in opposite directions, the helicity is negative. For particles with mass, helicity is not Lorentz invariant, since a change of reference frame can make the particle move, relatively, in the opposite direction. Hence helicity depends on the reference frame, while chirality does not and is thereby Lorentz invariant. For massless particles, and in the $E \gg m$ limit, helicity corresponds to chirality, causing positive helicity equate RH chirality, whereas negative helicity equate LH chirality. Chirality is defined through the projection operator in equation 2.1, with eigenvalues on ± 1. It is related to weak isospin, with fractional isospin associated with negative chirality (LH particles), and zero weak isospin associated with positive chirality (RH particles) [5].

2.1.1 Conserved Quantities in the SM

A number of quantities are observed to be conserved within the SM. Violations of such conservations are in general sought, since it would be an evidence of physics beyond the SM.

The SM accommodates a number of symmetries which each associate to a conserved quantity, due to Noether's theorem[1]. In every interaction, the energy, momentum, and angular momentum are conserved as well as the quantum numbers; Q, L, B, and I; electric charge, lepton number for each lepton flavour, baryon number and weak isospin, respectively. The symmetry CP, the combination of charge conjugation C with parity transformation P, is conserved for strong and electromagnetic processes,

[1] E.g. translation symmetry correspond to momentum conservation and time invariance correspond to energy conservation.

Particle name	Symbol	EM charge	Spin	Mass [MeV]
electron	e	-1	1/2	0.511
electron neutrino	ν_e	0	1/2	$< 2.2 \cdot 10^{-6}$
muon	μ	-1	1/2	106
muon neutrino	ν_μ	0	1/2	< 1.7
tau	τ	-1	1/2	1777
tau neutrino	ν_τ	0	1/2	< 15.5
up	u	+2/3	1/2	~ 2.3
down	d	$-1/3$	1/2	~ 4.8
charm	c	+2/3	1/2	$\sim 1.3 \cdot 10^3$
strange	s	$-1/3$	1/2	~ 95
top	t	+2/3	1/2	$\sim 173 \cdot 10^3$
bottom	b	$-1/3$	1/2	$\sim 4.2 \cdot 10^3$

Table 2.1: The matter particles of the Standard Model with their charge, spin, and mass [6].

Particle name	Symbol	EM charge	Spin	Mass [GeV]
photon	γ	0	1	0
Z-boson	Z^0	0	1	91.19
W-boson	$W^\pm$	± 1	1	80.39
gluon	g	0	1	0
Higgs boson	H^0	0	0	125

Table 2.2: The force particles and the Higgs boson of the Standard Model with their charge, spin, and mass [6].

but is violated for some weak interactions, for instance in K^0-decays. The symmetry CPT, the combination of CP with time reversal T, has only been observed as a conserved quantity.

2.1.2 Successes of the SM

The SM constitutes a complete theory from a theoretical point of view. High precision measurements performed so far show that it is also a consistent theory, which is summarised in figure 2.1.

Via precision measurements of the electroweak parameters of the Z-boson, the mass of the W, top, and Higgs can be predicted. The

properties of the Z boson, such as its width and couplings measured through asymmetries, etc., are affected via loop corrections. Those loop corrections are especially affected by the top mass, and to some extend by the Higgs mass. The weak mixing angle θ_W, measured via asymmetries, are connected to the W mass by the relation $m_W = m_Z \cos(\theta_W)$.

The predictions and measurements are consistent within two standard deviations as shown in figure 2.1, where the predictions of the W, top and Higgs mass are confined within the grey circles, and the green areas shows the direct measurements of the top and W mass. The measurement of the Higgs-boson at $m_H = 125$ GeV, confines the circles to the blue area. This puts constraints on new physics. If new particles exists they must either be very heavy or be an extension to the model that only minimally affect loop corrections of the Z-boson, such as e.g. sterile neutrinos.

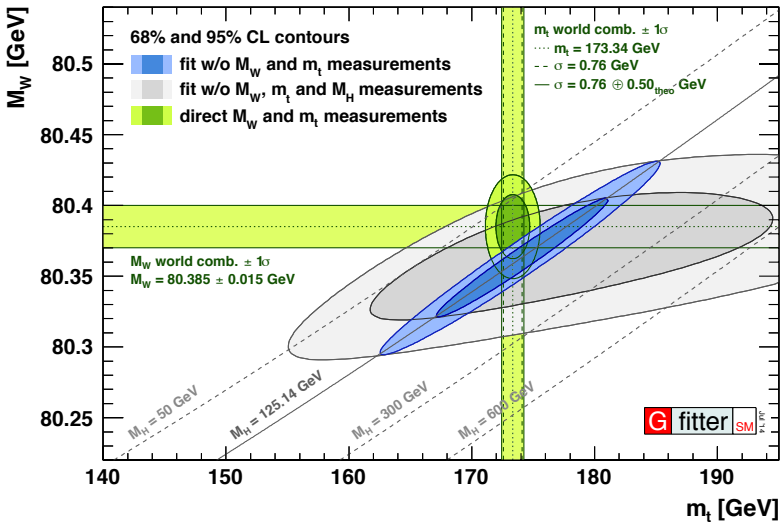

Figure 2.1: Direct measurements of the top and W mass (green areas). The grey area shows indirect constrains of m_t, m_W, and m_H obtained from measurements of electroweak parameters of the Z boson. The Higgs mass measurement confines the constraints to the blue area [7].

2.1.3 Shortcomings of the Standard Model

The SM excels in numerous predictions and measurements, and yet no measurement from the laboratory is inconsistent with the SM. However, a number of observed phenomena in both astro-physics, astro-particle-

physics, and cosmology remain unexplained by the SM, some of them are listed here. The experimental observation of neutrino oscillations[8] require the neutrinos to be massive, and imply that lepton flavour numbers are not conserved for each flavour individually, is a clear manifestation of physics beyond the SM. The origin of Dark Matter [9], the observed excess of non-luminous, non-absorbing matter, is not included in the SM. And lastly, the relatively small degree of *CP*-violation in the Standard Model is not adequate to explain the large excess of matter over anti-matter in the Universe, refered to as Baryon asymmetry in the Universe [10].

2.2 Active Neutrinos

From measurements of charged current (CC) interactions, it has been determined, that the CC exclusively couples to left-handed particles and right-handed anti-particles, which is why a right-handed neutrino was not introduced when the SM was formulated. Hence the neutrinos were thought to be massless.[2]

In the 1970s a deficit was found by the Homestake experiment [11] between the flux of the measured electron-neutrinos from the sun and the predicted flux, which is known as the solar neutrino problem. Neutrino experiments before SNO [8] were only sensitive to ν_e interacting via charged current interactions, while the SNO experiment was sensitive to the sum of neutrino flavours interacting via neutral current interactions. The total neutrino flux from the sun, consistent with the predicted flux, was thus later measured by SNO. In 1998 the oscillation of atmospheric neutrinos was measured with a deficit of ν_μ, indicating oscillations of ν_μ into ν_τ [12]. The measurements of solar and atmospheric neutrino oscillations were later confirmed by accelerator [13] and reactor experiments [14].

Oscillations of neutrinos imply that the neutrinos are massive and mixed particles. The probability of a neutrino to oscillate into another flavour is dependent on the mixing angle θ, the mass difference of the mass eigenstates, the oscillation length L, and the neutrino energy E_ν. The probability of oscillations from ν_e to ν_μ is[3] [5]

[2]Fermions acquire mass by the Dirac mass term, that mixes left and right chiral fermions.

[3]The expression is valid for the case of two neutrino generations only, and is here chosen in order to simplify the cumbersome expression for oscillations with tree neutrino generations.

$$P(\nu_e \to \nu_\mu) = \sin^2(2\theta)\sin^2\left(\frac{(m_1^2 - m_2^2)L}{4E_\nu}\right) \tag{2.2}$$

In order to oscillate, neutrinos need to 'sense' time and space, which only massive particles are capable of.

In the minimal case when there are only three mass eigenstates, neutrino oscillations are transitions between the flavour eigenstates, ν_e, ν_μ, and ν_τ propagating via the mass eigenstates; ν_1, ν_2, and ν_3 with the mixing parametrised in the 3×3 PMNS matrix:

$$\begin{pmatrix} \nu_e \\ \nu_\mu \\ \nu_\tau \end{pmatrix} = \begin{pmatrix} U_{e1} & U_{e2} & U_{e3} \\ U_{\mu 1} & U_{\mu 2} & U_{\mu 3} \\ U_{\tau 1} & U_{\tau 2} & U_{\tau 3} \end{pmatrix} \begin{pmatrix} \nu_1 \\ \nu_2 \\ \nu_3 \end{pmatrix}. \tag{2.3}$$

The PMNS matix can be parametrised by [15]:

$$U_{PMNS} = \begin{pmatrix} c_{12}s_{13} & s_{12}c_{13} & s_{13}e^{-i\delta_{CP}} \\ -s_{12}c_{23} - c_{12}s_{23}s_{13}e^{i\delta_{CP}} & -c_{12}s_{23} - s_{12}c_{23}s_{13}e^{i\delta_{CP}} & s_{23}c_{13} \\ s_{12}c_{23} - c_{12}s_{23}s_{13}e^{i\delta_{CP}} & -c_{12}s_{23} - s_{12}c_{23}s_{13}e^{i\delta_{CP}} & c_{23}c_{13} \end{pmatrix} \tag{2.4}$$

$$\times \text{diag}(1, e^{i\alpha_{21}/2}, e^{i\alpha_{31}/2}), \tag{2.5}$$

where c_{ij} and s_{ij} denote $\cos(\theta_{ij})$ and $\sin(\theta_{ij})$, respectively, with θ_{12}, θ_{13}, and θ_{23} being the three mixing angles, δ_{CP} is a CP-violating phase, and α_{21}, α_{31} represent potential Majorana phases, with the current measurements [15] listed in table 2.3.

Parameter	best-fit	3σ
$\sin^2\theta_{12}$	0.217	0.250-0.354
$\sin^2\theta_{23}$	0.437	0.379-06.16
$\sin^2\theta_{13}$	0.0214	0.0185-0.0246
δ_{CP}/π	1.35	0.92-1.99

Table 2.3: Current measurement of the mixing angles and CP-violating phase of the PMNS matrix [15].

The oscillations occur due to the mass difference of the mass eigenstates, but since only the absolute value of the difference of the squared masses can be derived from the measurements, it results in an undetermined mass hierarchy. Two mass hierarchies are possible, normal mass hierarchy and inverted mass hierarchy, which are sketched in figure 2.2.

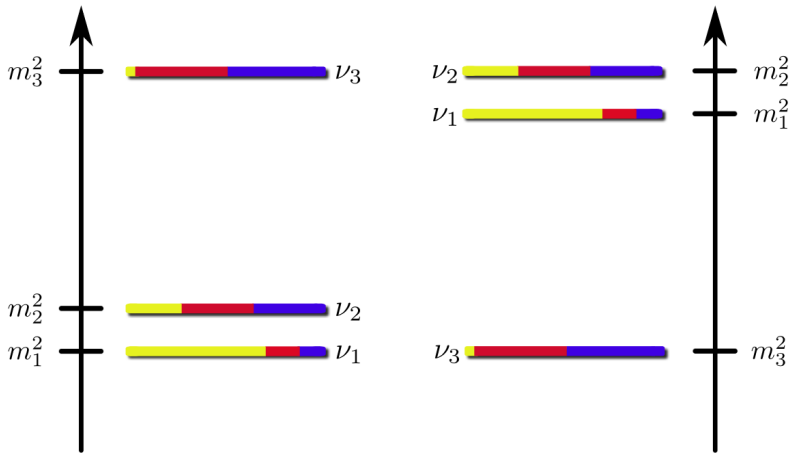

Figure 2.2: The two possible neutrino mass hierarchies, normal to the left and inverted to the right. Yellow indicates the ν_e flavour eigenstate, red the ν_μ flavour eigenstate, and blue the ν_τ flavour eigenstate. The size of the colour box is proportional to $|U_{\alpha i}|^2$ with $\alpha = e, \mu, \tau$ and $i = 1, 2, 3$ [16].

The current measured mass differences between the propagation states are [15]

$$\Delta m^2_{21} = (7.53 \pm 0.18) \cdot 10^{-5}\ \text{eV}^2, \tag{2.6}$$

$$\Delta m^2_{32} = (2.45 \pm 0.05) \cdot 10^{-3}\ \text{eV}^2. \tag{2.7}$$

where the value of Δm^2_{21} comes from measurements of neutrinos coming from the sun, and Δm^2_{32} from the atmospheric neutrinos. The quoted value for Δm^2_{32} is under the assumption of normal mass hierarchy. With inverted mass hierarchy, the value is $\Delta m^2_{32} = (2.52 \pm 0.05) \cdot 10^{-3}$ eV.

Since measurements of neutrino oscillations only are sensitive to the mass differences squared, the absolute mass scales of the neutrinos are unknown. However, measurements from the Planck satellite obtained a constraint on the sum of the neutrino masses of $\sum_i m_i < 0.23$ eV, indicating the smallness of the neutrino masses.[17].

The number of light neutrino generations were measured by LEP [18] via the invisible width of the Z-boson. The number of neutrino generations were determined via the invisible width of the Z, that was measured by the total width of the Z, when assuming lepton universality. The result is shown in figure 2.3 and found by the relation:

$$N_\nu = \left(\frac{\Gamma_{\text{inv}}}{\Gamma_{\text{lept}}}\right)^{\text{meas}} \Big/ \left(\frac{\Gamma_{\nu\bar{\nu}}}{\Gamma_{\text{lept}}}\right)^{\text{SM}}, \tag{2.8}$$

with a value of

$$N_\nu = 2.9840 \pm 0.0082 \quad [18]. \tag{2.9}$$

N_ν can be observed to be almost two standard deviations below the integer number three, a likely insignificant, but interesting deficit in the expected direction due to suppression, if sterile neutrinos are present, as pointed out in [19].

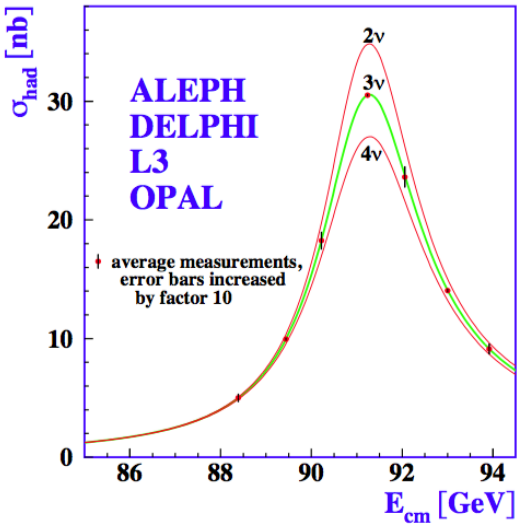

Figure 2.3: Number of neutrino generations N_ν measured via the total width of the Z boson by LEP [18].

2.3 Sterile Neutrinos

The addition of right handed neutrinos is an elegant and simple extension to the Standard Model [20] [21]. All fermions in the SM, except the neutrino, have a left-handed and a right-handed component, which is illustrated in figure 2.4 to the left, and with the implemented sterile neutrinos to the right. The right-handed neutrino has zero electric, weak and colour charge, which is why it is also called sterile. Thereby it only interacts via

the Yukawa coupling to the Higgs field[4] and the active neutrinos. Several right-handed neutrino models have been developed, proposing masses of the right-handed neutrino all the way from eV-scale up to GUT-scale (10^{16} GeV). The Neutrino Minimal Standard Model, *vMSM* [22], is a right-handed neutrino model restricted by certain constrains giving rise to a set of parameters. The *vMSM* accommodate a number of shortcomings of the SM, such as the unexplained neutrino masses, dark matter, and the baryon asymmetry of the Universe, and shares all its successes. The model describes sterile neutrinos with masses below the electro-weak scale. In the following sections, first a general implementation of right-handed neutrinos and the Seesaw mechanism are introduced, followed by an introduction to the *vMSM*.

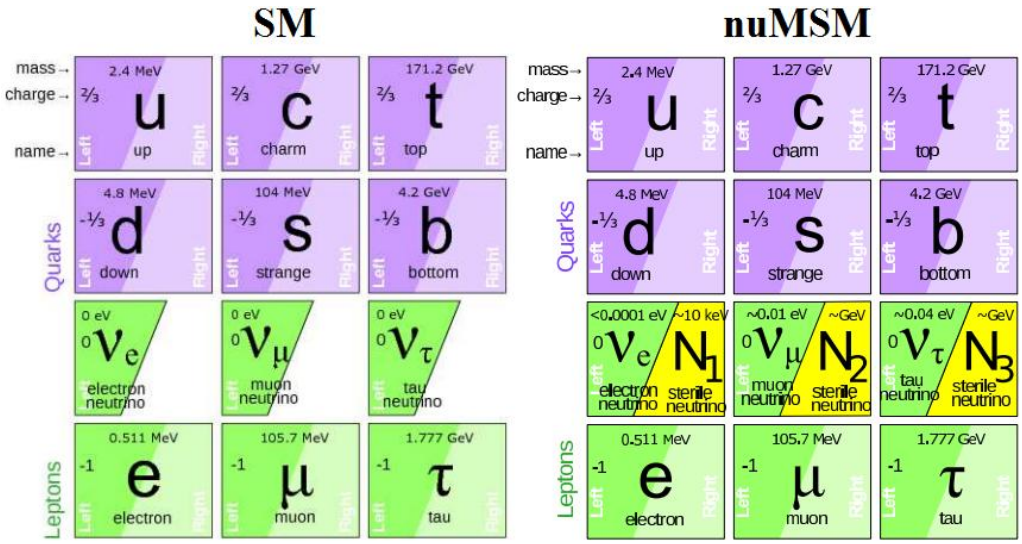

Figure 2.4: SM vs. *vMSM*, with and without right-handed neutrinos [23].

2.3.1 Introducing one Sterile Neutrino

In this section one sterile neutrino is introduced as an extension to the SM. The discussion is based on [24]. In the SM, neutrinos are implemented as massless particles with the left-handed neutrino fields exclusively. A Dirac mass term can be generated through the standard Higgs mechanism introducing a right-handed neutrino field, this breaking the SM

[4]The right-handed neutrino only couples to the Higgs field via its Dirac mass term.

assumption. For simplicity only one neutrino field is considered at first, $\nu = \nu_L + \nu_R$, with the Dirac mass term:

$$\mathcal{L}^D = -m_D \bar{\nu}\nu = -m_D(\overline{\nu_R}\nu_L + \overline{\nu_L}\nu_R) \tag{2.10}$$

where $m_D = yv/\sqrt{2}$, with y being the dimensionless Yukawa coupling, and $v = 246$ GeV the vacuum expectation value of the Higgs field. The chiral left-handed and right-handed neutrino fields, ν_L and ν_R, are obtained by acting on ν with the chiral projecting operators, P_L and P_R, defined in equation 2.1, implying $P_L\nu_L = \nu_L$, $P_R\nu_R = \nu_R$, and $P_L\nu_R = P_R\nu_L = 0$.

The Dirac mass term cannot explain naturally the smallness of the neutrino mass compared to that of the electron, the lightest of the other fermions, which is why the possibility of a Majorana mass term is explored.

The Majorana condition, ($\psi = \psi^C$) implies that a spinor, denoted by ψ, is equivalent to its charge conjugate, meaning that a Majorana particle is its own antiparticle. A general Majorana field can then be written as $\psi = \psi_L + \psi_L^C$.

Acting with the projecting operators on the Majorana neutrino fields, yield: $P_L\nu_L^C = 0$, $P_L\nu_R^C = \nu_R^C$, $P_R\nu_R^C = 0$, and $P_R\nu_L^C = \nu_L^C$. Which means that ν_R^C is left-handed and ν_L^C right-handed.

If both the left-handed and right-handed chiral fields exist and are independent, a Majorana mass term is allowed for the neutrino field ν_R and is obtained using the Majorana condition in the mass term from equation (2.10)

$$\mathcal{L}_R^M = -\frac{1}{2} m_M(\overline{\nu_R^C}\nu_R + \overline{\nu_R}\nu_R^C), \tag{2.11}$$

with the Majorana mass, m_M, and a factor 1/2 to account for double counting, since the hermitian conjugate is the same.

Then a combined Dirac-Majorana mass term can be written as

$$\begin{aligned} \mathcal{L}^{D+M} &= \mathcal{L}^D + \mathcal{L}_R^M & (2.12)\\ &= \frac{1}{2}\begin{pmatrix}\overline{\nu_L^C} & \overline{\nu_R}\end{pmatrix}\begin{pmatrix}0 & m_D\\ m_D & m_M\end{pmatrix}\begin{pmatrix}\nu_L\\ \nu_R^C\end{pmatrix} + h.c., & (2.13)\end{aligned}$$

where h.c. denotes the hermitian conjugate. In order to find the fields with definite masses, the matrix must be diagonalised. It is convenient to rewrite the expression as

$$\mathcal{L}^{D+M} = \frac{1}{2}\overline{N_L^C} M N_L + h.c., \tag{2.14}$$

where $M = \begin{pmatrix} 0 & m_D \\ m_D & m_M \end{pmatrix}$ and $N_L = \begin{pmatrix} \nu_L \\ \nu_R^C \end{pmatrix}$.

The left-handed field, N_L, can be written in terms of the vector n_L containing the mass eigenstates and a unitary matrix U

$$N_L = U n_L, \quad \text{with} \quad n_L = \begin{pmatrix} \nu_{1,L} \\ \nu_{2,L} \end{pmatrix}, \tag{2.15}$$

where U is chosen such that M gets diagonalized:

$$U^T M U = \begin{pmatrix} m_1 & 0 \\ 0 & m_2 \end{pmatrix}. \tag{2.16}$$

Considering a real mass matrix, the mixing matrix U can be written as a product of two orthogonal matrices $U = O\rho$, which

$$O = \begin{pmatrix} \cos\theta & \sin\theta \\ -\sin\theta & \cos\theta \end{pmatrix}, \quad \rho = \begin{pmatrix} \rho_1 & 0 \\ 0 & \rho_2 \end{pmatrix}, \tag{2.17}$$

where θ is the the mixing angle between the active and sterile neutrino field. O is chosen such that

$$O^T M O = \begin{pmatrix} m'_1 & 0 \\ 0 & m'_2 \end{pmatrix} \tag{2.18}$$

and the phase, $\rho_k^2 = \pm 1$, $k = 1, 2$, is chosen to insure that the masses are positive

$$U^T M U = \begin{pmatrix} \rho_1^2 m'_1 & 0 \\ 0 & \rho_2^2 m'_2 \end{pmatrix}. \tag{2.19}$$

This leads to

$$\tan(2\theta) = \frac{2m_D}{m_M}, \qquad m'_{2,1} = \frac{1}{2}\left(m_M \pm \sqrt{m_M^2 + 4m_D^2}\right). \tag{2.20}$$

The diagonalised Dirac + Majorana mass term then becomes

$$\mathcal{L}^{D+M} = \frac{1}{2}\sum_{k=1,2} m_k \overline{\nu_{kL}^C} \nu_{kL} + h.c., \tag{2.21}$$

which is a sum of Majorana mass terms for the massive Majorana neutrino fields

$$\nu_k = \nu_{kL} + \nu_{kL}^C, \quad k = 1, 2. \tag{2.22}$$

The most plausible and interesting case of parameter choice is the Seesaw mechanism, where $|m_D| \ll m_M$. In this limit the expression in equation (2.20) becomes

$$m'_{2,1} \approx \frac{1}{2}\left(m_M \pm (m_M + 2\frac{m_D^2}{m_M})\right), \tag{2.23}$$

which leads to the expressions for the three parameters

$$m_1 \approx \frac{m_D^2}{m_M} \ll |m_D|, \qquad m_2 \approx m_M, \qquad \tan\theta \approx \frac{m_D}{m_M} \ll 1. \tag{2.24}$$

In the Seesaw mechanism, m_1 thereby gets suppressed by the small ratio m_D/m_M. Since m_M and m_2 are of the same order, a heavy ν_2 then corresponds to a light ν_1. The Dirac mass, m_D, is expected to be generated through the standard Higgs mechanism, and is presumed to be of the same order as the masses of other fermions in the given generation, whereas the Majorana mass, m_M, is a free parameter.

For very small mixing angles, the neutrino fields can be identified as $\nu_{1,L} \approx -\nu_L$ and $\nu_{2,L} \approx \nu_R^C$ obtained from equation (2.15). This implies that the ν_1 is practically the active neutrino participating in weak interactions, whereas the ν_2 is a heavy neutrino practically decoupled from interactions with matter.

2.3.2 Introducing three Sterile Neutrinos

Introducing three sterile neutrinos to the SM is more cumbersome, but in its essence the same principle as in the previous section, and hence not described as much in detail.

The three active neutrino fields are now denoted $\nu_{eL}, \nu_{\mu L}, \nu_{\tau L}$ and the sterile neutrino fields, $\nu_{s_1 R}, \nu_{s_2 R}, \nu_{s_3 R}$. The corresponding Dirac and Majorana mass term can be written

$$\mathcal{L}^D = -\sum_{s,\beta} \overline{\nu_{sR}} M^D_{s\beta} \nu_{\beta L} + h.c., \tag{2.25}$$

$$\mathcal{L}^M_R = -\frac{1}{2}\sum_{s,s'} \overline{\nu^C_{sR}} M^R_{s,s'} \nu_{s'R} + h.c.. \tag{2.26}$$

In the same way as in equation (2.14) the terms can be written in one Lagrangian with

$$N_L = \begin{pmatrix} \nu_L \\ \nu_R^C \end{pmatrix}, \quad \text{where} \quad \nu_L = \begin{pmatrix} \nu_{eL} \\ \nu_{\mu L} \\ \nu_{\tau L} \end{pmatrix}, \quad \text{and} \quad \nu_R^C = \begin{pmatrix} \nu_{s_1 R}^C \\ \nu_{s_2 R}^C \\ \nu_{s_3 R}^C \end{pmatrix}, \tag{2.27}$$

and with the 6×6 matrix $M = \begin{pmatrix} 0 & (M^D)^T \\ M^D & M^R \end{pmatrix}$, with M^D and M^R being 3×3 matrices representing the Dirac mass matrix and the sterile mass matrix, respectively.
As for the example with only one neutrino field, the matrix gets diagonalised resulting in a mass matrix

$$M' = \begin{pmatrix} M_{light} & 0 \\ 0 & M_{heavy} \end{pmatrix}. \tag{2.28}$$

The matrix U used to diagonalise M' includes the standard PMNS matrix with mixing of the active neutrinos, and the mixing angles $\theta_{\alpha,i}$ with $\alpha = e, \mu, \tau$ and $i = s_1, s_2, s_3$ that mixes the sterile neutrinos with the active neutrinos.

2.3.3 *νMSM*

The *νMSM* is a minimal extension to the SM that constrains three right-handed, sterile neutrinos with masses below the electro-weak scale.

To explain the phenomena of neutrino oscillations, the number of implemented singlet neutrinos must be $N \geq 2$. It turns out that the same two sterile neutrinos that are responsible for the neutrino oscillations, can generate Baryon asymmetry of the universe, if their masses are below that of the W boson and very close to each other [10], [25]. Both neutrino oscillations and dark matter can be accounted for by the model if $N = 3$. With three sterile neutrinos, the lightest is favoured as a Dark Matter candidate. With three sterile neutrinos, the symmetry between the quarks and leptons can be restored: For every left-handed fermion there will be a right-handed counterpart. For the sterile neutrino to be a dark matter candidate, the mass is restricted to the keV range and the lifetime has to be greater than the age of the Universe, and this restricts the mixing angle. For that reason it cannot contribute to the active neutrino mass matrix, which is why three sterile neutrinos are needed to account for both neutrino oscillations and Dark Matter [25].

For $N = 2$ the number of free parameters is 11, with 2 Majorana masses, 2 Dirac Masses, 4 mixing angles and 3 CP violating phases. If $N = 3$, 18 free parameters are obtained with 3 Majorana masses, 3 Dirac Masses, 6 mixing angles and 6 CP violating phases [25].

Dark Matter

The observed anomaly between the amount of visible matter and the rotation of galaxies, has lead to the introduction of Dark Matter (DM); a substance non-luminous and non-absorbing, only interacting through gravity, thus the name. The constituents of DM are still unknown, and a number of hypothetical candidates have been proposed, such as Weakly Interacting Massive Particles (WIPMs) and Axions [9]. If three sterile neutrinos exist, one of the singlet fermions in *νMSM* could thus be a DM candidate.

Baryon asymmetry in the Universe

Baryon asymmetry of the Universe (BAU) refers to the imbalance between observed baryonic matter and anti-baryonic matter in the Universe. Its origin is still unknown, since the Standard Model *CP*-violation, cannot explain the extent of the observed asymmetry [10].
In the *νMSM*, the BAU can be explained by the *CP*-violating oscillations of sterile neutrinos in the early Universe. At the electroweak epoch, these oscillations created the asymmetry in the left- and right-handed lepton sector. The asymmetry in the left-handed sector was converted into the baryon asymmetry via processes known as sphalerons[5] [25].

Predictions from νMSM

In order to make a theory testable, it needs to make predictions. Four predictions of the *νMSM* are presented here [25]. Firstly, the Higgs boson was predicted in the mass interval [126;194] GeV, and was discovered in 2012 at LHC [26] [27] within the theoretical uncertainty from [28]. Secondly, one of the active neutrinos must be very light $m_1 \lesssim O(10^{-6})$ eV. This fixes the other two active neutrino masses to $m_2 \simeq 9 \cdot 10^{-3}$ eV and $m_3 \simeq 5 \cdot 10^{-2}$ eV for normal hierarchy and $m_{2,3} \simeq 5 \cdot 10^{-2}$ eV for inverted hierarchy, in agreement with equation (2.6) and (2.7). Thirdly, an effective Majorana mass for neutrinoless double decay can be determined. For normal hierarchy the constraints are 1.3 meV $< m_{\beta\beta} <$ 3.4 meV and for

[5]Sphalerons are a saddle point solution to the electroweak field equation.

inverted hierarchy: 13 meV $< m_{\beta\beta} <$ 50 meV. And lastly, negative results in direct and indirect search for weakly interacting massive particles, proton decay, neutron oscillations, and extra sources of *CP*-violation in the hadronic sector. So far the predictions are in agreement with the observations.

If all predictions holds it supports the existence of sterile neutrinos. In order to verify the model, an observation of a sterile neutrino is required.[6]

2.4 Physics of the Sterile Neutrino

The two main parameters of a search for sterile neutrinos is the mixing angle between active and sterile neutrinos and its mass, M_N. For this study the masses of interest of the sterile neutrino are at the electroweak scale, specifically between 10 and 80 GeV. The specific coupling between the active neutrino flauvors and the sterile neutinos states is denoted by $\theta_{i,j}$, with $i = e, \mu, \tau$, and $j = 1, 2$, corresponding to the sterile neutrinos, where the third sterile neutrino is assumed to be the dark matter candidate why it couples very weakly to the active neutrinos as pointed out above [29]. The parameter $|\theta|^2 = \sum_{i,j} \theta^2_{i,j}$ denotes the sum of squares of all mixing angles.
Through mixing withing the active neutrino, the sterile neutrino can be produced from *Z*, *W*, or Higgs-boson decays [29] and is shown in figure 2.5 in production from a *Z* boson. For this study, the focus is on a sterile neutrino produced from a *Z*-boson.

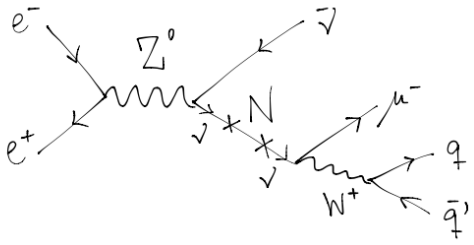

Figure 2.5: Feynman diagram of the process $Z \to \bar{\nu}N$ where N decays via $N \to \mu^- q\bar{q}'$. The sterile neutrino is produced and decays through mixing with an active neutrino.

[6] *"Science walks forward on two feet, namely theory and experiment... but continuous progress is only made by the use of both" (- Robert A. Millikan).*

The decay width of $(Z \to \nu_i N_j)$ is [29]:

$$\Gamma(Z \to \bar{\nu}_i N_j) = |\theta_{ij}|^2 \cdot \Gamma(Z \to \nu_i \bar{\nu}_i) \cdot \Pi\left(\frac{M_N}{m_Z}\right) \tag{2.29}$$

$$= |\theta_{ij}|^2 \cdot \frac{G_F m_Z^3}{3\sqrt{2}\pi} \cdot \Pi\left(\frac{M_N}{m_Z}\right), \tag{2.30}$$

where G_F is the Fermi coupling constant, and the indices $i = e, \mu, \tau$, $j = 1, 2$. The charge conjugated is taken into account, implying that equation (2.30) includes both the decays $Z \to \bar{\nu}_i N_j$ and $Z \to \nu_i \bar{N}_j$ and is thereby a factor two larger than the expression for $\Gamma(Z \to \bar{\nu}_i N_j)$ in [29], that exclusively includes the process $Z \to \bar{\nu}_i N_j$. The phase space factor is given by

$$\Pi\left(\frac{M_N}{m_Z}\right) = \frac{1}{2}\left(1 - \left(\frac{M_N}{m_Z}\right)^2\right)^2 \left(2 + \left(\frac{M_N}{m_Z}\right)^2\right). \tag{2.31}$$

The sterile neutrino can decay through the same channels as they can be produced, via mixing with the active neutrino and decaying through the Z and W bosons or via the Higgs-boson. The approximate branching ratios have a small dependence on mass, at masses above 10 GeV and below the m_W as shown in figure 2.6 for the different final states. The mass dependence is disregarded in the practical application in this study.

In the first study long lived sterile neutrinos are investigated and is elaborated in chapter 5. In this study, all possible decay modes of the sterile neutrino are taken into account. In the second study investigating short lived sterile neutrinos, only fully visible decays with the decay products $\mu^{\pm} q\bar{q}$, where the sterile neutrino is decaying through a hadronic W-decay associated with a muon, are taken into account, as shown in the Feynman diagram in figure 2.5.[7] For this study, elaborated in chapter 6, the branching ratio of relevance is for a sterile neutrino decaying via a W with a hadronic decay, denoted "quarks, CC" in figure 2.6, and has a value of

$$BR(N \to \ell^{\pm} q\bar{q}') \simeq 50\%. \tag{2.32}$$

A possible signature of a visible decay from a sterile neutrino with a detached vertex, is characterised by a mono-jet signature associated with a muon, which are recoiling against an active neutrino, as in figure 2.7.

[7] Throughout this study, when the process $N \to \mu^- q\bar{q}'$ is described, it holds as well for the charged conjugated process and for all possible quark decays according to the CKM-matrix.

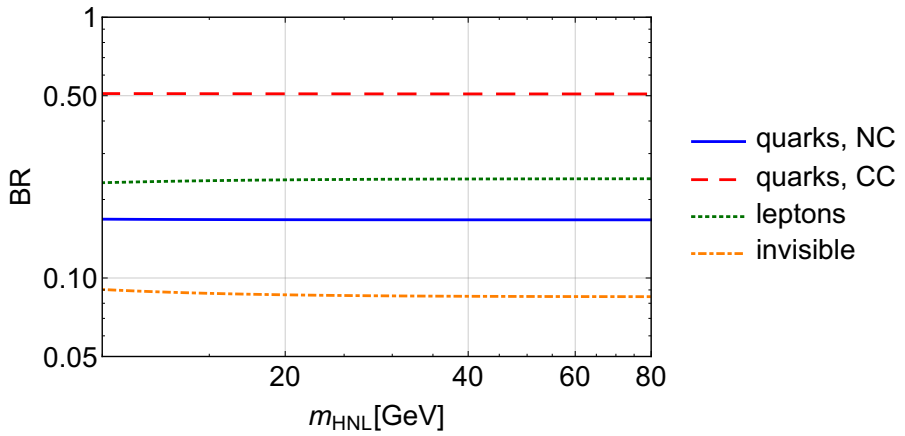

Figure 2.6: Branching ratios (BR) of sterile neutrino decays calculated by Oleg Ruchayskiy. BR of final state quarks decaying from neutral current (Z^0) in fully drawn blue, and from charged current ($W^{\pm}$) in dashed red. BR of a fully leptonic decay dotted in green, and invisible decays dotted in orange. The Branching ratios have a slight mass dependence due to the phase space.

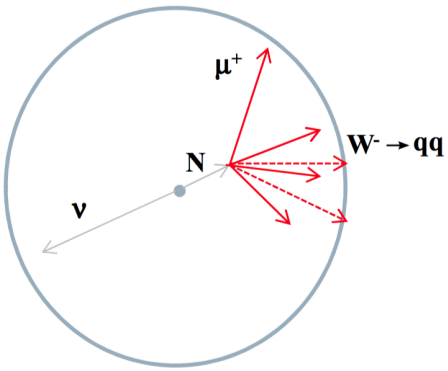

Figure 2.7: Signature of a sterile neutrino decaying fully visible with a detached vertex in production from a Z boson [30].

A power-law approximation of the lifetime of the sterile neutrino which is coupling to the muon neutrino, τ_μ, used later in this study, is derived in [31] for masses below m_W:

$$\tau_\mu = \frac{4.49 \cdot 10^{-12}}{|\theta|^2} \left(\frac{\text{GeV}}{M_N}\right)^{5.19} \text{s.} \tag{2.33}$$

Chapter 3

Experimental Conditions of the FCC-*ee*

The Future Circular Collider (FCC) project is a long term accelerator project proposed at CERN (Conseil Européen pour la Recherche Nucléaire) at the Swiss-French boarder, as shown in figure 3.1. With a circumference of 100 km, it is proposed as a two stage project, a potential initial step of an electron-positron collider (FCC-ee) mainly for precision measurements of electroweak parameters including Higgs properties, and an ultimate goal of a proton-proton collider (FCC-hh) aiming with a collision energy of 100 TeV aiming at direct discoveries of new phenomena at very high mass scales.

As the historical precedents reveal, lower-energy machines, such as LEP, have via precision measurements predicted new phenomena followed by discoveries at higher-energy machines. Examples include the Z-boson, W-boson, top quark and Higgs-boson [32].

The FCC-ee is a very high luminosity[1], high precision collider at an energy range of $90 - 400$ GeV covering the energies at the Z pole, the WW threshold, the HZ maximum cross section, and the $t\bar{t}$ threshold. Since the colliding particles, electrons and positrons, are elementary and not composite as protons, it has the advantage of no underlying events, negligible pile-up collisions, and known energy and momentum of the initial state, hence also the final state energy and momentum are known.

[1] Luminosity L is defined by the relation between number of events N and the cross section σ for a given production, $N = \sigma \cdot L$.

Projected luminosities as a function of collision energy is shown for the FCC-ee in figure 3.2, where it is compared to that of other proposed e^+e^- colliders: CECP, a similar circular collider project proposed to be build in China, and the two linear colliders ILC and CLIC, proposed to be build in Japan and at CERN, respectively. The ILC collider had originally a scope of 250, 500, and an upgrade to 1000 GeV, but is in the latest plans focusing exclusively (at least in its initial phase) on the Higgs factory at 250 GeV. The CLIC experiment is designed as a discovery machine for high energies, covering energies between $380-3000$ GeV. The CECP project is in principle the same design as the FCC-ee but with lower luminosity and not aiming for the $t\bar{t}$ threshold. The FCC-ee is covering energies from the Z-pole to the $t\bar{t}$ threshold and has extremely high luminosity, especially for low center-of-mass-energies $\sqrt{s}$. It is worth noticing, that the luminosity of FCC-ee is three to four orders or magnitude higher than that of LEP. This is achieved due to modern accelerator technology developed at B-factories with very high focusing and top-up-injection [32].

Circular electron and positron storage rings are limited to a maximum beam energy of about 200 GeV, due to synchrotron radiation, where the energy loss is proportional to the gamma factor to the power of four over the bending radius $E_{\text{loss}} \propto \gamma^4/r$. For the very light electrons, the γ-factor is very high and thus results in a high synchrotron radiation. Contrary to e^+e^- circular colliders, linear e^+e^- colliders can obtain a high energy reach but have limited luminosity performance for low energies. Thus, ultimate precision measurements can be obtained with circular colliders, while ultimate center of mass energy can be obtained with linear colliders, making CLIC and FCC-ee complementary.

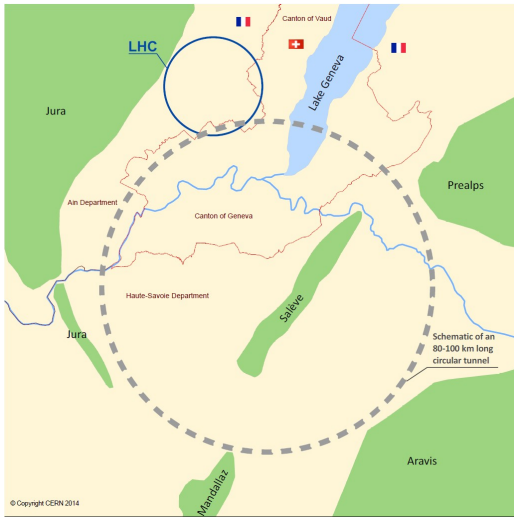

Figure 3.1: The FCC ring at the Swiss-French border close to the CERN site in Geneve [33].

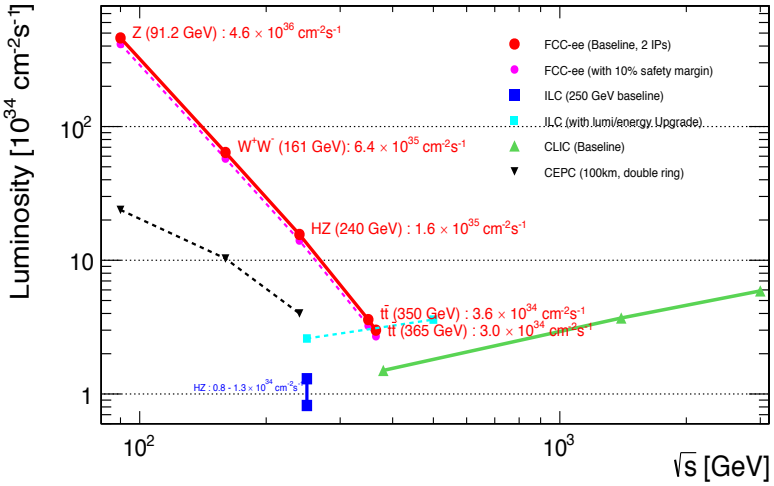

Figure 3.2: Projected lumminosity performance vs. center-of-mass-energy for proposed e^+e^- colliders: FCC-ee, CEPC, ILC, and CLIC [33].

3.1 Main Physics Motivation for the FCC-ee

The high luminosity of the FCC-ee, allow studies of the SM heaviest particles, Z, W, Higgs, and the top quark with ultimate precision. The very high statistics for the four channels have the anticipated order of magnitudes, Tera Z (10^{12}), several Oku[2] W (10^8), several Mega Higgs and a Mega top (10^6).

To improve the existing SM limits and exclude or discover new physics, several physics programs are on the schedule of FCC-ee. Some of the priorities at the Z pole, is the measurements of the lineshape, the mass and width, the weak mixing angle $\sin^2(\theta_W)$ measured via asymmetries, and branching ratios. Measuring number of neutrino generations, N_ν, and searching for rare decays, such as lepton flavour violation and sterile neutrinos are also on the agenda. Priorities for the WW and the $t\bar{t}$ threshold scans are measurements of their respective mass, branching ratios, and measurement of the strong coupling constant α_S. The goal of producing millions of Higgs-boson in a clean environment, is to measure all Higgs branching ratios at per mill precision, a precision needed to start probing into interesting regions as predicted by many popular extensions of the SM [34].

The estimate of improvement on the precision measurement observables is generally around a factor of 25 on the Z mass and width, and the W, top, and Higgs mass which will confine the constraints shown in the Gfitter plot in figure 2.1 by a factor 25 in each dimension [32].

Altogether the main motivation is to test the SM to very high precision and to set limits for and/or discover new physics. A way to formulate which limits precision measurements at lower energies puts on new physics is through the use of effective field theory (EFT). EFTs describe physics at a given energy scale with a given energy cut-off without describing the physics in detail in energy regimes out of interest. In other words EFTs facilitate (in particle physics) a simplification of a given interaction by a contact interaction, without describing the substructure of the interaction. An EFT addition to the SM Lagrangian is in general described by [35], [36]:

$$\mathcal{L}_{\text{SMEFT}} = \mathcal{L}_{\text{SM}} + \sum_i \frac{c_i}{\Lambda^2} O_i \tag{3.1}$$

where $\mathcal{L}_{\text{SM}}$ is the SM Lagrangian, O_i are operators describing new physics,

[2] Oku comes from Japanese and stands for 10^8.

c_i are dimensionless coefficients called the Wilson coefficients, i denotes the type of the operator, and Λ is the cut-off at which energy scale new physics might occur. In figure 3.3 the cut-off energy Λ, obtainable with the FCC-ee, is given for the different model-independent operators. It shows, that FCC-ee can constrain new physics for masses below 15 to 90 TeV, depending on the operator. This is based on the histogram bins, where the coloured bins represent the precision with current theoretical uncertainties and the dark bins represent precision without theoretical uncertainties. At the time when FCC-ee might be operating, the current theoretical uncertainties are expected to improve drastically. This imply that precision measurements at the FCC-ee might achieve limits on new physics at energy scales around 50 – 100 TeV.

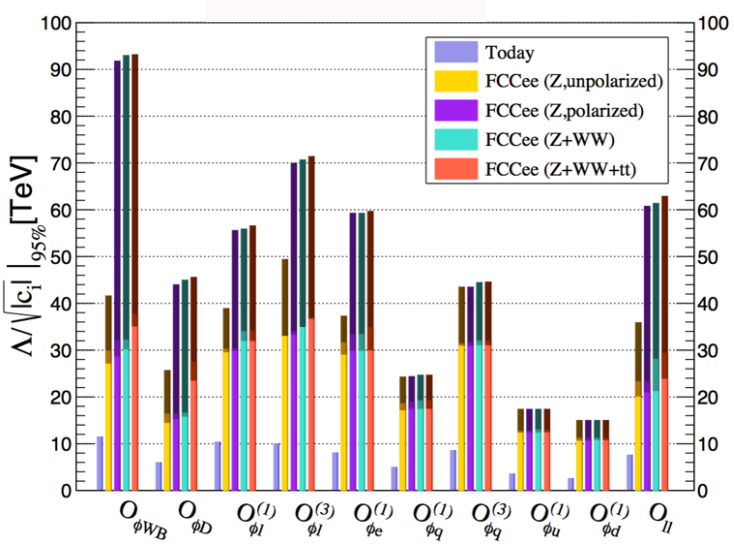

Figure 3.3: New physics reach of FCC-ee precision measurements as a function of SMEFT operators. Coloured bins represent precision with theoretical uncertainties and dark bins represent precision without theoretical uncertainties [37].

3.2 Accelerator at the FCC-ee

The design of the FCC-ee collider with ~100 km in circumference is optimized for maximum luminosity by having two separate e^+, e^- storage rings, and one accelerator ring, inspired by the modern B-factories, as

e.g. SuperKEKB [38]. The electrons and positrons will be accelerated, and reaccelerated due to energy loss from synchetron radiation, by the radio frequency (RF) cavaties located at the ring. The lifetime of a beam is about 15 minutes, constrained primarily by elastic e^+e^- scattering, Bhabha scattering, which is compensated by continous top up injection once per minute [32].

The accelerator is characterised by a very short bunch spacing, that throughout the optimisation has varied within the interval $3 - 20$ ns. The very short bunch spacing is challenging due to $\sim$ 20,000 bunches rotating in each direction. To avoid unintended collisions in the ring, the two beams are separated and are only brought into collisions in the detector areas, where the beams cross with an angle of 30 mrad at the interaction point (IP). The booster, that accelerates the two beams alternately to the beam energy as well as maintaining the top-up injection, is about 9 m from the IP for it not to collide with the detector. The two e^+, e^- beams are bent as little as possible before the collision at the IP, to minimize synchrotron radiation in the detector area, as it is a potential detector background. The sketch of the accelerator in figure 3.4 shows the separate e^+ and e^- beam lines in red and blue, the booster ring in green, the IPs and the two RF sections. The illustration in the middle shows a blow up of the three beam lines at the IP.

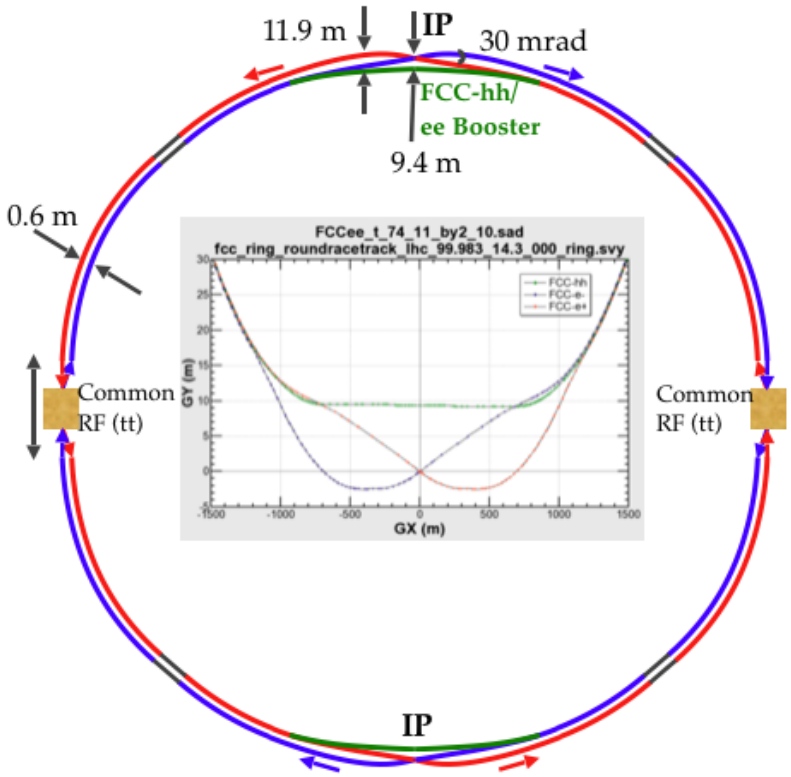

Figure 3.4: FCC accelererator with separate channels for e^+ and e^- (blue and red), booster ring (green), with two interaction points (IP) and two radio frequency (RF) sections. The illustration in the middle shows the three beam lines at the IP [37].

3.3 Detector

The experience of building e^+e^- detectors at collision energies comparable to those of the FCC-ee is broad. Examples are detectors at LEP and at the SLC (at SLAC) and the comprehensive detector design studies for the ILC project with the two detectors ILD and SiD. The CLIC detector design developed from a merge of the ILD and SiD detector designs. The FCC-ee aims for extremely high statistical precision, which demands a high systematic precision too, and requires very precise detectors.

In general, particle detectors are designed in such a way, that different

particles leave different signatures. A generic detector is designed with layers of different sub-detector technologies, usually with an inner tracking detector, an electromagnetic calorimeter, a hadronic calorimeter, muon chambers and a magnet system to bend the charged particles. Charged particles are measurable in the inner tracking detector. Both charged and neutral particles deposit their energy in one of the calorimeters, except high momentum muons traversing throughout the muon chambers. The electromagnetic calorimeter (EM-cal) measures the energy deposit from particles interacting electromagnetically (electrons and photons). Whereas strongly interacting particles (hadrons and hadronically decaying taus) deposit their energy in the hadronic calorimeter (H-cal). Neutrinos are so weakly interacting, that they leave no traces in the detector and are measured indirectly as missing energy. The different particle signatures in a generic detector are shown in figure 3.5, where solid lines indicate typical signatures and no lines indicate no interaction between the particle and detector material.

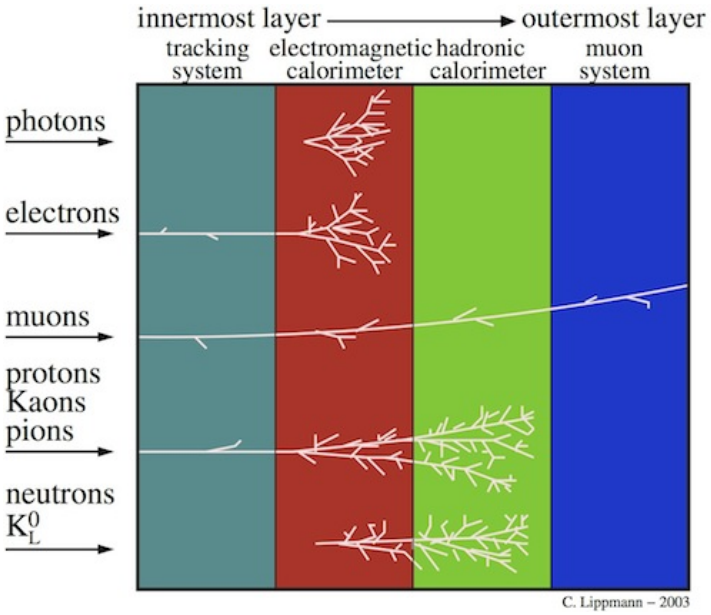

Figure 3.5: Signatures of different particles in a generic detector. Solid lines indicate typical signatures, whereas no lines indicate no interaction between the particle and the detector material [39].

3.3.1 Detector at the FCC-ee

A detector under its planning phase at CERN, CLICdp (CLIC detector project) [40], a state of the art detector, is now being adapted to the FCC-ee experiment. However, CLIC is designed for a linear accelerator, which implies some modifications for adapting the detector to the circular accelerator of the FCC-ee. Most importantly, the 30 mrad crossing angle of the beams puts an effective limit to the strength of the detector solenoidal field of 2 T as compared to 3.5 T at CLIC. To compensate for the lower momentum resolution which results for this, the radial dimensions of the detector are increased. The FCC-ee detector design is still under development, but is assumed to have the approximate same resolutions as the CLIC detector. The CLIC experiment is inspired by the advanced technology from the ILC experiment, and the CLICdp is a merge of the two ILC detector designs; the ILD and SiD detectors [41]. An illustration of the CLIC detector is shown in figure 3.6.

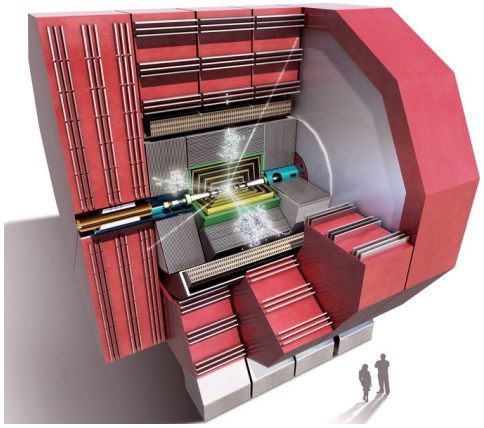

Figure 3.6: Illustration of the CLIC detector with a simulated particle collision, and two persons for size comparison [42].

The different layers of the detector are shown in figure 3.7, vertex detector and outer tracker (pink), electromagnetic calorimeter (green), hadronic calorimeter (light green), the coil (blue) and the muon chambers (red) outermost.

Tracking detector

The tracking detector, immersed in a magnetic field provided by the surrounding coil, measures trajectories of charged particles in order to determine their charge and momentum by its bending radius. It is made

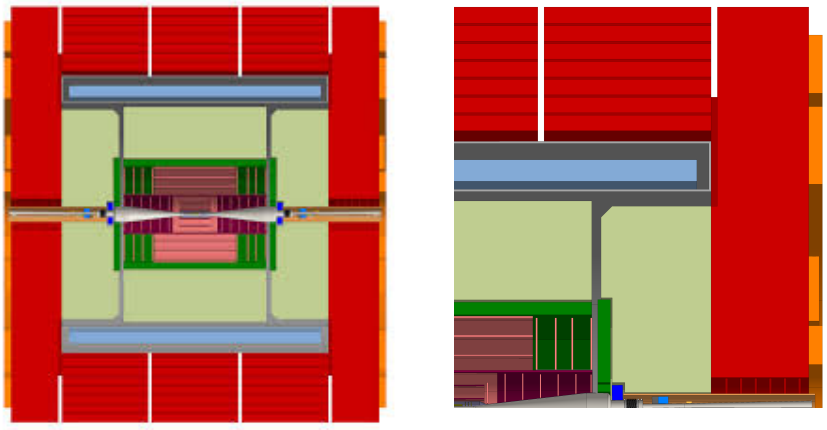

(a) **(b)**

Figure 3.7: (a) Illustration of the different layers in the CLIC detector, and **(b)** an enlarged slice of the detector [42] with the inner tracker detector (pink), the EM-calorimeter (green), hadronic calorimeter (light green), the coil (blue), and the muon chambers (red).

of silicon layers and consists of a very precise vertex detector and an outer tracker. The purpose of the vertex detector is to identify and measure secondary vertices from long-lived hadrons containing b or c quarks and from tau leptons.

For the work presented in this thesis a momentum resolution similar to that of the ILC experiments [41] have been assumed. Hence the resolution of the tracker can be parametrised by

$$\frac{\delta p_T}{p_T} = \sqrt{a^2 + (b \cdot p_T)^2} \tag{3.2}$$

with the parameters; a, a multiple scattering term, and b, a measurement term with the values: $a = 10^{-3}$ and $b = 2 \cdot 10^{-5}$ GeV^{-1}. The efficiency of the tracker to see a charged particle above a miminum momentum of 0.1 GeV was assumed to be $\epsilon = 99.5\%$. This for example corresponds to a relative precision of about 0.14% on the momentum measurement of muons from Z decays.

Calorimeters

The EM-cal is based on silicon-tungsten samplings, while the H-cal is based on tungsten for the barrel and steel at the endcaps. Both the electromagnetic and hadronic calorimeter can be parametrised by:

$$\frac{\delta E}{E} = \sqrt{a^2 + \left(\frac{b}{\sqrt{E}}\right)^2 + \left(\frac{c}{E}\right)^2} \tag{3.3}$$

with the parameters; a, a constant term, b, a stochastic term, and c, a noise term. The values of the parameters of the EM-calorimeter are $a = 0.011$, $b = 0.165$ GeV$^{1/2}$ and $c = 0.010$ GeV. The hadronic calorimeter has parameter values on: $a = 0.016$, $b = 0.58$ GeV$^{1/2}$ and $c = 0.18$ GeV. This for example corresponds to a relative precision of about 5.3% on the energy measurement of a 10 GeV photon, and a relative precision of about 18.5% of a 10 GeV neutron.

Magnet system

The solenoid outside the calorimeters of 2 T strength, makes it possible to measure momentum of charged particles by their trajectory subjected to the Lorentz force: $\boldsymbol{F} = Q\boldsymbol{v} \times \boldsymbol{B}$. The momentum of the particles are then measured by their bending radius, ρ, related by $p_T = 0.3 \cdot QB\rho$ [6], where p_T is the magnitude of the transverse momentum in GeV, Q is the charge in units of e, B is the magnetic field in T, and ρ is in units of m.

Muon chambers and magnet yoke

The muon chambers measure the tracks of muons and consist of track sensitive chambers in between layers of iron. With muons relatively high mass and non-strongly interacting nature, it is highly penetrating and traversing throughout the calorimeter systems. The iron layers minimize punch-through (jets that have not deposit all of their energy in the calorimeters) and function as well as a return yoke of the coil.

Part II

SEARCH FOR STERILE NEUTRINOS WITH THE FCC-*ee*

Chapter 4

Analysis of the FCC-*ee* Sensitivity for Sterile Neutrino Search

In the previous part I, the theoretical background and experimental conditions were outlined as a foundation for the analysis of the FCC-ee sensitivity to sterile neutrinos. Due to the 'clean physics' produced in e^+e^- collisions and the very high luminosity for the FCC-ee, sensitivity of very rare processes can be achieved in order to set new limits for the mixing angle. In this work, two possible search strategies have been investigated: I) long-lived sterile neutrinos, where the search is based on a sterile neutrino decay with a detached vertex, and II) short-lived sterile neutrinos, where the search is based on the topology of the events in a Monte Carlo study. These will be discussed in detail in the two following chapters. Since II) involved the coupling of the sterile neutrino to second generation fermions, this will be the main emphasis of the following discussion. In practice, however, search II) would be also performed for sterile neutrinos coupling to first generation, where the final state would encompass an electron in stead of a muon.

4.1 Previous Searches

In figure 4.1 is shown compilation of current and future sensitivity of the mixing angle between a muon neutrino and a single sterile neutrino $\theta_{\mu N}$

in the mass range 100 MeV - 500 GeV from various, prior and planned experiments.[1]

The (brown, shaded) area labelled 'Seesaw' shows the scale of mixing expected due to the Seesaw mechanism. Below this limit the Seesaw mechanism is in disagreement with the current limits on the active neutrino masses. The (grey, shaded) area labelled 'BBN' correspond to lifetime of the sterile neutrino > 1 second, which is disfavoured by Big Bang Nucleosynthesis [25]. The remaining limits are set by experiments, with existing limits shown with coloured areas and future potential limits presented with solid lines only.

The (brown, dotted) limit labelled 'EWPD' is the 90% confidence limit (C.L.) from the electroweak precision data, obtained by constrains from modified electroweak precision observables. As an example is the Fermi constant G_F, that is measured from muon decays, modified due to the effects of the sterile neutrinos by $G_\mu^2 = G_F^2(1-|\theta_e|^2)(1-|\theta_\mu|^2)$ [29].

The limit set by the CHARM experiment, labelled 'CHARM' and 'CHARM-II' (dark grey, shaded) is a 90% C.L. probed by D-mesons produced in a fixed target experiment and decaying mostly semileptonically, thus in association with a neutrino. The (violet, solid) counter labelled 'SHiP' is the expected limit at 90% C.L. for the proposed SHiP experiment at CERN. The high intensity and fixed target experiment is proposed to probe this limit by charm (c) and beauty/bottom (b) meson decays, with semileptonic decays. Both the CHARM and SHiP limits are constrained by the respective meson masses.

The (green, dashed) and (pink, dashed) counter labelled 'DELPHI' and 'L3' are 95% C.L. obtained from Z-decays at the DELPHI and L3 experiment, both experiments at LEP-I. The (light green, solid) contour labelled 'FCC-ee' is the expected limit at 95 % C.L. at the proposed 100 km accelerator with 10^{12} Z-decays. This study is reproduced and the results confirmed in chapter 5. The DELPHI, L3, and FCC-ee limit are all constrained by the Z mass. The (blue, solid) contour labelled 'ATLAS' is a 95% C.L. for sterile neutrinos produced in highly off-shell W-decays or from a hypothetical heavy W-boson, that only couple to right-handed particles. The limits of most interest for this study are the DELPHI limit (dashed, green) and the FCC-ee limit (light green), which will be elaborated in chapter 5.

[1] Similar plots are found for mixing with the two other flavours θ_{eN} and $\theta_{\tau N}$ in [43].

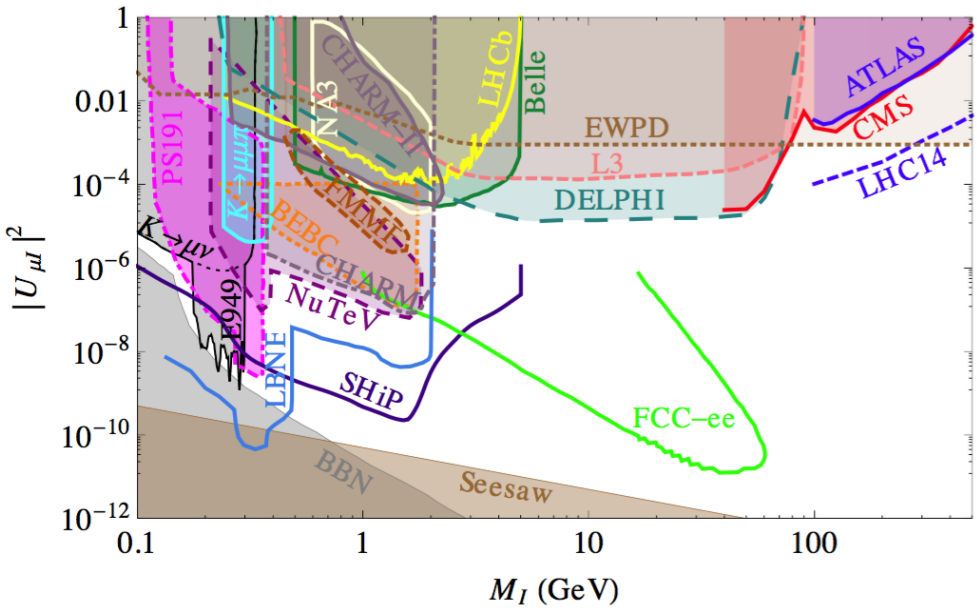

Figure 4.1: Combined limits for the mixing angle between the muon neutrino and a single sterile neutrino $|\theta_{\mu N}|^2$ (here denoted as $|U_{\mu I}|^2$), as a function of the mass of the sterile neutrino M_N (here denoted as M_I). The limits with coloured areas are existing limits, whereas the contours with lines only are future potential limits [43].

4.2 The DELPHI Limit

The DELPHI experiment was one of the four main detectors at LEP (Large Electron Positron Collider) located at CERN, running in the period 1989-2000 in the same tunnel as LHC is currently running. In the search for sterile neutrinos (denominated heavy neutral leptons in [1]), DELPHI still preserves the best limit for masses at electroweak scale. A total number of $3.3 \cdot 10^6$ hadronic Z events was collected for the search, from which an upper limit could be set on the branching ratio of $BR(Z \to N\nu) \sim 1.3 \cdot 10^{-6}$ at 95% confidence level for masses from 3.5 to 50 GeV. The obtained limit for the mixing angle $|\theta|^2$ (denominated $|U|^2$ in [1]) as a function of mass, as well as the efficiency, is shown in figure 4.2. Since the DELPHI analysis was complete inclusive regarding the leptonic initial and final states, the limit was obtained for $|\theta|^2$ which incorporate mixing angles of the sterile neutrino to all three neutrino flavours.

The DELPHI limit is a merge of two limits, search for sterile neutrinos with short life time, and sterile neutrinos with long lifetime. It is a combined result from four separate searches, short-lived sterile neutrino production with I) monojet signatures or II) acollinear jet topologies, and long-lived sterile neutrinos with III) detectable detached vertices or IV) calorimeter cluster.

When the DELPHI limit is redrawn, it is frequently drawn flat at the bottom, like in figure 4.1. Genuinely it consists of two parts, one for short lived sterile neutrinos and one for long lived, as seen in figure 4.2. The same shape of the FCC-ee limit appears for the limit of the long lived sterile neutrinos of the DELPHI limit.

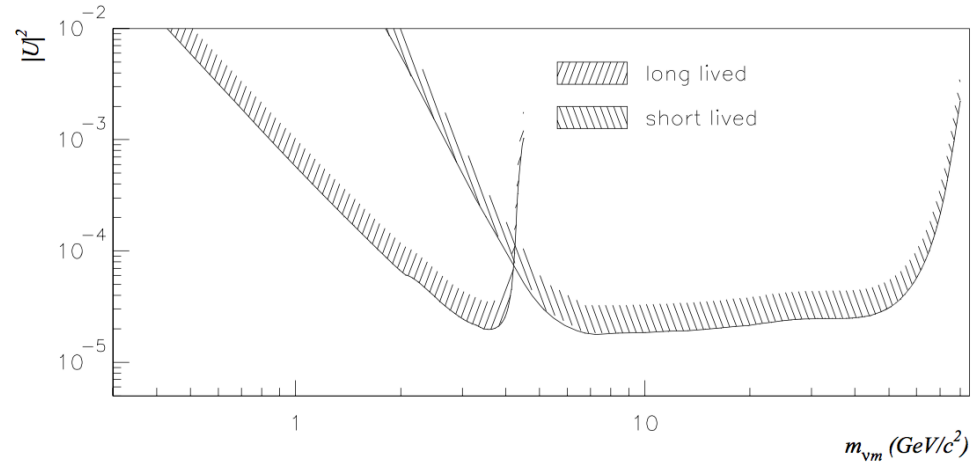

(a)

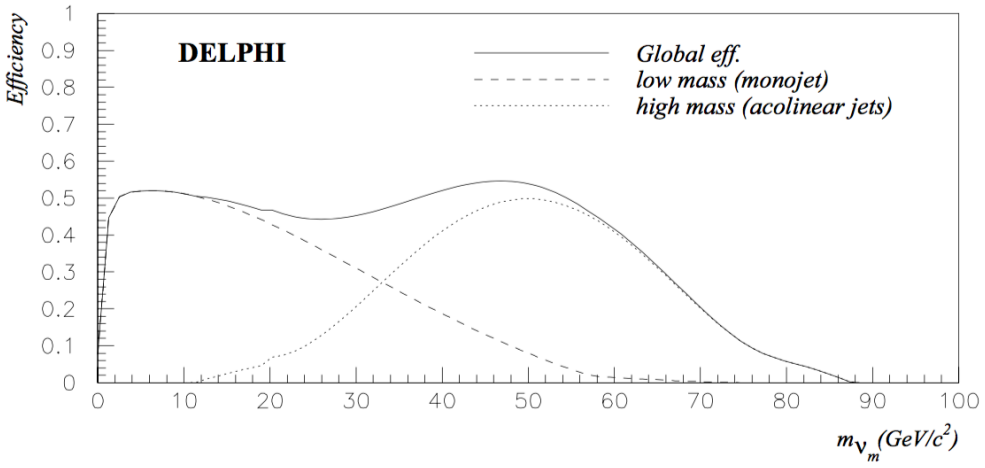

(b)

Figure 4.2: (a) DELPHI limit for the sterile neutrino mixing angle $|\theta|^2$ (here denoted $|U|^2$), as a function of mass, and **(b)** the selection efficiency as a function of mass. [1]

Chapter 5

Search for Sterile Neutrinos with Long Lifetime

In this chapter the FCC-ee sensitivity of sterile neutrinos with long lifetime is presented, inspired by [44]. Long-lived sterile neutrinos imply, for this study, sterile neutrinos that decay with a detached vertex and with masses below the W mass. This search investigate sterile neutrino produced from $Z \to \nu\bar{\nu}$ with one of the active neutrinos mixing into a sterile neutrino. The production, decay and the FCC-ee sensitivity of long-lived sterile neutrinos are presented followed by a discussion of background estimates.

If the sterile neutrino has sufficiently small mixing angle and mass, its lifetime will be long enough for it to decay with a detectable time of flight. A signature with a detached vertex with decay products recoiling against an undetected active neutrino is expected to be virtually free from background. This is discussed in detail in the next section. For very short lifetime of the sterile neutrino, where the time of flight is too short to detect, signal and background becomes harder to discriminate, and requires another analysis procedure, which is elaborated in chapter 6.

Assuming no background for the detached vertex, an analysis of the sensitivity in the FCC-ee detector was performed. In this analysis, the sterile neutrino can decay into all possible decays, the only requirement being the detection of a detached vertex at a detectable distance from the interaction point. A 2σ significance (corresponding to 4 signal events s, due to $Z = s/\sqrt{s+b}$, where number of background events $b = 0$) has

been required and calculated from a total number of 10^{12} Z-bosons. Two different detector volumes, for which the detector is sensitive to detached vertices, are considered. The considered detector volumes are sensitive to detached vertices decaying with a flight distance between a) 1 mm − 1 m, and b) 100 μm − 5 m. For the previous outlined detector design sensitivity of a) is fully satisfied, where the sensitivity of b) would require a rethinking of the detector design.

The number of sterile neutrinos from Z-decays is governed by

$$N_N = N_Z \cdot BR(Z \to N\nu), \tag{5.1}$$

where the branching ratio is obtained from the partial width in equation (2.30). The number of produced sterile neutrinos from Z-decays for a given mixing angle and mass is shown in figure 5.1. The production rate of the sterile neutrino is mass independent except for the effect of the phase space, which has an impact for masses larger than 40 GeV as shown in figure 5.1.

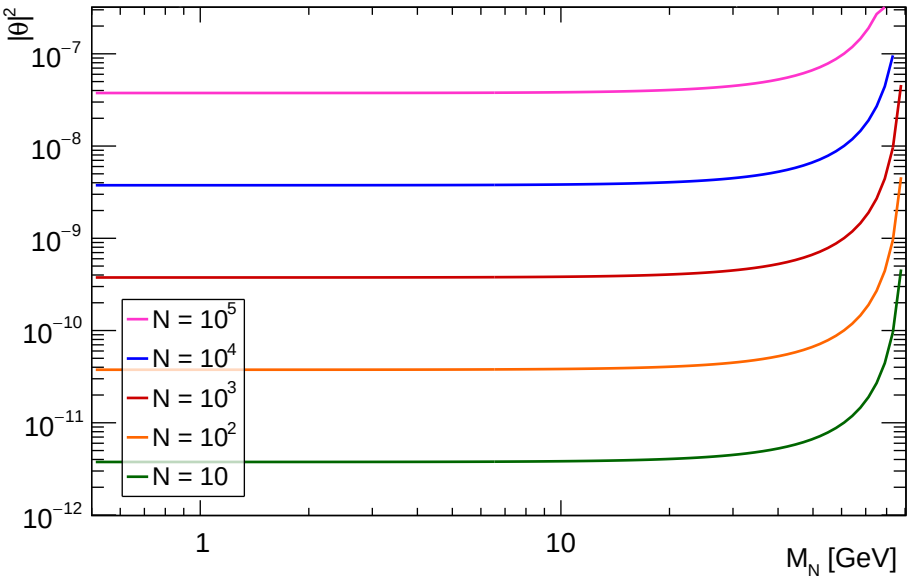

Figure 5.1: Number of sterile neutrinos produced in 10^{12} Z decays as a function of the mass, M_N, and the mixing angle, $|\theta|^2$.

The decay length λ is obtained from the lifetime τ_μ, given by equation 2.33, multiplied by the speed of light and the boost in laboratory frame $\gamma\beta$:

$$\lambda = \gamma\beta c \cdot \tau_\mu, \tag{5.2}$$

where $\gamma\beta = p_N/M_N$, and the momentum of the sterile neutrino p_N, is obtained from simple energy-momentum conservation:

$$p_N = \frac{m_Z^2 - M_N^2}{2m_Z}. \tag{5.3}$$

The dependence of fixed lifetimes in the range from 100 μm to 1000 km on the mixing angle and mass is shown in figure 5.2. The total number of decaying sterile neutrinos inside the detector volume is obtained by

$$N_{\text{decay}} = N_0[\exp(-d_{min}/\lambda - \exp(-d_{max}/\lambda))], \tag{5.4}$$

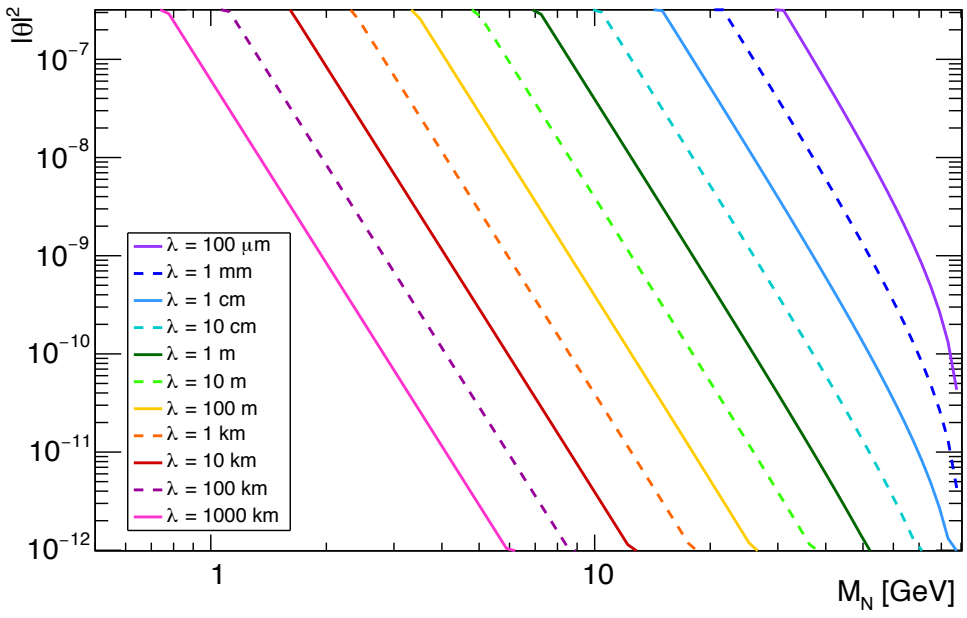

Figure 5.2: Counters of fixed decay lengths in the laboratory frame of sterile neutrinos as a function of the mass M_N, and the square of the mixing angle $|\theta|^2$.

where d_{min}, d_{max} are the minimum and maximum distance detectable in the detector and λ is the actual decay length from equation (5.2). For any flight distance considerably larger than d_{max}, the outer radius of the

detector, the fraction of events decaying inside the detector volume is of course $f = d_{\max}/\lambda$. In practice this will be the case for any $\lambda \gtrsim 10$ m.

A production of 10^{12} Z-bosons in the FCC-ee would produce $\sim 2 \cdot 10^{11}$ $Z \to \nu\bar{\nu}$ which, for a mixing angle of the sterile neutrino $|\theta|^2$ down to 10^{-11}, would be adequate to provide a few events, depending on the mass of the sterile neutrino. The sensitivity of sterile neutrinos in two proposed detector sizes with sensitivity to detached vertices at distances: 1 mm−1 m (orange) and 100 μm−5 m (red) is shown in figure 5.3. In the lower left section of the plot, the detection is constrained by too long lifetimes of the sterile neutrinos, resulting in decays outside of the detector. A larger detector would improve the detection efficiency in the area, hence the red contour, representing a detector with a 5 m outer radius, extends further to the left. Above the contours in the right corner, the detection is limited by too short lifetimes to detect a detached vertex. Sensitivity improvements in this area, could be obtained with a more precise vertex detector, even though the difference between the two considered inner radii does not seem to play a major role.

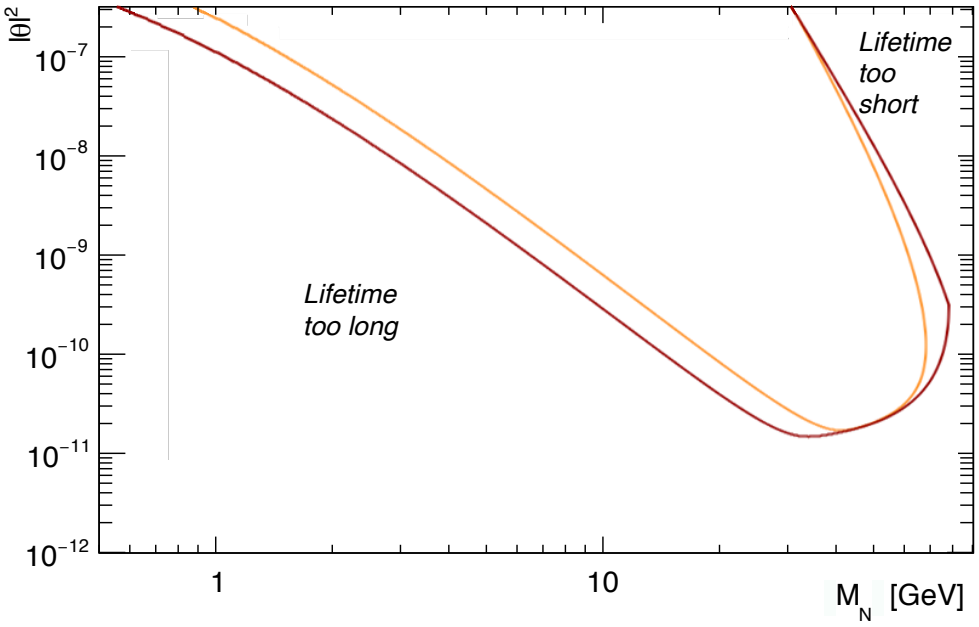

Figure 5.3: Sensitivity on 2σ (4 events) of the mixing angle, $|\theta|^2$, vs mass of the sterile neutrino N decaying with a detached vertex inside the FCC-ee detector volume. The orange graph represent decay lengths from a) 1 mm−1 m, the red graph decay lengths from b) 100 μm−5 m.

5.1 Background Estimates of Long-lived Sterile Neutrinos

Two possible background contributions to the long lifetime search has been identified: I) $Z \to \tau^+\tau^-$ decays, and II) interaction of atmospheric neutrinos in the detector material. Both turn out to be negligible as argued in the following discussion.

The background candidate $Z \to \tau^+\tau^-$, is considered for decays with one tau decaying hadronically into 1, 3, or 5 charged particles and a neutrino, a so-called 1-, 3-, or 5- prong decay, and the other tau decays leptonically to a soft electron together with the respective neutrinos, with the electron energy too low to detect. Since the minimum energy of the observed system from a τ decay is $E_{\text{min}} = \left(\frac{m_{\text{sys}}}{m_\tau}\right)^2 \cdot E_\tau$, the minimum energy of an

electron is ~ 4 keV, and can go undetected, whereas the minimum energy from a muon is ~ 160 MeV, and would be detected, due to the energy threshold of the detector of about 100 MeV. Such τ decay with a very soft electron would cause a mono-jet signature with a detached vertex with a relatively short distance to the IP, due to the lifetime of the τ. With a lifetime of the τ on $2.9 \cdot 10^{-13}$ s [6] and a gamma-factor of ~ 26, the τ from a Z decay has a flight distance around 2.3 mm. This background can be distinguished from the signal by observing that the tau lepton is charged whereas the sterile neutrino is neutral. Hence, by requiring that the sum of charges of the final state particles add up to zero. Another way to discriminate these events from a possible sterile neutrino, could be to require decays with masses below 2 GeV[1] to have a decay length considerable larger than the decay length of the τ, since light sterile neutrinos would be boosted and hence have a long flight-distance in the detector.

Other possible background candidates for the detached vertex search could come from the cosmic ray background. Standard backgrounds from cosmic rays, muons which penetrate down to the detector is not considered to be a background since the muon can hardly enter the detector unnoticed and thus is very unlikely to produce a mono-jet signature. However, atmospheric neutrinos interacting with the material inside the detector volume could potentially produce a mono-jet signature. In order to produce a signature with high enough energy for detection, a neutrino energy higher than a couple of GeV is required, thus solar neutrinos are not of relevance in this study, since they only carry energy in the MeV range. The most abundant neutrinos in the high energy spectrum are the muon neutrinos coming from pion decays in cosmic rays, also referred to as atmospheric neutrinos. Neutrinos with sufficient energy have a very small, but non-vanishing probability of interacting with the detector material, due to the high neutrino flux. Deep inelastic scattering of a nucleon caused by an atmospheric neutrino, could then potentially produce a mono-jet signature in the detector.

The cross section measurements of muon neutrinos and anti-neutrinos in charged current interactions are collected from the experiments; BNL 7-foot bubble chamber experiment, SKAT, Gargamelle, and SciBooNE. The contributing processes for the cross section measurement are quasi-elastic scattering, resonance production, and deep inelastic scattering, and are shown in figure 5.4a and 5.4b. The neutrino flux is measured by several experiments, e.g. the India-based Neutrino Observatory (INO),

[1]The tau lepton has a mass of 1.777 GeV.

the IceCube experiment at the South Pole, Pyhäsalmi in Finland, and Super Kamiokande in Japan. Their flux measurements are consistent, when averaging over one year and all directions [45]. The neutrino flux measurements from Super Kamiokande are shown in figure 5.4c.

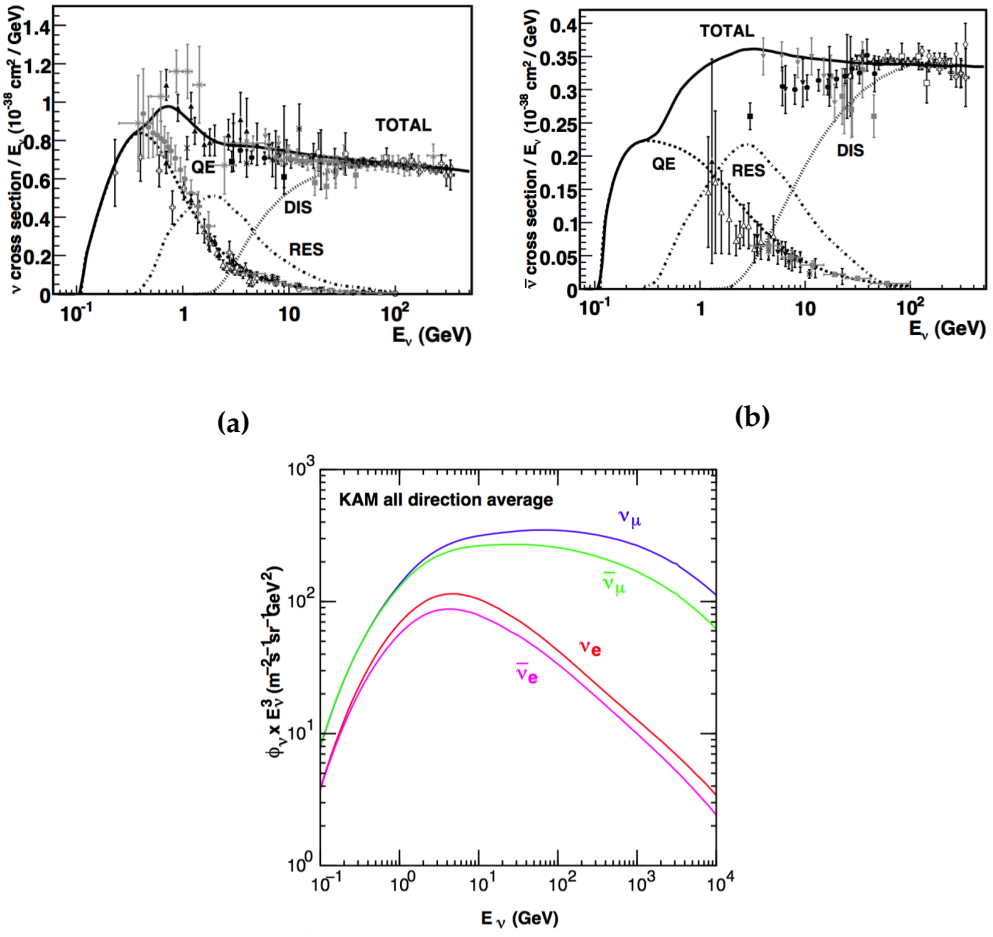

Figure 5.4: Muon neutrino **(a)** and anti-neutrino **(b)** cross section in charged current interactions divided by the neutrino energy plotted as a function of energy [46]. The data is collected by several experiments: ▲ (BNL 7-foot bubble chamber experiment [47]), * (SKAT [48]), ■ (Gargamelle [49]), and ⋆ (SciBooNE [50]). The various contributing processes are shown; quasi-elastic scattering (QE), resonance production (RES), and deep inelastic scattering (DIS). Figure **(c)** shows the neutrino flux measured by Super Kamiokande averaged over one year and all directions [45].

In order for an interaction of an atmospheric neutrino to imitate a signal of a sterile neutrino, the expected missing momentum from the active neutrino produced in association with a sterile neutrino is $p_\nu = p_N$ with the expression for p_N given in equation (5.3), should be consistent with the reconstructed invariant mass of the decay products from the inelastic scattering of a nucleon by the atmospheric neutrino, $m_{inv} \approx \sqrt{2m_p E_\nu}$, where m_p is the mass of a proton, and $E_\nu \sim p_\nu$. When those two expressions are combined, it is realised that only neutrino energies around 45 GeV are meeting the requirements. If an atmospheric neutrino interacts via inelastic scattering with the detector material, the final state momentum could be fully reconstructed, thus equivalent to the initial energy of the atmospheric neutrino. A mono-jet system with a reconstructed mass above 100 GeV would certainly not have its origin from a Z decay. Hence neutrino energies from 40 GeV to 100 GeV were taken into account in the estimate.

To make a rough estimate, the graphs showing the flux and cross sections were all considered to be flat in the studied energy range. The summed cross section of ν_μ and $\bar{\nu}_\mu$ was estimated to $\sigma/E_\nu < 1.2 \cdot 10^{-38}$ cm^2/GeV from figure 5.4a and 5.4b. Whereas only the CC cross sections are given in figure 5.4a and 5.4b it is the sum of the CC and NC current cross section which is of relevance here. Since the cross section of CC interactions was at least a factor two higher than NC interactions (see table XI in [46]), a total summed maximum cross section of ν_μ and $\bar{\nu}_\mu$ was estimated to $\sigma/E_\nu < 2 \cdot 10^{-38}$ cm^2/GeV. The flux of ν_μ and $\bar{\nu}_\mu$ was estimated with a maximum mean value of $\phi \times E_{nu}^3 < 400$ m^{-2}s^{-1}sr^{-1}GeV from figure 5.4c.

Integrating the product of neutrino cross section and flux in the energy interval 40−100 GeV, yields a number of neutrino interactions per second per nucleus. A detector with thin silicon layers, mostly consisting of air, was assumed. The largest detector for this study was considered (a 4 meter long cylinder-shaped detector with 5 meters in radius) with an estimated mass of 400 kg. It was then assumed that the effective mass is 10 times larger, when instrumentation was taken into account, thus an effective mass of approximately 4 ton. Data-taking was assumed to be approximately a third of a year.

With the listed assumptions, less than 0.005 atmospheric neutrinos would interact per year. Only considering those decays interacting in the opposite hemisphere of the direction of the atmospheric neutrino came from, in order to imitate a signal, the background candidates would be halved. An additional requirement that the vertex points towards the IP with an correct mass and time-of-flight is expected to kill the background. Since the atmospheric neutrinos have a higher probability of interacting

in the thin silicon layers, than in between the layers, a veto on detached vertex interactions originating from the silicon layers, could decrease this background even further.

5.2 Summary of Search for Sterile Neutrinos with Long Lifetime

Two background candidates, $Z \to \tau^+\tau^-$ and atmospheric neutrinos, were considered for the search for sterile neutrinos with long lifetime at the FCC-ee with 10^{12} Z boson decays. Both backgrounds candidates were estimated to be negligible. The search reach shown in figure 5.3 is thus well-founded, and displays a discovery reach for sterile neutrinos for mixing angles $|\theta|^2$ down to 10^{-11}, covering a large part of the allowed parameter space, cf. figure 4.1.

Chapter 6

Search for Sterile Neutrinos with Short Lifetime

This part of the analysis investigates the sensitivity of the FCC-ee for short lived sterile neutrinos in the mass range 10 – 80 GeV. The ambition is to improve the DELPHI analysis discussed in section 4.2 with a better detector, and investigate how the analysis scales with increased statistics. For this study, 10^8 hadronic Z events were generated corresponding to $1.43 \cdot 10^8$ Z events, which is 30 times more statistics than DELPHI. FCC-ee aims for way higher statistics (10^{12} Z bosons), but fewer events are investigated due to limitation of computer resources.[1]

6.1 Analysis Strategy

This study aims to cover as much as possible of the parameter space between the DELPHI limit and the FCC-ee long lifetime limit, as well as the parameter space in the right corner above the FCC-ee limit in figure 4.1. In this area, the sterile neutrino has too short lifetime for a detached vertex to be detected, referring to figure 5.2. Hence, the analysis rely on the topology of the events in order to distinguish background from signal.

[1] Generating 10^8 $Z \to q\bar{q}$ events in PYTHIA and writing to HepMC format took about 16 hours and took up 67 GB of memory by saving only ~ 4% of the selected events. To generate $7 \cdot 10^{11}$ $Z \to q\bar{q}$ corresponding to 10^{12} Z bosons, as FCC-ee is striving to produce, would take around 13 years and the datafile would be 470 TB large!

In order to simplify the current study it was restricted to specific final states. Firstly, it was decided to consider only fully visible final states proceeding via charged current interactions. The fully visible modes with branching fractions of about 50%, see section 2.4, have the advantage that the mass of the sterile neutrino can be fully reconstructed from the final state particles. Secondly, it was decided to concentrate on the mode with a muon in the final state, i.e. the decay $N \to \mu^{\pm} q\bar{q}'$.

A total of 10^8 $e^+e^- \to Z \to q\bar{q}$ events were generated, which correspond to a total integrated luminosity of $L_{int} = N/\sigma = 3.33$ fb^{-1}. Even if a generation of 10^{12} Z-bosons had been possible for an appropriate time scale, the result would not necessarily be trustworthy, due to the generation of very rare decays in rare areas of phase space, for which the generators have certainly not been tuned.

In this study, methods were sought to best separate sterile neutrino signal from background. The strategy was to develop selection criteria to minimize the background, ideally eliminate it completely, while trying to keep as high signal efficiency as possible. To avoid biases, the cuts were developed on one set of Monte Carlo samples and then finally tested on an independent set of samples. All background samples were scaled to the integrated luminosity $L = 3.33$ fb^{-1}, while the number of generated signal events, was arbitrary.

The signal investigated in this study is the process $Z \to \nu N$ with $N \to \mu\bar{q}q$. Eight different signal samples were analysed with a sterile neutrino mass of 10, 20, 30, 40, 50, 60, 70, and 80 GeV. The signal has a characteristic signature of **a)** high missing momentum coming from the non-observation of the active neutrino, and **b)** a muon produced in association with **c)** a mono-jet or a di-jet depending on the sterile neutrino mass. All three characteristic signatures are dependent on the sterile neutrino mass, also referred to as signal mass. For low masses, the signal signature tends to be a mono-jet close to the muon. The higher the sterile neutrino mass gets, the lower the boost thus the larger opening angle of the jet(s) and the lower the missing momentum.

The background candidates considered for the study were:

1. $Z \to q\bar{q}$ because of the high cross section of 30 nb. With this enormous amount of events, there is a possibility of producing events that are very distinct from the ordinary $Z \to q\bar{q}$ decays.

2. $Z \rightarrow \tau^+\tau^-$ since a lot of the events already contain a muon, a jet, and missing momentum.

3. $Z \rightarrow \mu^+\mu^-$, since it already involves a muon.

4. The four-fermion process $e^+e^- \rightarrow e^+e^-q\bar{q}$ mostly due to the two-photon process containing a jet and with an electron going into the beam-pipe creating missing momentum.

5. The four-fermion process $e^+e^- \rightarrow q\bar{q}\mu\nu$, due to the decay products being identical to the decay products of the signal.

The distribution of missing momentum for the signal and background samples are shown in figure 6.1. A more detailed description of both signal and background samples are presented in sections 6.5 and 6.6.

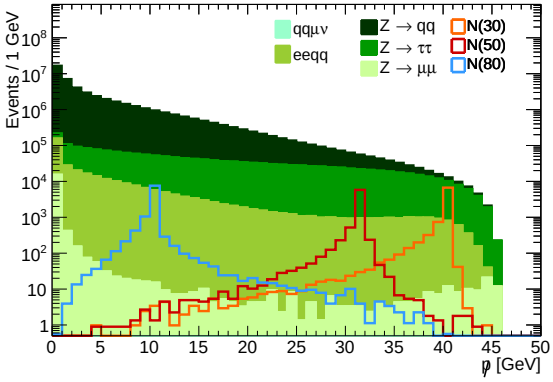

Figure 6.1: Distribution of missing momentum at generation level without any cuts applied. Three different signal samples with sterile neutrino masses of 30, 50, and 80 GeV are superimposed with all background samples.

6.2 Outline of the Analysis

In order to optimise memory as well as CPU time for the data processing, a pre-selection was made before saving the events for subsequent analysis. Hence, the study was separated into three steps: I) pre-selection, II) main analysis, and III) sliding cuts, as shown schematically in figure 6.2a. Furthermore, the main analysis was divided into two parts: A low mass

analysis performed for the sterile neutrino masses 10, 20, and 30 GeV, and a high mass analysis performed for the masses 30, 40, 50, 60, 70, 80 GeV. Finally, sliding cuts were applied, focussing on the individual mass points.[2]

Since the decay channel $N \rightarrow \mu q\bar{q}'$ was chosen for this search, the sterile neutrino N is assumed only to couple to the muon neutrino, ν_μ, via the parameter $|\theta_{\mu N}|^2$. Strictly speaking, the coupling investigated in this search is equal $(\theta_{eN} + \theta_{\mu N} + \theta_{\tau N}) \cdot \theta_{\mu N}$, since the Z boson decays into all three neutrino flavours, which in principle can all mix into the sterile neutrino N, and then mix into the highly off-shell ν_μ that decays into the decay products $\mu q\bar{q}'$. For convenience, and in order to compare with existing results, the assumption of the sterile neutrino only coupling through $|\theta_{\mu N}|^2$ is implemented. Ideally, similar analyses would be made for the $e^\pm$ and $\tau^\pm$ channels, in order to combine the limits for all three leptonic decay channels.

The sterile neutrino is assumed to have too short lifetime to detect a detached vertex. For decay lengths below 100 μm, the kinematics of the events does not depend on the mixing angle $|\theta|^2$, but exclusively on the sterile neutrino mass m_N. Hence, the only signal parameter changed in this analysis is the mass.

The missing momentum $\not{p}$, arising from the active neutrino from the signal, can be expressed as an delta function for a given signal mass:

$$\not{p} \sim p_\nu = \frac{m_Z^2 - m_N^2}{2m_Z} \tag{6.1}$$

This is characteristic for the signal, and therefore used in the sliding cuts in section 6.10. Numerical values for the neutrino momentum, p_ν, for each signal mass were found by eq. (6.1) and is shown in the table in figure 6.2b. The pre-selection, the two analysis for low and high mass, and the sliding cuts, are described in detail in section 6.7, 6.8, 6.9, and 6.10 respectively.

[2]For an analysis with real data and search for an sterile neutrino with an unknown mass, sliding cuts or sliding window, would have been shifted with much smaller intervals, probably at a step size of approximately the resolution of the given parameter.

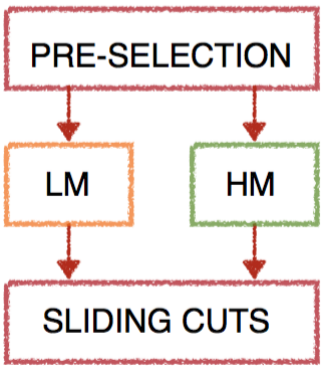

(a)

M_N [GeV]	p_ν [GeV]
10	45.1
20	43.4
30	40.7
40	36.8
50	31.9
60	25.9
70	18.7
80	10.5

(b)

Figure 6.2: **(a)** Schematic picture of the total analysis. **(b)** Theoretical recoiling neutrino momentum, p_ν, for each signal mass.

6.3 Generation of Events

The event samples were generated with the event generators PYTHIA 8.2 [51] and WHIZARD 2.4.0 [52]. The main strength of PYTHIA is the hadronisation of events via parton shower. To generate events in PYTHIA, the specific processes shall be parsed to the generator. In WHIZARD, on the other hand, only the particles in the initial and final state shall be parsed to the event generator, and then every process is calculated via matrix elements. Productions were simulated for e^+e^- beams at the Z-pole, $E_{CM} = 91.2$ GeV, implying all standard settings in both PYTHIA and WHIZARD. All samples were written to HepMC format [53], from where they were read and analysed.

The signal samples, and the background samples, $Z \to q\bar{q}$, $Z \to \tau^+\tau^-$ and $Z \to \mu^+\mu^-$ were generated with PYTHIA, while the four-fermion processes, $e^+e^- \to e^+e^-q\bar{q}$ and $e^+e^- \to q\bar{q}\mu\nu$, were generated with WHIZARD, and then subsequently hadronised through PYTHIA.

6.4 Detector Parametrisation

A detector parametrisation based on section 3.3.1 was done for all samples. The method used to smear the momentum and energies of the particles is based on what is known as "particle flow": The energy of all particles is determined, as much as possible, by the charged tracks measured in the tracking detectors. The calorimeters are then mainly used to determine

the energy of the neutral particles, not detected in the tracking detectors.

As a first step neutrinos were removed. Particles close to the beam line with an angle $|\cos(\theta)| < 0.99$[3] were removed, as well as soft particles with momentum below $p < 0.1$ GeV that would curl up due to the B-field. The momentum and energy of the remaining particles were then smeared with parametrisation of the tracker, the electromagnetic calorimeter and the hadronic calorimeter:

- The momentum of all charged particles were smeared with the parametrisation of the tracker from equation (3.2) with the efficiency of measuring a track of 99.5%.
- The momentum of all photons were smeared with the parametrisation for the electromagnetic calorimeter given in equation (3.3) with the corresponding values.
- Finally, the momentum of all neutral hadronic interacting particles were smeared with the parametrisation from (3.3), with the corresponding values for the hadronic calorimeter.

The detector parametrisation was done in two steps, first with a prototype detector simulation, followed by a smearing of the sample. The prototype detector simulation includes removing neutrinos, soft particles, and particles close to the beam line. The smeared sample encompasses the prototype detector simulation and the parametrisation. The invariant mass of $Z \to q\bar{q}$ is shown in figure 6.3 at generator level, with the prototype detector simulation, and with the smeared sample. The smearing manifests itself in the mass spectrum as a tail for the higher masses as well as a boosted tail for the lower masses, compatible with lost particles at low angles and momenta.

6.4.1 Misidentification of Pions as Muons

Muons penetrating the calorimeters and muon chambers lose about 3 GeV by ionisation. Hence, only muons with momentum higher than $p > 3$ GeV were identified. Due to consideration of pion decays ($\pi^{\pm} \to \mu^{\pm}\nu_{\mu}$) and pions interacting late in detector (punch through), a misidentification

[3] For this detector a right-handed Cartesian coordinate system is used with origin at the IP, the x-axis pointing towards the center of the accelerator ring, the y-axis pointing upwards and the z-axis along the beam line. The polar angle θ expresses the angle down to the beam line, while ϕ denotes the azimuthal angle.

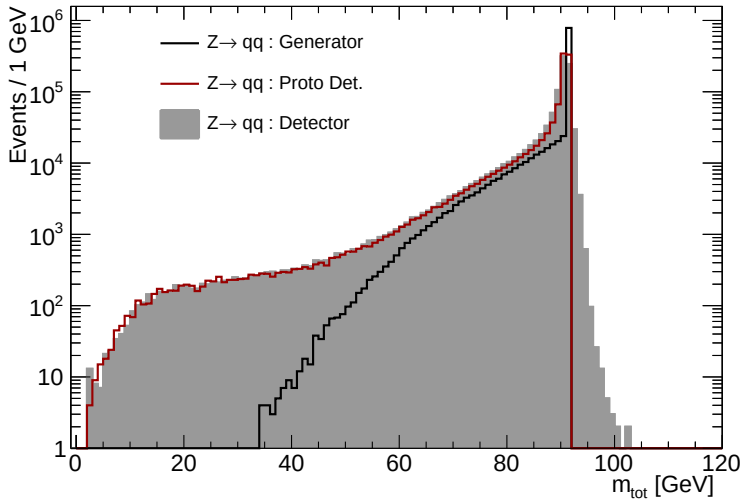

Figure 6.3: Comparison between generator level (black line), prototype detector simulation (red line), and the smeared sample (gray) for the invariant mass of $Z \to q\bar{q}$.

of pions as muons with a probability of 0.25% was implemented in accordance with estimates from the ILC detectors [41]. In figure 6.4a the number of true muons is shown, the number of misidentified muons is shown in figure 6.4b, and the total number of muons, with both true and misidentified muons, is shown in figure 6.4c.

After the detector parametrisation and misidentification, jets were reconstructed using the e^+e^- k_t algorithm (Durham algorithm) from fastjet [54]. The *exclusive jets* algorithm was employed to force events into one, two, or three jets, depending on the analysis and cuts. The reconstructed muon was not included in the jet reconstruction.

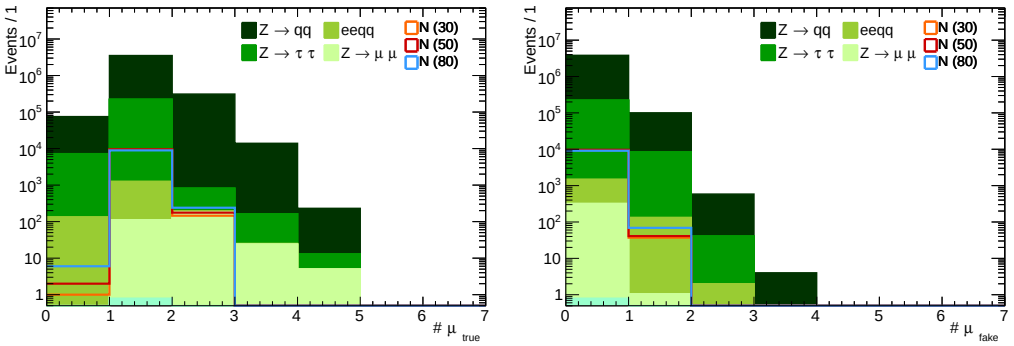

(a) **(b)**

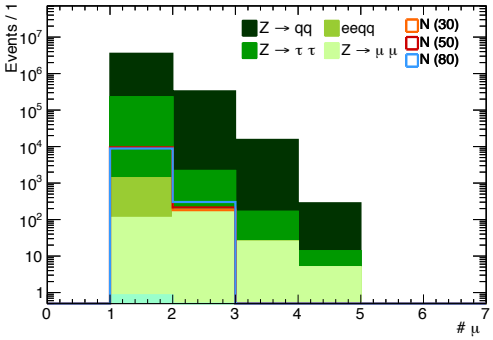

(c)

Figure 6.4: **(a)** Number of true muons, **(b)** number of misidentified pions as muons, and **(c)** the actual number of identified muons including both true and fake muons with a requirement of at least one muon in the event.

6.5 Signal Signatures

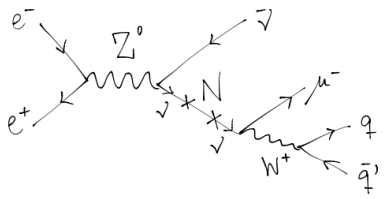

Figure 6.5: Feynman diagram of the signal process $e^+e^- \to Z \to N\bar{\nu}$ with $N \to \mu^- W^+ \to \mu q\bar{q}$

For the production $Z \to \nu N$ with the decay $N \to \mu W \to \mu q\bar{q}$ the signal signatures depends on the mass and mixing angle of the sterile neutrino. A Feynman diagram of the process is shown in figure 6.5. Assuming no significant decay length of the sterile neutrino, and thereby no detached vertex, the decay products intersect in the interaction point. Hence, the signature exclusively depends on the sterile neutrino mass M_N.

In this analysis, the focus is on the mass range $10-80$ GeV of the sterile neutrino. For low masses of the sterile neutrino, it has a high boost. As a result of the low mass and the boost, the two quarks from the sterile neutrino decay tend to be collimated. However, for high masses of the sterile neutrino, the boost is low and the two jets tend to have a large relative opening angle. Examples of event displays are shown in figure 6.6 with decays of sterile neutrinos with the masses 50 GeV and 80 GeV, together with a $Z \to q\bar{q}$ decay.

For this study, the sterile neutrino and its decay to $\mu q\bar{q}$ was introduced into PYTHIA, with the combination of q and $\bar{q}$ selected stochastically according to the CKM-matrix. After some initial trials, which did not successfully describe the final state particle multiplicity, a good decay mode was eventually identified; for technical details, see Appendix A.1. For this mode the three final state particles, μ, q, and $\bar{q}$, were distributed according to a flat phase space, i.e. not taking into account that the decay goes via an intermediate W boson. To remedy this, a more realistic phase space distribution was implemented via importance sampling.

For every event, generated with a flat phase space distribution, a weight w was calculated, comparing the matrix element squared $|\mathcal{M}|^2$ for the given event with the maximum value of the matrix element squared

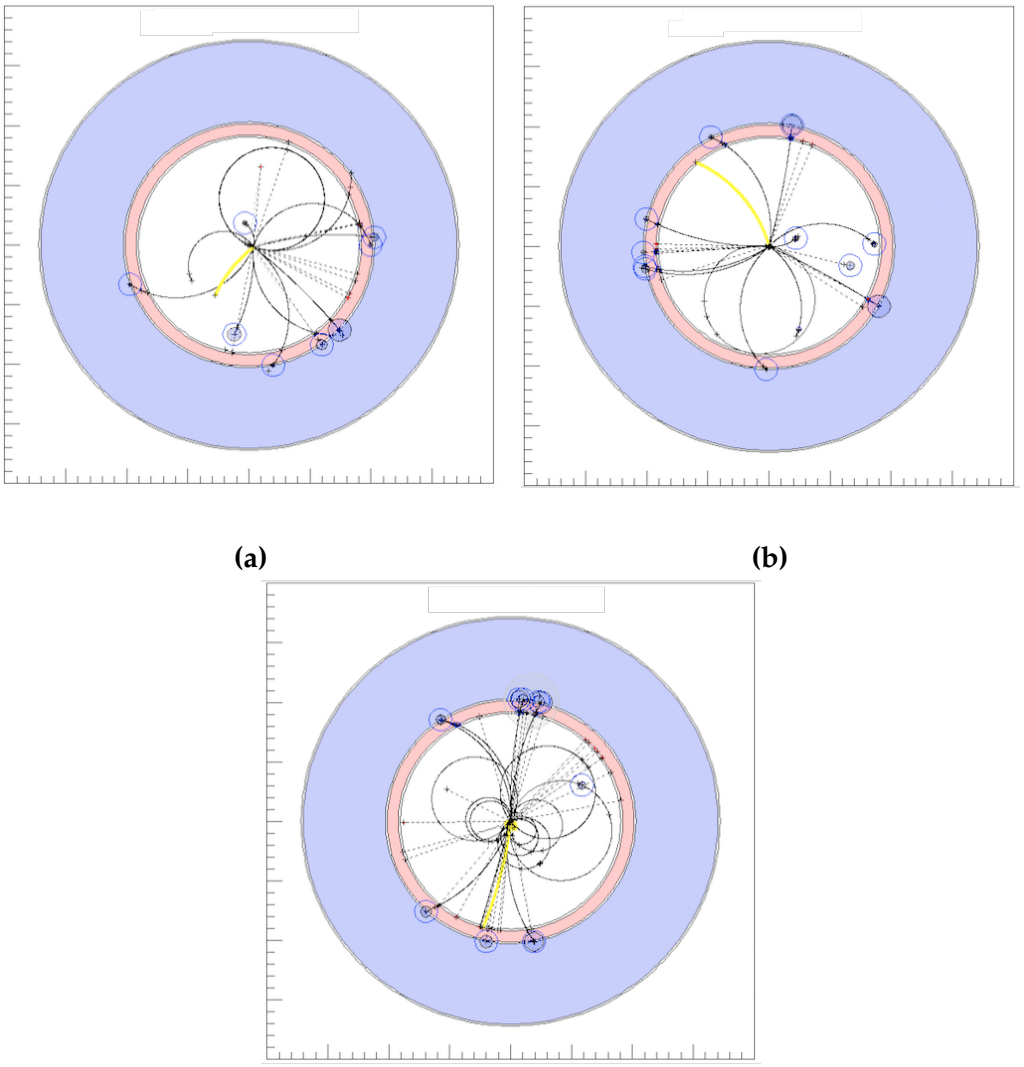

(a) **(b)**

(c)

Figure 6.6: Event displays generated with PAPAS [55], showing decays of signal events $Z \to \nu N$ with $N \to \mu q\bar{q}$ and the background process $Z \to qq$, with **(a)** $N \to \mu q\bar{q}$ decay with $m_N = 50$ GeV, **(b)** $N \to \mu q\bar{q}$ decay with $m_N = 80$ GeV, and **(c)** $Z \to qq$ decay. The yellow line represents a muon.

$|\mathcal{M}|^2_{max}$ for the total event sample, $w = \frac{|\mathcal{M}|^2}{|\mathcal{M}|^2_{max}}$. The matrix element $|\mathcal{M}|^2$ for the sterile neutrino decay has the expression [56] [4]:

$$|\mathcal{M}|^2 \propto \frac{(p_N p_{\bar{q}})(p_q p_\mu)}{((p_q + p_{\bar{q}})^2 - m_W^2)^2 + m_W^2 \Gamma_W^2} \tag{6.2}$$

Here the $p_N, p_q, p_{\bar{q}}$ and p_μ are four-momenta of the sterile neutrino, quark, anti-quark, and muon respectively, and $m_W = 80.385\,\text{GeV}$ and $\Gamma_w = 2.1$ GeV are the mass and width of the W-boson. In the the denominator of eq. (6.2), the term $((p_q + p_{\bar{q}})^2 - m_W^2)^2$ goes to zero as $m_N \to m_W$, but the term $m_W^2 \Gamma_W^2$ prevents divergence.

The importance sampling was subsequently selected by comparing w to a random number r from a flat distribution between 0 and 1. The event was saved if $w > r$.

The Breit-Wigner function of the W-boson causes an enhancement of the invariant mass of the $q\bar{q}$-system, which has a great significance for mass of the sterile neutrino, $m_N = 80$ GeV, where the W-boson can be almost on-shell. For lower masses, the significance is considerably smaller, since the W-boson is highly off-shell. This tendency is seen in figure 6.7a of the invariant mass for the 80 GeV sterile neutrinos. For lower masses of the sterile neutrino, the effect of the matrix-element-weight is not as distinct as for 80 GeV, shown for 50 GeV in figure 6.7b. The momentum is equally distributed between the three final state particles with flat phase space, whereas the momentum is varyingly distributed to the W, and thus the $q\bar{q}$ system, depending on the M_N with realistic phase space. In both plots the flat phase space distributions (black) and the matrix-element-weighted distributions (coloured) are superimposed.

[4] The matrix element is received from private communication with P. Skands. The expression is originally describing the top mass decay at a time, where it was not known that the top quark was heavier than the W boson. Due to same decay products and kinematics, the only difference is a factor three from the quark colours and a trivial change of the indices.

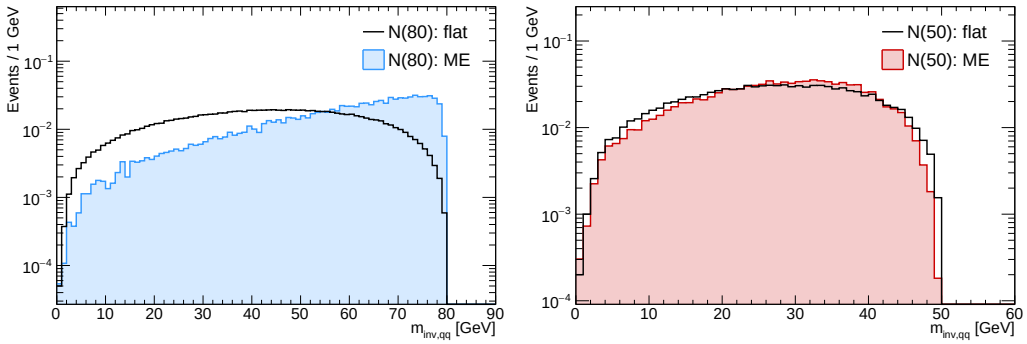

(a) **(b)**

Figure 6.7: Invariant mass of $q\bar{q}$ with flat phase space (black line) with a sample with realistic phase space (coloured) for **(a)** $m_N = 80$ GeV, and **(b)** $m_N = 50$ GeV.

6.6 Background Signatures

In the following section the background signatures and characteristic distributions are outlined. The distributions shown before pre-selection are with the prototype detector simulation and before cuts are made on missing momentum, number of charged particles, and number of muons. The remaining distributions represent the event samples after the pre-selection and with parametrised detector response. One, two, or three jets have been reconstructed for those events, depending on the sample, which is denoted at the given distribution. The selected muon is not included in the jet reconstruction.

6.6.1 Background Sample $Z \to q\bar{q}$

The dominant background is $Z \to q\bar{q}$ with $\sigma = 30$nb [18] and its Feynman diagram shown in figure 6.8. It has an average charged particle multiplicity around 20 as shown in figure 6.9a. The distributions of the cut variables missing momentum and number of muons with $p > 3$ GeV, are shown in figure 6.9b and 6.9c. $Z \to q\bar{q}$ events with a high missing momentum and a muon likely come from events where the Z decays to $b\bar{b}$ or $c\bar{c}$. The distributions in figure 6.9 are shown before a pre-selection is made, discussed further in section 6.7.

The invariant mass of the process has a peak a little below 91.2 GeV,

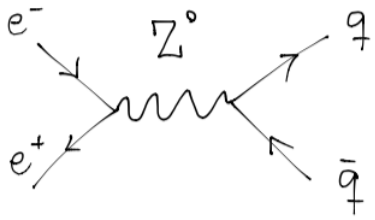

Figure 6.8: Feynman diagram of the $e^+e^- \rightarrow Z \rightarrow q\bar{q}$ background process.

the mass of the Z boson, shown in figure 6.9d. The mass peak is a bit lower than the Z mass due to the detector coverage, the loss of low momentum particles, and due to neutrinos from $Z \rightarrow b\bar{b}$ and $Z \rightarrow c\bar{c}$ decays. When the events are forced into two jets, the two jets are likely to be back-to-back, as shown in figure 6.9e with a peak around $\cos(j, j) = -1$. This distribution has a tail all the way up to values of $\cos(j, j) = 0.8$, representing atypical events that could be potential background events for the study.

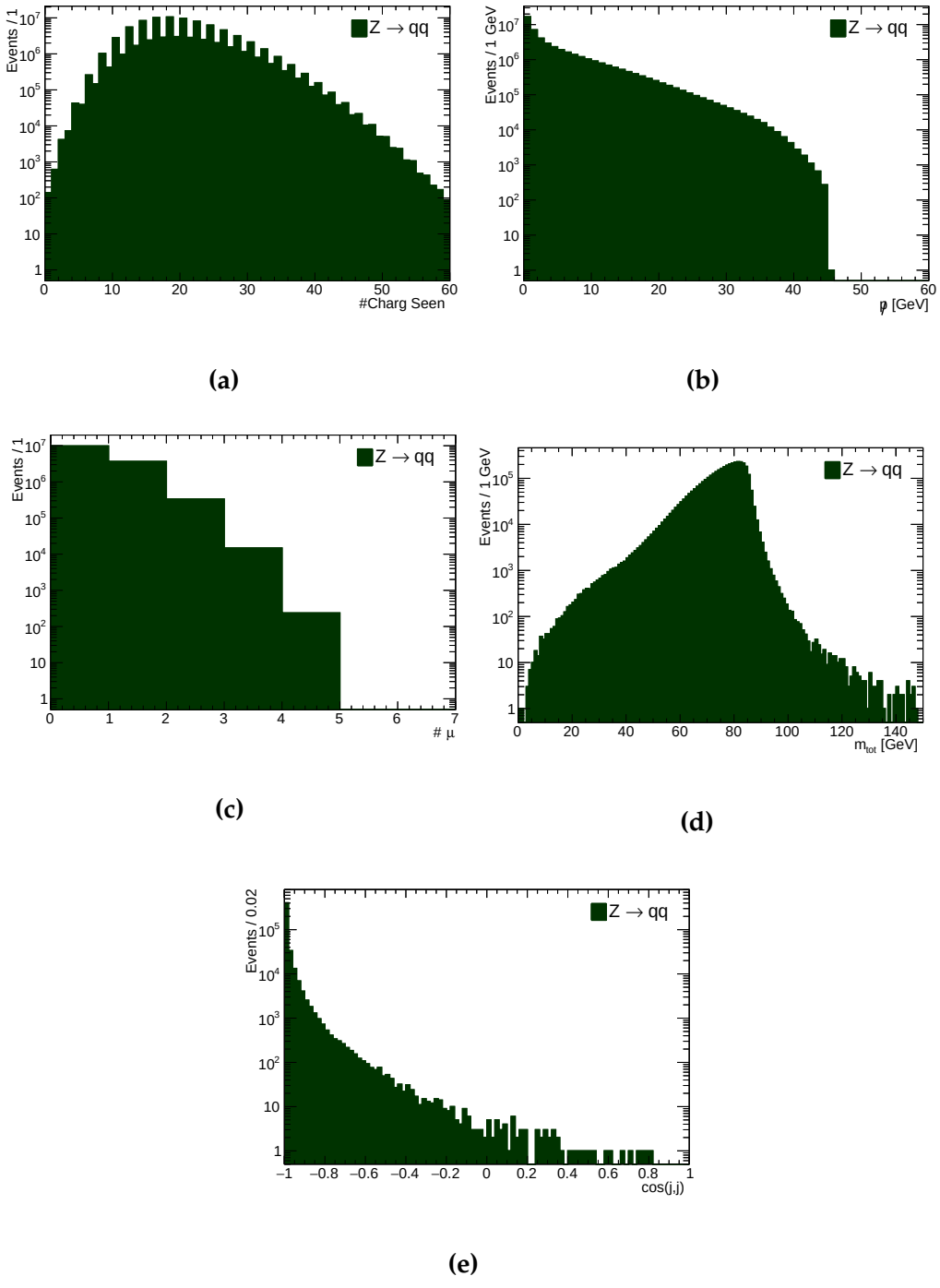

Figure 6.9: Distributions of the $Z \to q\bar{q}$ background sample with **(a)** number of charged particles seen, **(b)** missing momentum, **(c)** number of muons with $p > 3$ GeV, **(d)** the invariant mass, and **(e)** cosine of the angle between the two reconstructed jets. Distribution **(a)** and **(b)** are before the pre-selection and with the prototype detector simulation. Distribution **(c)**, **(d)**, and **(e)** are after pre-selection and parametrised detector response.

6.6.2 Background Sample $Z \rightarrow \tau^-\tau^+$

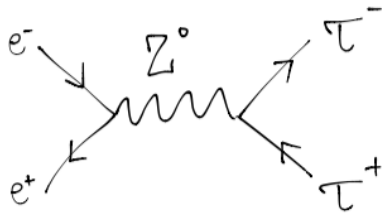

Figure 6.10: Feynman diagram of the $e^+e^- \rightarrow Z \rightarrow \tau^+\tau^-$ background process.

Figure 6.10 shows the Feynman diagram of the background, $Z \rightarrow \tau^+\tau^-$, with the process that has a cross section of $\sigma(Z \rightarrow \tau^-\tau^+) = 1.5$ nb. A total number of $5 \cdot 10^6$ $Z \rightarrow \tau^-\tau^+$ events were generated.[5]

Tau leptons decay fully leptonically $\sim$ 35%, equally shared between decays to an electron and to an muon ($\tau^- \rightarrow \nu_\tau e^- \bar{\nu}_e$ and $\tau^- \rightarrow \nu_\tau \mu^- \bar{\nu}_\mu$), and hadronically $\sim$ 65% of the time ($\tau^- \rightarrow \nu_\tau h^-$), where h^- denotes the hadronic system [6]. With the requirements of 1-2 jets, a muon, and missing momentum, one tau decaying to a muon and the other hadronically could imitate the signal. It turns out that the main reason for $Z \rightarrow \tau^-\tau^+$ being a background candidate in this search is because of initial state radiation (ISR) and final state radiation (FSR).

In figure 6.11a, the invariant mass of the visible decay products from the tau decay, are shown. Cosines of the angle between the two reconstructed jets in figure 6.11b shows a tendency to be in the same direction, most likely a one, three or five pronged forced into two jets. The relation between the muon and one of the jets is mostly back to back, shown in figure 6.11c, which indicate the scenario with one leptonic and one hadronic decay. The distribution of the maximum value of the cosine of the angle between the missing momentum and one of the forced jets, shown in figure 6.11d, indicates that the missing momentum and the jet are usually in opposite hemispheres. Since the missing momentum is depending on the neutrinos and the neutrinos from a leptonic decay ($\tau^- \rightarrow \nu_\tau e^- \bar{\nu}_e$ and $\tau^- \rightarrow \nu_\tau \mu^- \bar{\nu}_\mu$) generally carry more energy than the single tau-neutrino from a hadronic

[5] The mode "TauDecays:mode = 0" was used in PYTHIA, a model for isotropic decays, used due to time optimisation. The more realistic model in PYTHIA takes more than three orders of magnitude additional time to generate, and is thus impossible to work with considering event samples of this size. The PYTHIA authors have been made aware of this problem.

decay, the missing momentum is usually assigned in the direction of the leptonic tau-decay. Over ten times less frequently, the missing momentum is in the same direction as the jet. A similar conclusion can be drawn from figure 6.11e showing the cosine of the angle between the missing momentum and the muon: In most cases the missing momentum tends to be parallel to the muon.

6.6.3 Background Sample $Z \to \mu^-\mu^+$

As for $Z \to \tau^+\tau^-$ the cross section for $Z \to \mu^+\mu^-$ is $\sigma = 1.5$ nb, in agreement with lepton universality. A total number of $5 \cdot 10^6$ $Z \to \mu^-\mu^+$ events were generated. A Feynman diagram of the process is shown in figure 6.12b.

A priori, one would not think of $Z \to \mu^-\mu^+$ as a background, with its low charge multiplicity and clean signature. A search for very rare decays from a possible signal requires consideration of rare decays from background as well. After pre-selection, which requires at least three charged particles per event, 321 $Z \to \mu^-\mu^+$ events were left, shown in figure 6.12a. A charged particle multiplicity greater than two for $Z \to \mu^-\mu^+$ is seemingly caused by initial state radiation ISR and final state radiation FSR, with a high probability of pair production, $\gamma \to e^+e^-$, or a decay to two muons. In the case of a radiated photon with $\gamma \to q\bar{q}$, PYTHIA might be hadronising the event, resulting in a higher charged particle multiplicity.

6.6.4 Background Samples for Four-fermion Processes

The four-fermion processes considered for the background sample have been divided into the two processes: $e^+e^- \to e^+e^-q\bar{q}$ and $e^+e^- \to q\bar{q}\mu\nu$.

Background Sample $e^+e^- \to e^+e^-q\bar{q}$

The process $e^+e^- \to e^+e^-q\bar{q}$ includes mainly two processes, two photon processes shown as Feynman diagram in figure 6.13a and Z decays with a radiative photon shown in figure 6.13b and 6.13c. Since the phase space is complicated to calculate for the two photon processes, the events were generated with WHIZARD, for each quark flavour separately with a requirement of an invariant mass of the quark pair greater than 15 GeV. WHIZARD only takes initial and final state particles as input, which is why the inclusive process $e^+e^- \to e^+e^-q\bar{q}$ was generated and had a total cross section of $\sigma = 125.40$ pb, resulting in a total number of 418,013 events.

For high masses of the final state quark pairs, the process tends to be mediated by a Z-boson decaying hadronically with either initial or final

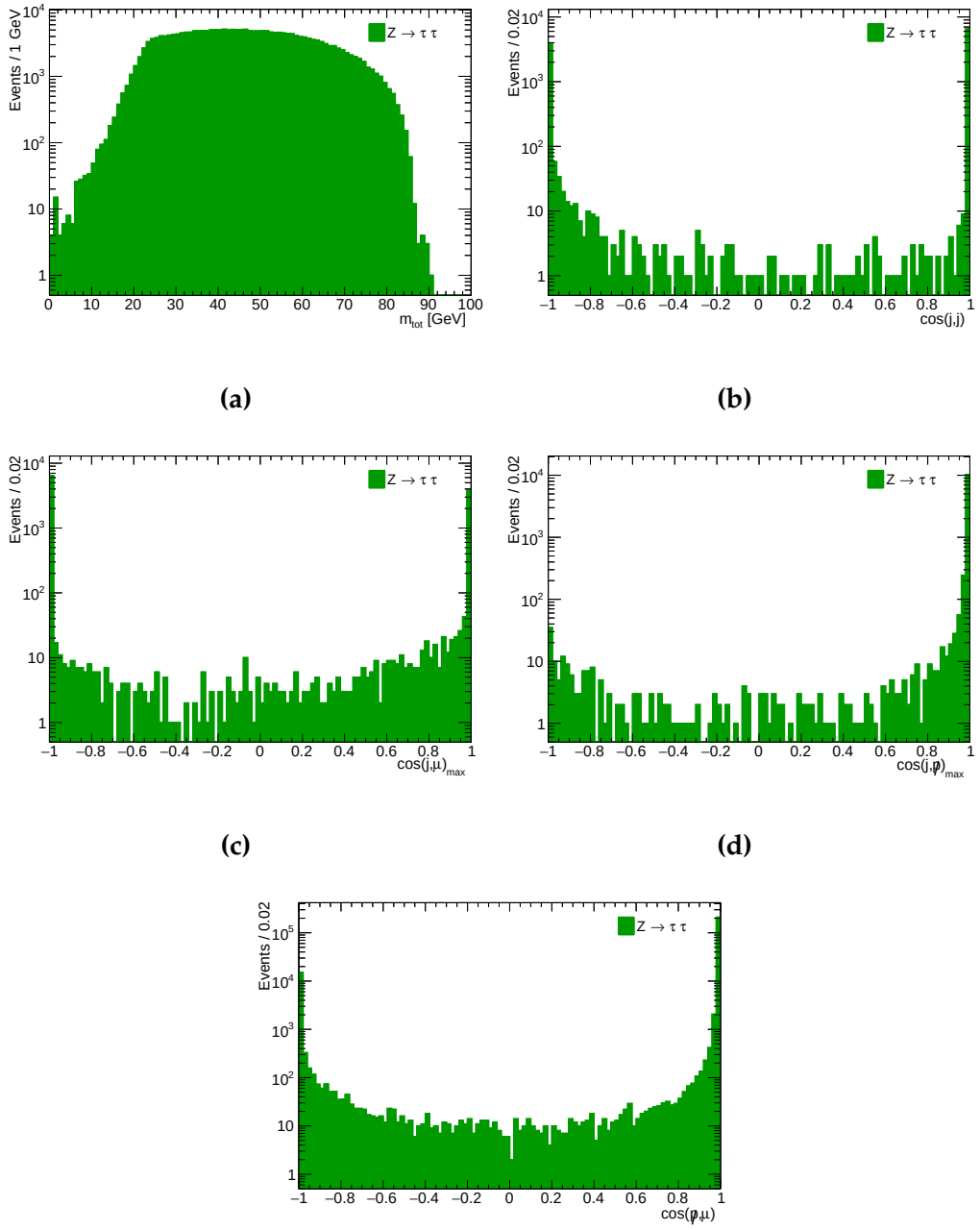

(a) **(b)**

(c) **(d)**

(e)

Figure 6.11: Distributions of the $Z \to \tau^+\tau^-$ background sample **(a)** invariant mass, **(b)** cosine of the angle between the two reconstructed jets, **(c)** the maximum value of cosine of the angle between the muon and one of the two reconstructed jets, **(d)** the maximum value of cosine of the angle between missing momentum and one of the two reconstucted jets, **(e)** cosine of the angle between missing momentum and the muon. All distributions are after pre-selection and parametrised detector response.

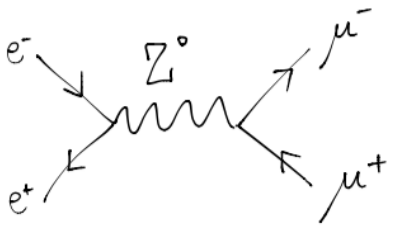

(a)

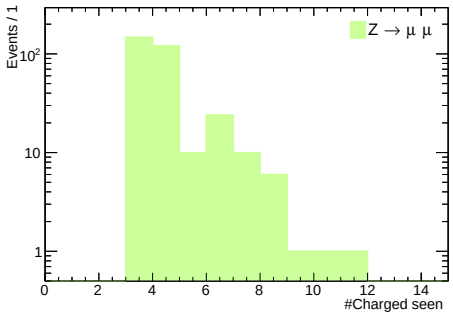

(b)

Figure 6.12: (a) Feynman diagram of the $e^+e^- \to Z \to \mu^+\mu^-$ background process. **(b)** Number of charged particles seen for $e^+e^- \to Z \to \mu^+\mu^-$ after pre-selection and parametrised detector response.

state radiation. In order to minimize double counting from events already generated in the $Z \to q\bar{q}$ sample, all events from the $e^+e^- \to e^+e^-q\bar{q}$ sample with an invariant mass larger than 50 GeV were excluded. In figure 6.14 the invariant mass of $e^+e^-q\bar{q}$ is shown before the cut. For low masses of the final state quark pairs, the production tends to come from a two photon process.

Background Sample $e^+e^- \to q\bar{q}\mu\nu$

The four-fermion process $e^+e^- \to q\bar{q}\mu\nu$ has a cross section of only $\sigma = 4.20$ fb at the Z-pole energy. To get better statistics, the luminosity was scaled with a factor 10^3, resulting in 14,009 generated events. An invariant mass of $q\bar{q}$ above 5 GeV was required as well as $|\cos(\theta)| > 0.99$ for the muon. In figure 6.15 Feynman diagrams of some of the main contributing $e^+e^- \to q\bar{q}\mu\nu$ background processes are shown. Processes with same final state but with a production of two W bosons have a vanishing cross section below the WW threshold, and do thus not contribute as a background.

The invariant mass of the $q\bar{q}$ system, is shown in figure 6.16 at generator level. The $q\bar{q}$ system has a peak around 80 GeV indicating a radiative W-boson decaying hadronically. The distribution of missing momentum before the pre-selection cuts, is shown in figure 6.17a. In figure 6.17b, 6.17c and 6.17d are the distributions of the total invariant mass, cosine of the angles between the two jets and cosine of the angle between the muon and missing momentum shown, respectively, all after parametrised detector

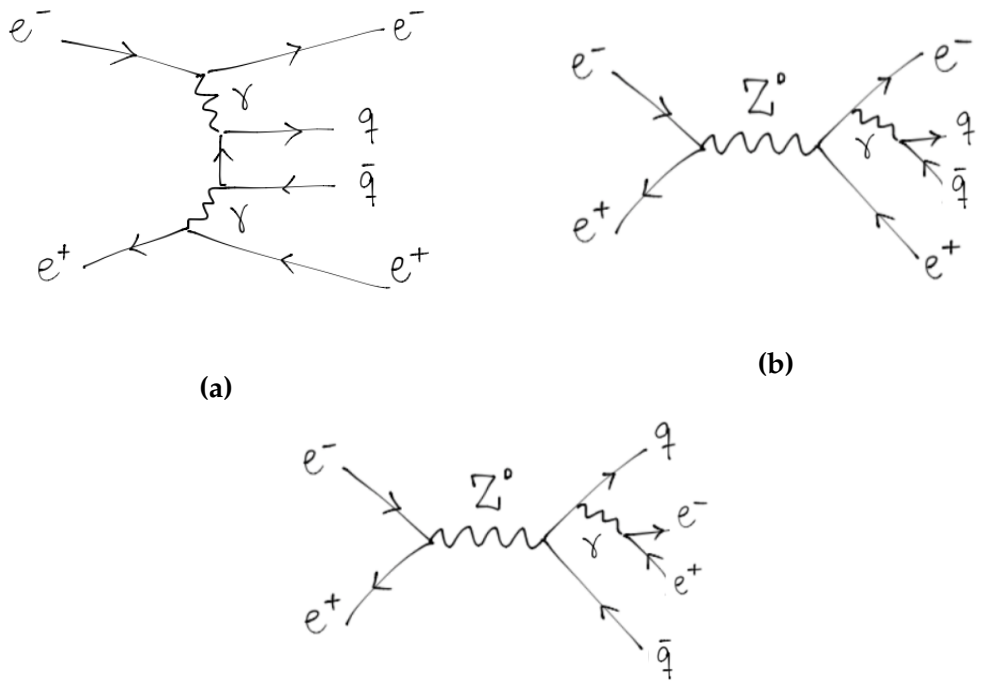

Figure 6.13: Feynman diagrams of the $e^+e^- \rightarrow e^+e^-q\bar{q}$ background process, produced by **(a)** a two photon process, **(b)** a Z-decay to e^+e^- with a radiative photon decaying to $q\bar{q}$, and **(c)** a Z-decay to $q\bar{q}$ with a radiative photon decaying to e^+e^-.

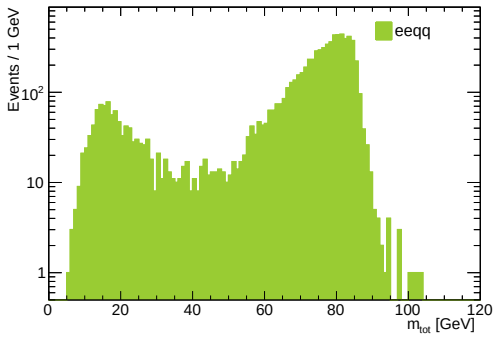

Figure 6.14: Invariant mass of $e^+e^-q\bar{q}$, after pre-selection and parametrised detector response.

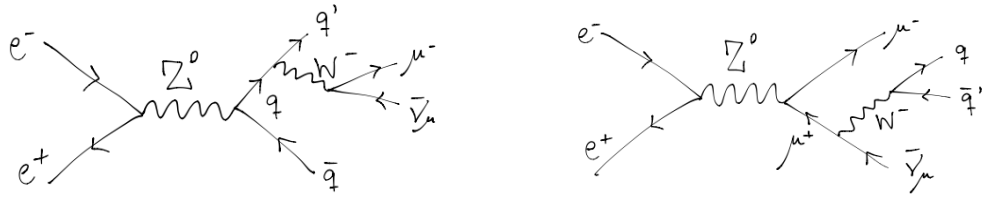

(a) **(b)**

Figure 6.15: Feynman diagrams of the four-fermion background $e^+e^- \rightarrow q\bar{q}\mu\nu$ process.

response. The peak appearing for the invariant mass of the $q\bar{q}$ system in figure 6.16 does not appear on the distribution for the total invariant mass in figure 6.17b. This is likely due to the case of the events at the peak having low missing momentum and thus discarded in the pre-selection. Since the signal signature is expected as correlated peaks for the $\not{p}$ and m_{tot} distributions, it is a challenge that the $e^+e^- \rightarrow q\bar{q}\mu\nu$ events have flat distributions for those parameters.

All $e^+e^- \rightarrow q\bar{q}\nu\mu$ histograms in this section are scaled by a factor 1000 times higher luminosity, due to the very low cross section of the process. This is later scaled to the correct luminosity in the analysis.

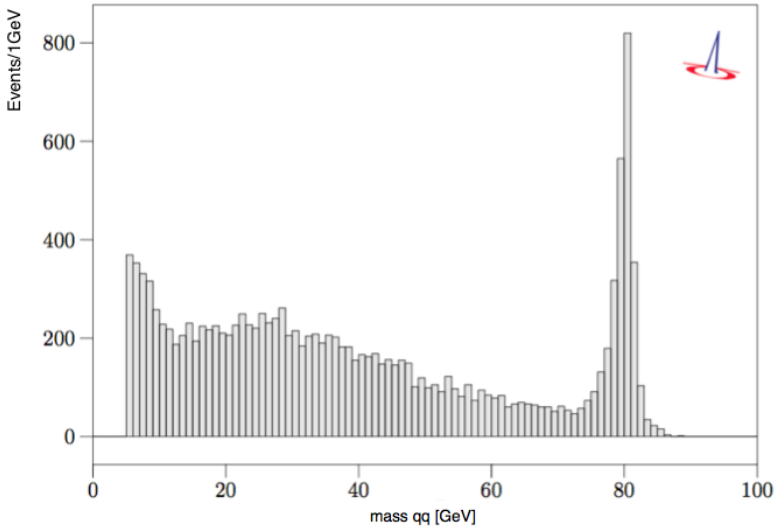

Figure 6.16: Invariant mass of the $q\bar{q}$ system for $e^+e^- \rightarrow \mu^-\bar{\nu}_\mu q\bar{q}$ at generation level.

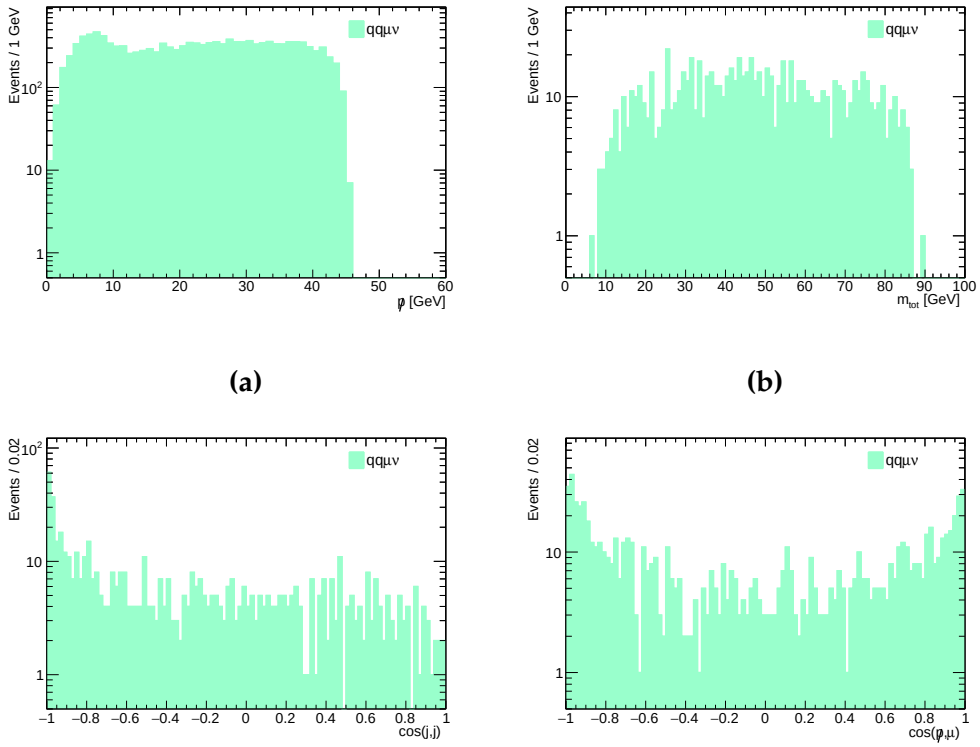

(a) **(b)**

(c) **(d)**

Figure 6.17: Distributions of the four-fermion background $e^+e^- \to q\bar{q}\nu\mu$ process, which are all scaled by a factor 1000 in order to get enough statistics due to the very low cross section. The distributions are **(a)** missing momentum, **(b)** total invariant mass, **(c)** cosine of the angle between the two reconstructed jets, and **(d)** cosine of the angle between the missing momentum and the muon. Distribution **(a)** is shown before pre-selection and with the prototype detector simulation. Distribution **(b)**, **(c)**, and **(d)** are after pre-selection and parametrised detector response.

6.7 Pre-selection

For the pre-selection three requirements were imposed:

1. At least 3 charged particles
2. Missing momentum larger than 5 GeV
3. At least one muon with momentum larger than 3 GeV

Distributions of the three variables are shown in figure 6.18. The statistics of the cut-flow is shown in table 6.1 for background, and table 6.2 for signal.

The signal has a signature of large missing momentum as well as a muon with high momentum, which distinguish signal from background to a large extent. After pre-selection only $\sim 4-5\%$ of the main background events, $Z \to q\bar{q}$, were left whereas the signal efficiency varied between $81-98\%$ depending on the mass.

Process:	$Z \to q\bar{q}$	$Z \to \tau^+\tau^-$	$Z \to \mu^+\mu^-$	$e^+e^-q\bar{q}$	$q\bar{q}\mu\nu$
Initial:	10^8	$5 \cdot 10^6$	$5 \cdot 10^6$	$4.1801 \cdot 10^5$	14.01
≥ 3 ch. part.	$9.9995 \cdot 10^7$	$1.4857 \cdot 10^6$	$1.6563 \cdot 10^4$	$3.2417 \cdot 10^5$	13.91
$p_{miss} > 5$ GeV	$1.3879 \cdot 10^7$	$1.1387 \cdot 10^6$	334	$1.0335 \cdot 10^5$	13.08
$\geq 1\ \mu, p > 3$ GeV	$4.0253 \cdot 10^6$	$2.3257 \cdot 10^5$	331	9139	0.80

Table 6.1: Statistics of the cut-flow for pre-selection for background events.

Process:	N10	N20	N30	N40	N50	N60	N70	N80
Initial:	10000	10000	10000	10000	10000	10000	10000	10000
≥ 3 ch. part.	9221	9772	9898	9941	9969	9974	9988	9995
$p_{miss} > 5$GeV	9219	9770	9895	9940	9967	9971	9981	9919
$\geq 1\ \mu$, p>3GeV	8194	8971	9532	9703	9774	9793	9782	9238

Table 6.2: Statistics of the cut-flow for pre-selection for signal events.

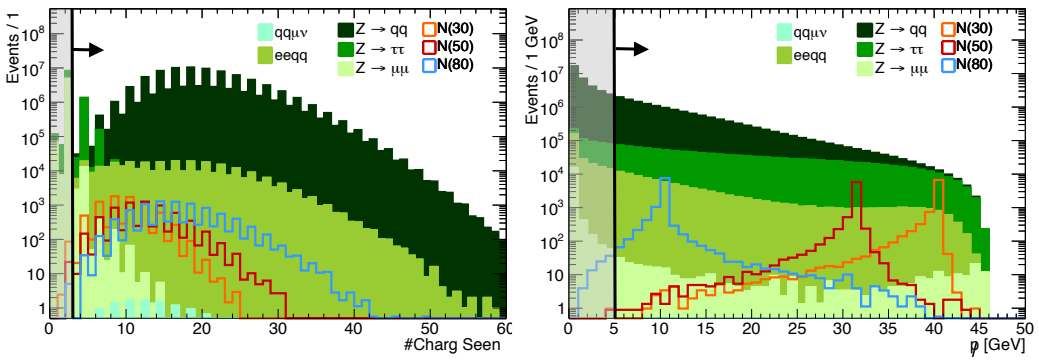

(a) **(b)**

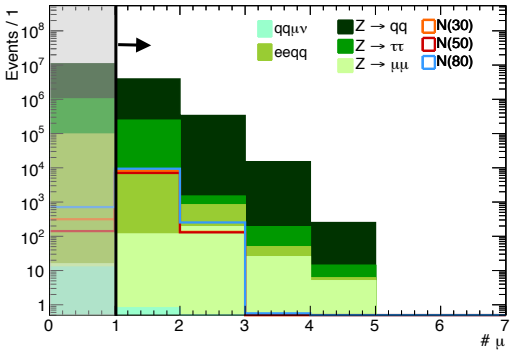

(c)

Figure 6.18: Distributions of the cut-variables for the pre-section are shown after the preceding cut in the pre-selection sequence was applied. The lines with an arrow indicate the cuts, where the shaded areas indicate discarded events. The distributions show **(a)** number of charged particles seen, **(b)** the missing momentum, and **(c)** number of muons with $p > 3$ GeV.

6.8 Low Mass Analysis

The analysis for low masses of the sterile neutrinos (LM) was performed for masses of the sterile neutrino in the range 10 – 30 GeV. A sketch of the cut-flow is shown in figure 6.19.

Exactly 1 muon with momentum $p > 3$ GeV was required. In figure 6.20a the distribution of number muons with momentum > 3 GeV is shown. To avoid background events with high missing momentum due to undetected particles going close to the beam line a cut on $|\cos(\theta_{\not p})| < 0.94$ was performed. This cut ensures a vigorous definition of $\not p$ in order to avoid that missing momentum are due to the small gab in the detector close to the beam axis. The distribution of $|\cos(\theta_{\not p})|$ is shown in figure 6.20b.

For the signals with low masses, the missing momentum tends to be in the hemisphere opposite from the muon. In $Z \to q\bar{q}$ processes with b and c decays, the muon and neutrino have momentum in same direction. The same argument holds for a leptonic tau decay. Hence, the cosine of the angle between $\not p$ and the muon is required to be less than $\cos(\not p, \mu) < 0.50$, as shown in figure 6.20c.

For the jet reconstruction, the exclusive jets option of the jet reconstruction algorithm was employed to require the reconstruction of exactly one jet with minimum 1 charged particle and energy of $E > 3$ GeV, since the signal for low masses tends to have a mono-jet signature. Here and everywhere else the identified muon was excluded from the jet finding algorithm.

The main background $Z \to q\bar{q}$ with the highest cross section, tends to decay to two jets in opposite hemispheres. To reduce this background, all events which were just reconstructed a one-jet events were now attempted reconstructed as two-jet events with the same requirements as before on each jet: at least 1 charged particle and $E_{\text{jet},i} > 3$ GeV. This way the total sample was divided into two sub-samples depending on whether or not the reconstruction of two jets was successful. Different cuts were then applied to these two sub-samples, as indicated in figure 6.19.

For those events possible to construct two jets a requirement on $\cos(j, j) > -0.80$ was applied. For the remaining events, where two jets could not be constructed, no cuts were applied. The cosine of the angle between the two constructed jets is shown in figure 6.21a.

In boosted N-decay, the muon is approximately in the same direction as the reconstructed jet(s). For the background samples, the muon tends to be either inside one of the jets as for the $Z \to q\bar{q}$ background, when forcing two jets in the events, or the muon tends to be in the opposite hemisphere of the jets as for the $Z \to \tau^+\tau^-$ events, where one tau decay leptonically and the other hadronically. Hence, a requirement of $-0.50 < \max(\cos(jet, \mu)) < 0.96$ was applied, as shown in figure 6.21b. Here the $\max(\cos(jet, \mu))$ variable is defined as the maximum cosine value when considering the two jets in events where the two-jet reconstruction succeeded. For events where this failed, there is no maximum value to be taken, of course. For this sub-sample, the same cut was applied for the angle between the muon and jet, $-0.50 < \cos(jet, \mu) < 0.96$, as seen in figure 6.21c.

Lastly, the mass of the jet in the one-jet reconstruction, is demanded in the interval 1.8 GeV $< m_{jet} <$ 30 GeV, as shown in figure 6.21d. The jet mass of the signal can take a maximum value of 30 GeV, whereas a large amount of the $Z \to q\bar{q}$ and $Z \to \tau^+\tau^-$ events have higher jet masses. The lower bound is set due to the tau mass of 1.777 GeV.

The statistics of the cut-flow for the low mass analysis is shown in table 6.3.

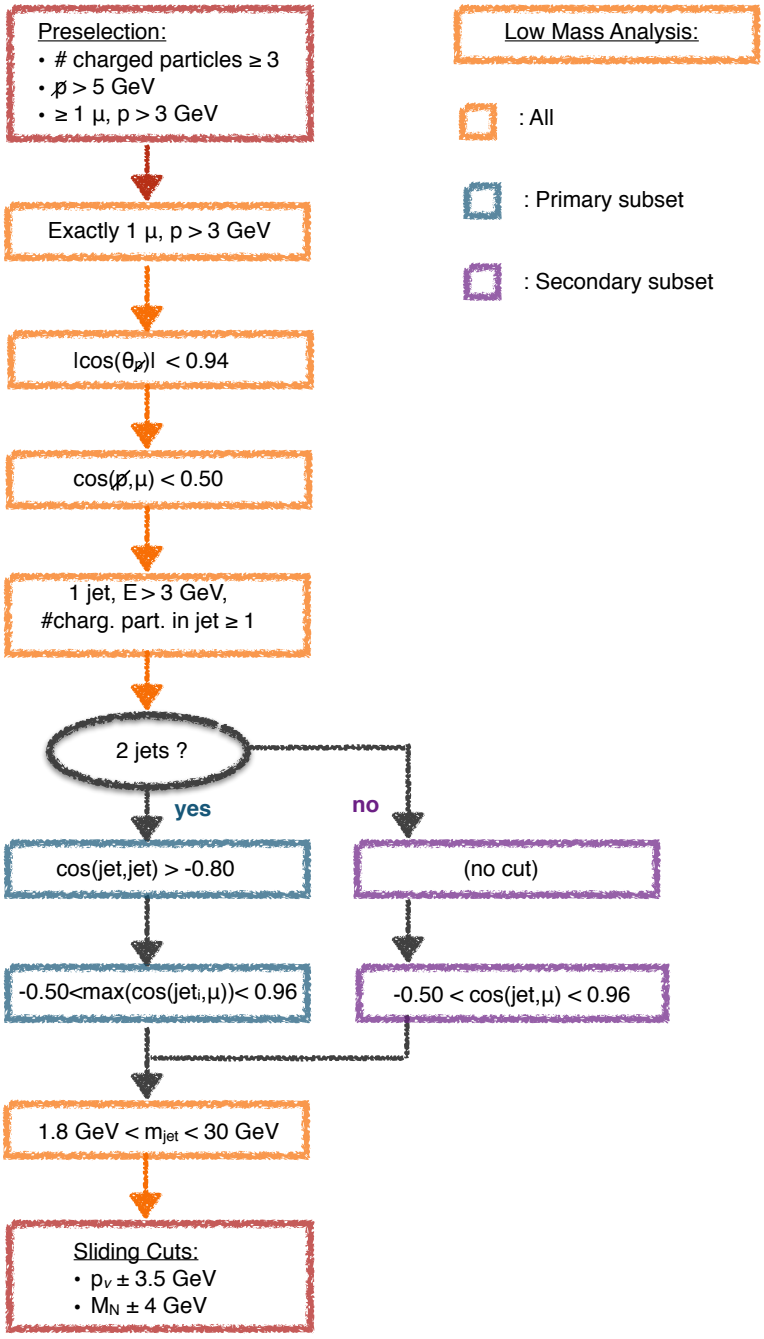

Figure 6.19: Sketch of the cut-flow for the low mass analysis.

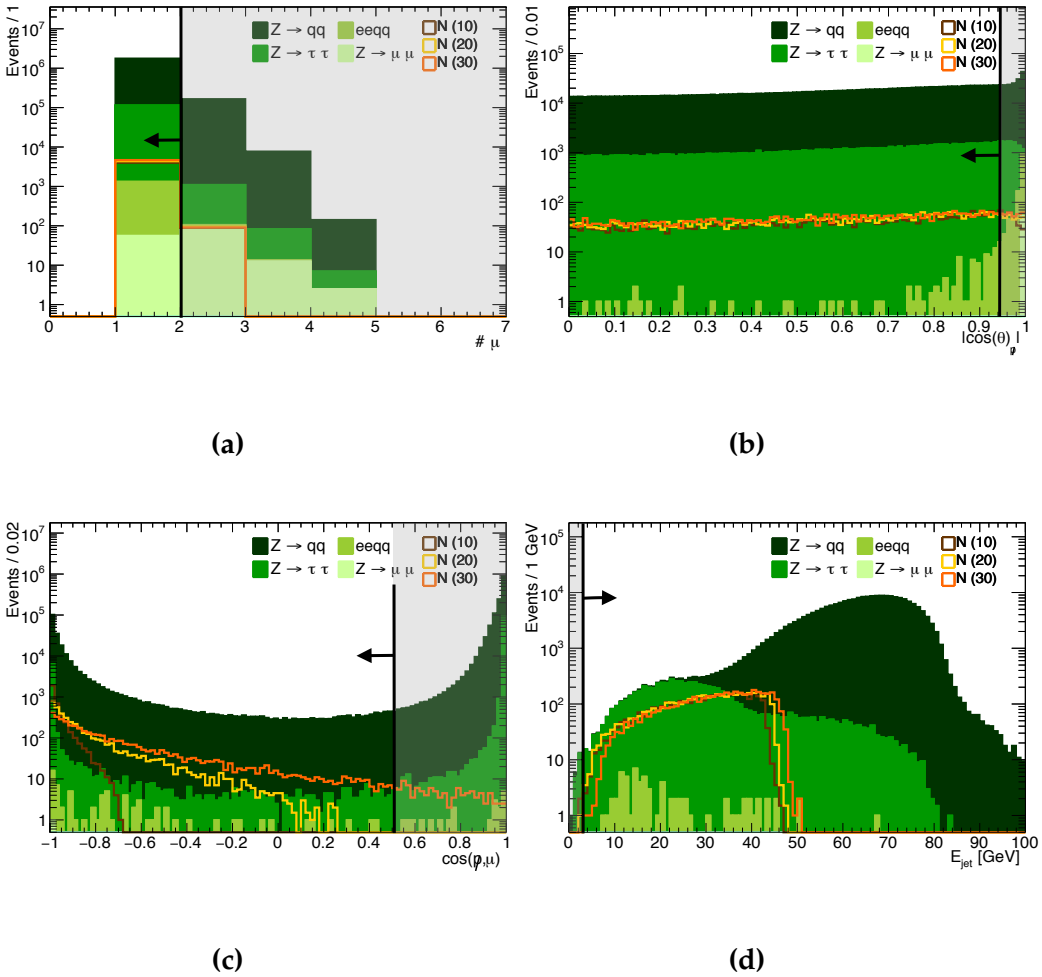

Figure 6.20: Distributions of the cut-variables for the low mass analysis, shown after preceding cuts from the sequence in the cut-flow (in figure 6.19) were applied. The lines with an arrow indicate the cuts, where the shaded areas indicate discarded events. The distributions show **(a)** number of muons with $p > 3$ GeV, **(b)** the absolute value of cosine of the angle of the missing momentum, $|\cos(\theta_{\not p})|$, **(c)** cosine of the angle between the missing momentum and the muon, $\cos(\not p, \mu)$, and **(d)** the energy of the one reconstructed jet, E_{jet}.

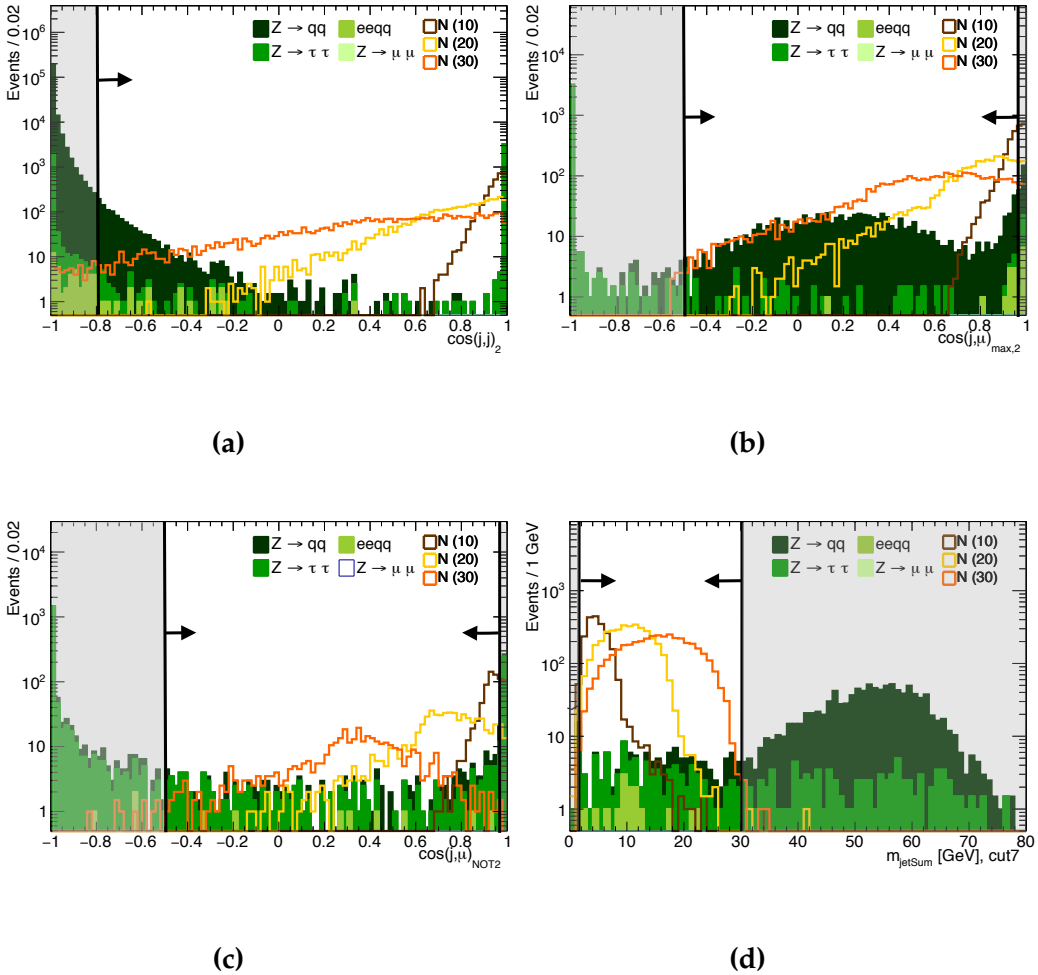

(a) **(b)**

(c) **(d)**

Figure 6.21: Distributions of the cut-variables for the low mass analysis, shown after preceding cuts from the sequence in the cut-flow (in figure 6.19) were applied. The lines with an arrow indicate the cuts, where the shaded areas indicate discarded events. The distributions show **(a)** cosine of the angle between two forced jets, $\cos(j, j)$, **(b)** the maximum value of cosine of the angle between one of the two forced jets and the muon $\max(\cos(j, \mu))$, **(c)** cosine of the angle between the muon and one jet, for the events not adequate to construct two jets, $\cos(j, \mu)_{NOT2}$, and **(d)** the mass of the one reconstructed jet, m_{jet}.

Process:	$Z \to q\bar{q}$	$Z \to \tau^+\tau^-$	$Z \to \mu^+\mu^-$	$e^+e^- q\bar{q}$	$q\bar{q}\mu\nu$	N10	N20	N30
Generated events:	10^8	$5 \cdot 10^6$	$5 \cdot 10^6$	$4.1801 \cdot 10^5$	14.01	10000	10000	10000
After pre-selection:	3690262	229806	321	1288	0.85	8153	8914	9488
Exactly 1 μ, $p > 3$ GeV	3343354	227661	112	1270	0.844	7974	8723	9307
$\lvert\cos(\theta_{\not p})\rvert < 0.94$	3022270	211449	4	92	0.802	7387	8114	8607
$\cos(\not p, \mu) < 0.50$	443156	14859	4	72	0.542	7387	8114	8382
1 jet, $E > 3$ GeV, no.charg.part.≥ 1	443124	14823	3	72	0.542	7383	8112	8382
Events with 2 jets	*442791*	*10767*	3	*61*	*0.501*	*5974*	*6810*	*7579*
cos(jet,jet) > -0.80	*2280*	*6659*	2	*17*	*0.344*	*5974*	*6810*	*7472*
$-0.50 < \max(\cos(\text{jet}, \mu)) < 0.96$	*1878*	*104*	*1*	*9*	*0.265*	*3160*	*6115*	*7163*
Events with 1 jet only	333	*4056*	*0*	*11*	*0.041*	*1409*	*1302*	*803*
$-0.50 < \cos(\text{jet}, \mu) < 0.96$	*92*	*271*	*0*	*8*	*0.032*	*974*	*1230*	*776*
Total after preceding cuts	1970	375	1	17	0.297	4134	7345	7939
1.8 GeV $< m_{\text{jet}} < 30$ GeV	78	145	0	15	0.199	4058	7303	7913

Table 6.3: Statistics of the cut-flow for the low mass analysis.

6.9 High Mass Analysis

The high mass analysis was applied for signals with masses 30, 40, 50, 60, 70, and 80 GeV. A sketch of the cut-flow diagram is shown in figure 6.23. The signal tends to have a di-jet signature for signal masses greater than 30 GeV, which is why the analysis is based on a reconstruction of two jets for all events.

As for the low mass analysis, exactly 1 muon with momentum greater than 3 GeV was required, and the absolute value of the angle of the missing momentum was required to be less than 0.94. The distributions of number of muons with $p > 3$ GeV, and $|\cos(\theta_{\not p})|$ are shown in figure 6.22a and 6.22b, respectively.

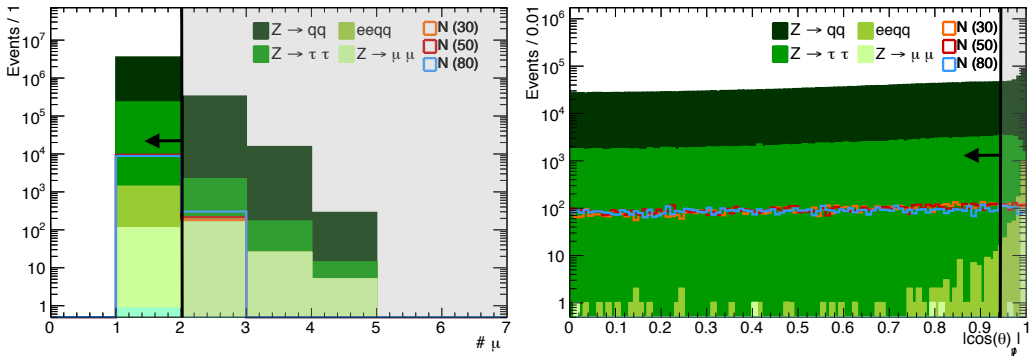

(a) **(b)**

Figure 6.22: Distributions of the cut-variables for the high mass analysis, shown after preceding cuts from the sequence in the cut-flow (in figure 6.23) were applied. The lines with an arrow indicate the cuts, where the shaded areas indicate discarded events. The distributions show **(a)** number of muons with $p > 3$ GeV, and **(b)** the absolute value of cosine of the angle of the missing momentum, $|\cos(\theta_{\not p})|$.

To discriminate against against $Z \to c\bar{c}$ and $Z \to b\bar{b}$ events, where a heavy quark decays semileptonically. e.g. $b \to c\mu\bar{\nu}_\mu$, and against $Z \to \tau^+\tau^-$ events, a requirement was made for $\cos(\not p, \mu) < 0.80$, as shown in figure 6.24a.

For the considered mass range above 30 GeV, the signals tend to have a di-jet signature, hence all events were forced into exactly two jets. Each jet was required to include at least one charged particle, and have an energy of at least 3 GeV. The reconstructed muon was not included in the jet reconstruction. The distribution of the minimum jet energy is shown in figure 6.24b.

The angular distribution between the two jets was required to be in the interval between $-0.80 < \cos(\text{jet,jet}) < 0.98$ shown in figure 6.24c. The low boundary was set considering the back-to-back signatures of jets coming from $Z \to q\bar{q}$ and $Z \to \tau^+\tau^-$ with both τs decaying hadronically. The upper bound was set due to mono-jets from $Z \to \tau^+\tau^-$ forced into two jets.

A background contribution consists of $Z \to c\bar{c}$ and $Z \to b\bar{b}$ events where a heavy quark decays semileptonically. This background can be suppressed by observing that in such events the lepton from the heavy quark decay tends to be in geometrical proximity to the associated jet. Hence a requirement on the minimum distance between the muon and the closest jet comes to mind. One problem with this is, that all events have been forced into a two-jet topology, and thus in the case of a hard gluon radiation this does not give a realistic picture of the event. To circumvent this, events were now (attempted to be) reconstructed as three-jet events before the cut of the maximum value of cosine of the angle between the muon and one of the three jets, $\max(\cos(jet_i, \mu)) < 0.80$, was applied, as shown in figure 6.25a.

For the sub-sample of events incapable of forming three jets, the same requirement on a maximum value of the cosine to the angle between the muon and one of the two reconstructed jets, $\max(\cos(jet_i, \mu)) < 0.80$, was made, shown in figure 6.25b.

To check the co-planarity of the events, yet again, a sub-sample of events possible to construct three jets, was required to have an angular sum between the three jets below $\sum_{i,j}(\text{jet}_i, \text{jet}_j) < 300^\circ$ for $i, j = 1, 2, 3$, shown in figure 6.25c. The lower the signal mass, the more a-coplanar the events were due to the energy of the active neutrino produced in association with the sterile neutrino. For the remaining events, incapable of forming three jets, no cuts were applied.

Finally a cut was made for the minimum jet mass $m_{\text{jet,min}} > 1.8$ GeV, shown in figure 6.25d, to discriminate against hadronic τ decays, with its mass of 1.777 GeV.

The statistics of the cut-flow for the high mass analysis is shown for the background and signal in table 6.4 and 6.5, respectively.

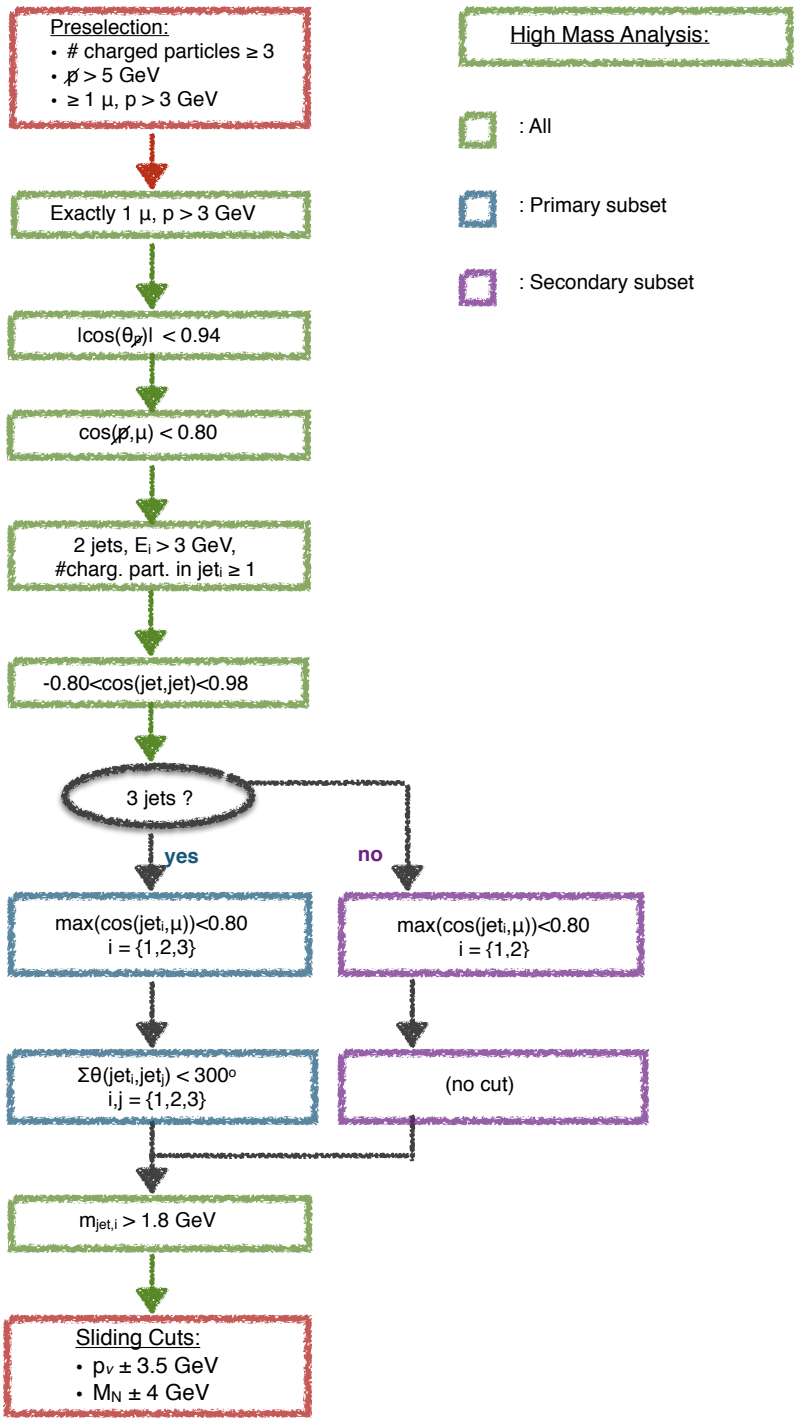

Figure 6.23: Sketch of the cut-flow for the high mass analysis.

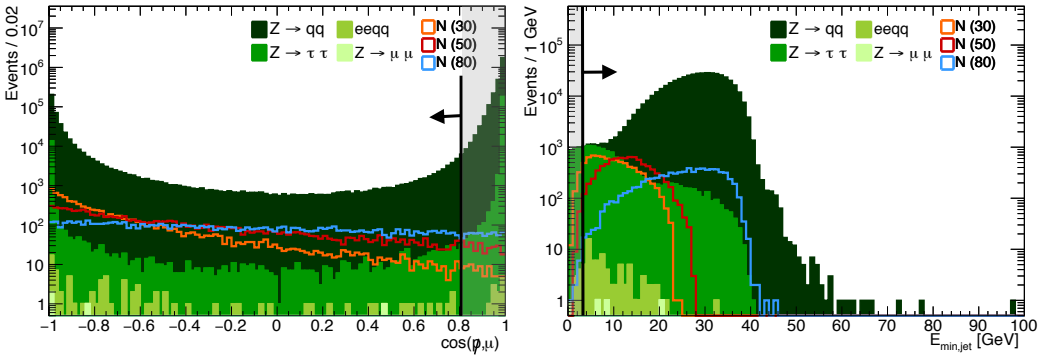

(a) **(b)**

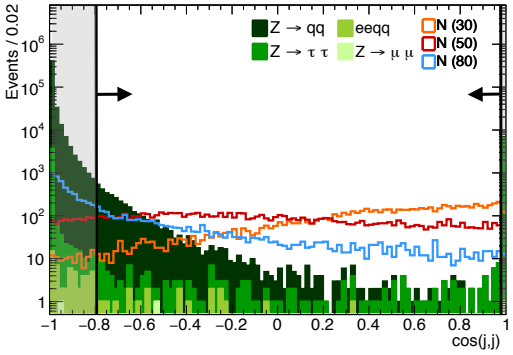

(c)

Figure 6.24: Distributions of the cut-variables for the high mass analysis, shown after preceding cuts from the sequence in the cut-flow (in figure 6.23) were applied. The lines with an arrow indicate the cuts, where the shaded areas indicate discarded events. The distributions show **(a)** cosine of the angle between the missing momentum and the muon, cos($\not{p}$, μ), and **(b)** the minimum jet energy of the two reconstructed jets, min(E_{jet}), and **(c)** cosine of the angle between two reconstructed jets, cos(jet,jet).

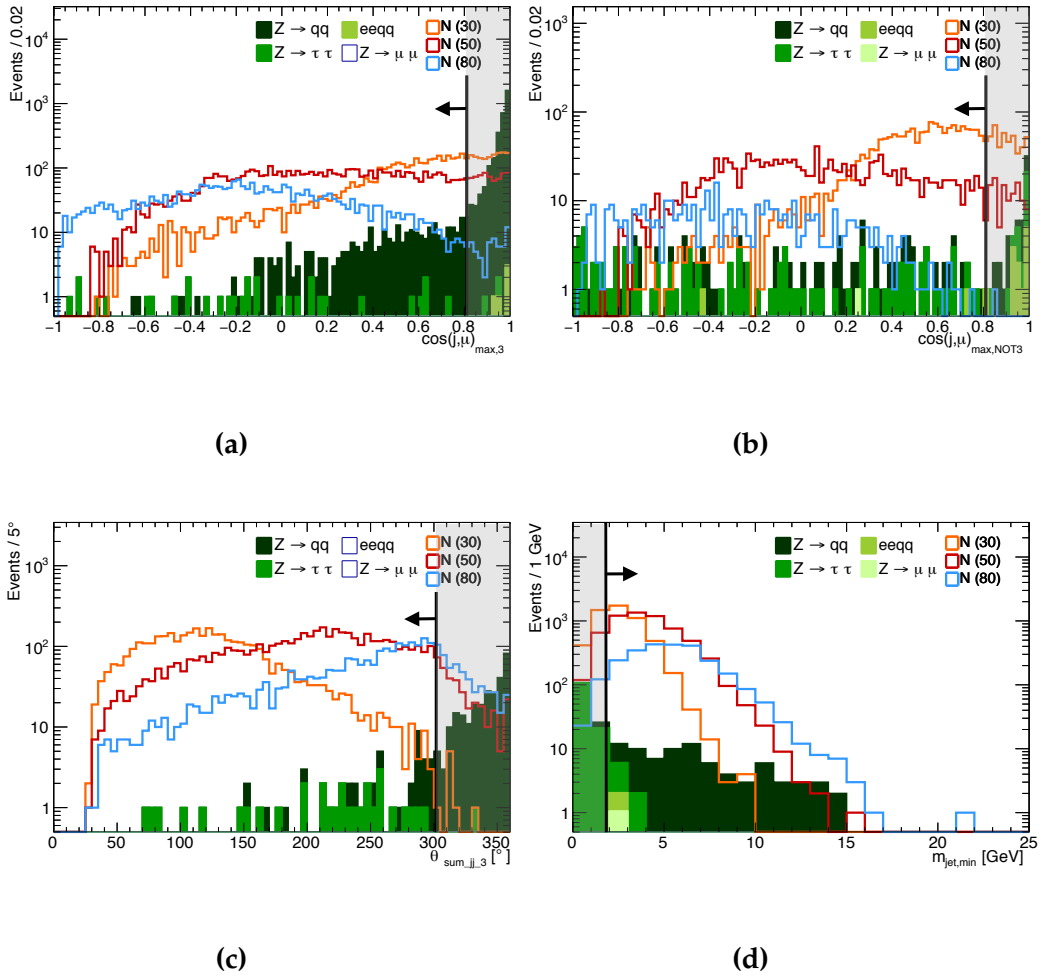

Figure 6.25: Distributions of the cut-variables for the high mass analysis, shown after preceding cuts from the sequence in the cut-flow (in figure 6.23) were applied. The lines with an arrow indicate the cuts, where the shaded areas indicate discarded events. The distributions show **(a)** the maximum value of cosine of the angle between one of the three forced jets and the muon $\max(\cos(j_i, \mu))$ with $i = 1, 2, 3$, **(b)** the maximum value of cosine of the angle between the muon and one of the two jets, for the events not adequate to construct three jets, $\max(\cos(j_i, \mu)_{NOT2})$ with $i = 1, 2$, **(c)** the sum of the angles between the three forced jets, $\sum_{i,j} \theta_{\text{jet}_i,\text{jet}_j}$ with $i, j = 1, 2, 3$, and **(d)** the minimum jet mass of the two reconstructed jets, $\min(m_{\text{jet}})$.

Process:	$Z \to q\bar{q}$	$Z \to \tau^+\tau^-$	$Z \to \mu^+\mu^-$	$e^+e^-q\bar{q}$	$q\bar{q}\mu\nu$
Generated events:	10^8	$5 \cdot 10^6$	$5 \cdot 10^6$	$4.1801 \cdot 10^5$	14.01
After pre-selection:	3690262	229806	321	1288	0.85
Exactly 1 μ, $p > 3$ GeV	3343354	227661	112	1270	0.844
$\lvert\cos(\theta_{\not p})\rvert < 0.94$	3022270	211449	4	92	0.802
$\cos(\not p, \mu) < 0.50$	473300	15136	4	81	0.645
2 jets, $E_i > 3$ GeV,no.ch.part. in jet$_i \geq 1$	472877	10741	3	70	0.603
cos(jet, jet) > -0.80	3456	161	1	19	0.41
Events with 3 jets	3379	34	0	5	0.295
$\max(\cos(\text{jet}_i, \mu)) < 0.80$	298	32	0	0	0.162
$\sum_{i,j} \theta(\text{jet}_i, \text{jet}_j) < 300°$	26	31	0	0	0.147
Events with 2 jets only	77	127	1	14	0.115
$\max(\cos(\text{jet}_i, \mu)) < 0.80$	53	104	1	2	0.081
Total after preceding cuts	79	135	1	2	0.228
$m_{\text{jet}} > 1.8$ GeV	75	6	1	1	0.19

Table 6.4: Statistics of the cut-flow for the high mass analysis with background events.

Process:	N30	N40	N50	N60	N70	N80
Generated events:	10000	10000	10000	10000	10000	10000
After pre-selection:	9488	9643	9729	9731	9735	9162
Exactly 1 μ, $p > 3$ GeV	9307	9428	9514	9476	9444	8859
$\lvert\cos(\theta_{\not p})\rvert < 0.94$	8607	8737	8823	8790	8870	8261
$\cos(\not p, \mu) < 0.50$	8535	8559	8540	8399	8338	7669
2 jets, $E_i > 3$ GeV,no.ch.part. in $\text{jet}_i \geq 1$	7725	8142	8266	8214	8205	7600
$\cos(\text{jet}, \text{jet}) > -0.80$	7495	7669	7407	6652	5435	3185
Events with 3 jets	*5168*	*5704*	*5813*	*5452*	*4625*	*2747*
$\max(\cos(\text{jet}_i, \mu)) < 0.80$	*3616*	*4739*	*5070*	*5000*	*4412*	*2684*
$\sum \theta(\text{jet}_i, \text{jet}_j) < 300°$	*3608*	*4614*	*4730*	*4457*	*3638*	*2147*
Events with 2 jets only	*2327*	*1965*	*1594*	*1200*	*810*	*438*
$\max(\cos(\text{jet}_i, \mu)) < 0.80$	*1832*	*1753*	*1479*	*1142*	*800*	*437*
Total after preceding cuts	5440	6367	6209	5599	4438	2584
$m_{\text{jet}} > 1.8$ GeV	3885	5374	5614	5210	4184	2481

Table 6.5: Statistics of the cut-flow for the high mass analysis with signal events.

6.10 Sliding Cuts

To isolate each signal, sliding cuts were applied for the missing momentum and for the invariant mass, after both the low mass and high mass analysis. The cuts for missing momentum were applied at ±3.5 GeV around the theoretical values of p_ν, shown for each signal in the table in figure 6.2b. The same procedure was done for the invariant mass with a cut on m_{tot} at ±4 GeV around the sterile neutrino mass M_N. A sketch of the procedure is shown in figure 6.26.

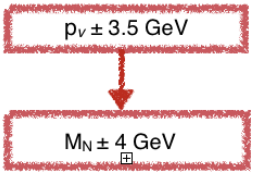

Figure 6.26: Sketch of the procedure of sliding cuts.

Sliding Cuts for Low Masses

The distributions of $\not{p}$ and m_{tot} from the LM analysis are shown in figure 6.27a and 6.27b, respectively, before the cuts were applied.

Zero background was optained for the 10 GeV and 20 GeV signal but a single $Z \to \tau^+\tau^-$ event remained for the 30 GeV signal. The specific event had the decay products:

$$Z \to \tau^+\tau^- \to \nu_\tau \pi^- \pi^0 \pi^0 + \bar{\nu}_\tau e^+ \nu_e + \gamma \text{ with } (\gamma \to \mu^+\mu^-)$$

In figure 6.28 a possible decay is illustrated in a Feynman diagram.

Sliding Cuts for High Masses

After all cuts were applied, all signals were background-free, except for the 80 GeV signal with three $Z \to q\bar{q}$ events. Of those three events, two of them were $c\bar{c}$ decays and the last a $b\bar{b}$ decay.

Statistics for Sliding Cuts

Since the 30 GeV signal was analysed in both the LM and HM analysis, efficiencies from the two analysis were combined. A total of 7302 events from the 30 GeV signal remained after all cuts in the LM analysis in presence of

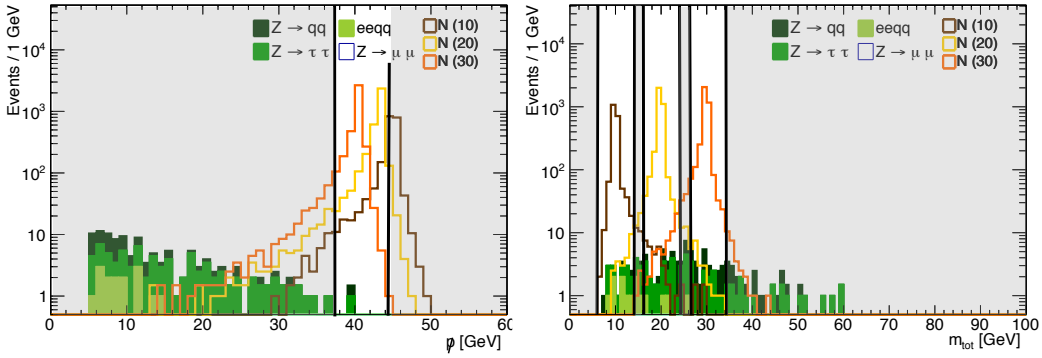

(a) **(b)**

Figure 6.27: Distributions of the sliding cut variables after the low mass analysis. The lines indicate the cuts and the shaded area indicate the discarded events. The sliding cuts were applied on the variables **(a)** missing momentum, and **(b)** the invariant mass. For the distribution in **(a)** the cuts for the separate masses overlap, hence only the cut for the 30 GeV signal is displayed for clarity.

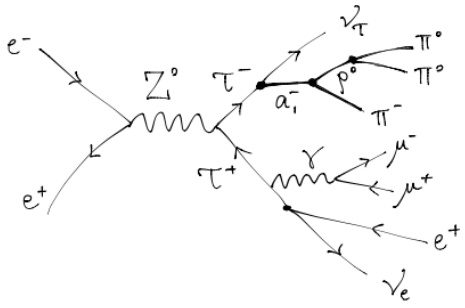

Figure 6.28: Feynman diagram of a possible decay of the remaining $\tau^+\tau^-$ background. In the hadronic τ decay, the intermediate W-bosons are left out for simplicity and mesons are drawn with a bold line.

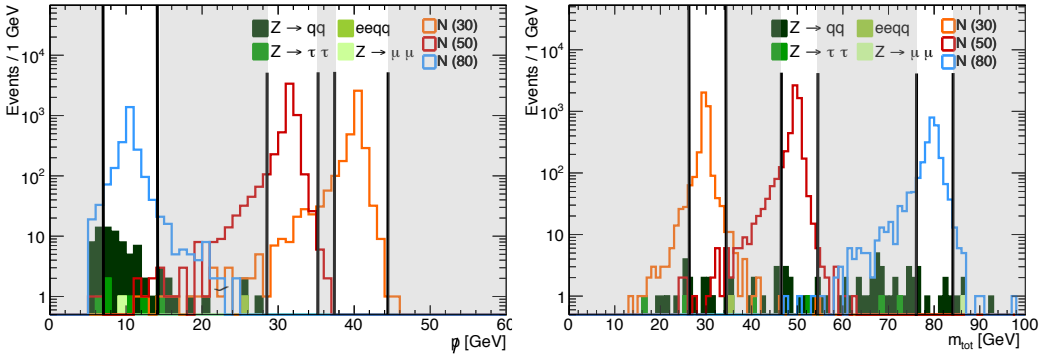

(a) **(b)**

Figure 6.29: Distributions of the sliding cut variables after the high mass analysis. The lines indicate the cuts and the shaded area indicate the discarded events. The sliding cuts were applied on the variables **(a)** missing momentum, and **(b)** the invariant mass.

one $\tau^+\tau^-$ background event. The HM analysis was background-free for the 30 GeV signal, with 3616 remaining signal events. 3522 of the same 30 GeV signal events appeared in both analysis, which gave a total of 7396 unique signal events for the combined 30 GeV signal.
Statistics for the sliding cuts applied on all signal samples are given in table 6.6.

As seen from table 6.6 the efficiency obtained for the short-lived sterile neutrino search is between 22 – 74%. The obtained efficiencies are compatible or better for all mass points than the efficiencies obtained at DELPHI, see figure 4.2b.

Process:	Signal	$Z \to q\bar{q}$	$Z \to \tau^+\tau^-$	$Z \to \mu^+\mu^-$	$e^+e^-q\bar{q}$	$q\bar{q}\mu\nu$
Initially produced:	10^4	10^8	$5 \cdot 10^6$	$5 \cdot 10^6$	$4.1801 \cdot 10^5$	14.01
N(10):						
$p_\nu \pm 3.5$ GeV	3826	1	0	0	0	0.0
$M_N \pm 4$ GeV	3725	0	0	0	0	0.0
N(20):						
$p_\nu \pm 3.5$ GeV	6881	1	1	0	0	0.003
$M_N \pm 4$ GeV	6776	0	0	0	0	0.0
N(30)LM:						
$p_\nu \pm 3.5$ GeV	*7418*	*2*	*4*	*0*	*0*	*0.011*
$M_N \pm 4$ GeV	*7302*	*0*	*1*	*0*	*0*	*0.007*
N(30)HM:						
$p_\nu \pm 3.5$ GeV	*3652*	*0*	*0*	*0*	*0*	*0.003*
$M_N \pm 4$ GeV	*3616*	*0*	*0*	*0*	*0*	*0.002*
N(30) combined:						
$M_N \pm 4$ GeV	7396	0	1	0	0	0.007
N(40):						
$p_\nu \pm 3.5$ GeV	5057	0	0	0	0	0.021
$M_N \pm 4$ GeV	4970	0	0	0	0	0.006
N(50):						
$p_\nu \pm 3.5$ GeV	5352	0	0	0	0	0.049
$M_N \pm 4$ GeV	5207	0	0	0	0	0.01
N(60):						
$p_\nu \pm 3.5$ GeV	4931	2	0	0	1	0.066
$M_N \pm 4$ GeV	4739	0	0	0	0	0.005
N(70):						
$p_\nu \pm 3.5$ GeV	3991	5	0	0	0	0.048
$M_N \pm 4$ GeV	3770	0	0	0	0	0.004
N(80):						
$p_\nu \pm 3.5$ GeV	2358	44	4	1	0	0.021
$M_N \pm 4$ GeV	2189	3	0	0	0	0.0

Table 6.6: Statistics for the cut-flow of the sliding cuts.

Chapter 7

Projected Sensitivity for Sterile Neutrinos Search at the FCC-*ee*

In the previous chapter an cut-based analysis was made for a Monte Carlo study of sterile neutrinos with short lifetimes at masses between 10 and 80 GeV. In this chapter the projected sensitivity of the search for short lived sterile neutrinos at the FCC-ee is derived from the results of this analysis followed by a discussion of the results.

7.1 Search Sensitivity

From the event selection, a background-free sample was optained for most of the signals samples. To compare results with DELPHI [1] a 2σ significance was chosen, calculated by the Gaussian approximation

$$Z = \frac{s}{\sqrt{b+s}} \geq 2. \tag{7.1}$$

Here s and b denote the number of signal and background events, respectively. To set a limit with 95% confidence level, at least 4 observed signal events were required for the background-free samples, at least 4.83 signal events for samples with one background event, and at least 6 observed signal events for samples with 3 background events. In order to obtain a

95% C.L., the required number of produced signal events, $N_{\text{sig}}^{\text{prod}}$, varies depending on the signal efficiency, ϵ_{sig}, with $N_{\text{sig}}^{\text{prod}} = N_{\text{sig}}^{\text{obs}}/\epsilon_{\text{sig}}$, where $N_{\text{sig}}^{\text{obs}}$ is the number of observed signal events. The values of observed signal events, required signal events produced, and the signal efficiency are given in table 7.1 together with the branching ratio for each signal.

The expression for the mixing angle of a sterile neutrino that only mixes with the muon flavour $|\theta_{\mu N}|^2$ is obtained using $BR(Z \to \nu N) = \Gamma(Z \to \nu N)/\Gamma_Z$ with the expression of $\Gamma(Z \to \nu N)$ from equation (2.30). The relation $BR(Z \to \bar{\nu}_\mu \mu q\bar{q}) = BR(Z \to \bar{\nu}_\mu N) \cdot BR(N \to \mu^\pm q\bar{q}')$ is used since only decay channels including a muon are considered and has a branching ratio on $BR(N \to \mu^\pm q\bar{q}') \simeq 0.5$, from equation (2.32).

$$|\theta_{\mu N}|^2 = \frac{3\sqrt{2}\pi}{G_F \cdot m_Z^3} \cdot \frac{1}{\Pi\left(\frac{M_N}{m_Z}\right)} \cdot \Gamma_Z \cdot \frac{BR(Z \to \bar{\nu}_\mu \mu q\bar{q})}{BR(N \to \mu^\pm q\bar{q}')} \tag{7.2}$$

From this expression, points in the parameter space M_N, $|\theta_{\mu N}|^2$ can be calculated in order to estimate a limit, with values given in table 7.1. The limit estimated from this analysis is projected with a 95% confidence level in conjunction with previous limits, shown in figure 7.1.

M_N [GeV]	ϵ_{sig} [%]	N_{bkg}	$N_{\text{obs}}^{\text{sig}}$	$N_{\text{prod}}^{\text{sig}}$	$BR(Z \to \nu N \to \mu^\pm q\bar{q})$	$\lvert\theta_{\mu N}\rvert^2$
10	37.3	0	4	10.7	$7.51 \cdot 10^{-8}$	$5.76 \cdot 10^{-7}$
20	67.8	0	4	5.9	$4.13 \cdot 10^{-8}$	$3.35 \cdot 10^{-7}$
30	74.0	1	4.83	6.5	$4.56 \cdot 10^{-8}$	$4.10 \cdot 10^{-7}$
40	49.7	0	4	8.1	$5.63 \cdot 10^{-8}$	$5.93 \cdot 10^{-7}$
50	52.1	0	4	7.7	$5.37 \cdot 10^{-8}$	$7.19 \cdot 10^{-7}$
60	47.4	0	4	8.4	$5.90 \cdot 10^{-8}$	$1.14 \cdot 10^{-6}$
70	37.7	0	4	10.6	$7.42 \cdot 10^{-8}$	$2.56 \cdot 10^{-6}$
80	21.9	3	6	27.4	$1.92 \cdot 10^{-7}$	$1.96 \cdot 10^{-5}$

Table 7.1: Table with values of the sterile neutrino masses, signal efficiency and number of remaining background events obtained from table 6.6. The number of observed signal events $N_{\text{prod}}^{\text{sig}}$ of $Z \to \bar{\nu}N$ with $N \to \mu^\pm q\bar{q}'$ is obtained from equation (7.1), and the number of required signal events produced is obtained from $N_{\text{obs}}^{\text{sig}}$ and the efficiency. The branching ratio of $Z \to \nu N \to \mu^\pm q\bar{q}$ is from the ratio $N_{\text{prod}}^{\text{sig}}/N_{\text{tot}}$ and the mixing angle $|\theta_{\mu N}|^2$ is obtained from equation (7.2).

Comparing the results to DELPHI [1], this study performs between 17 and 40 times better for the branching ratios, depending on the mass point.

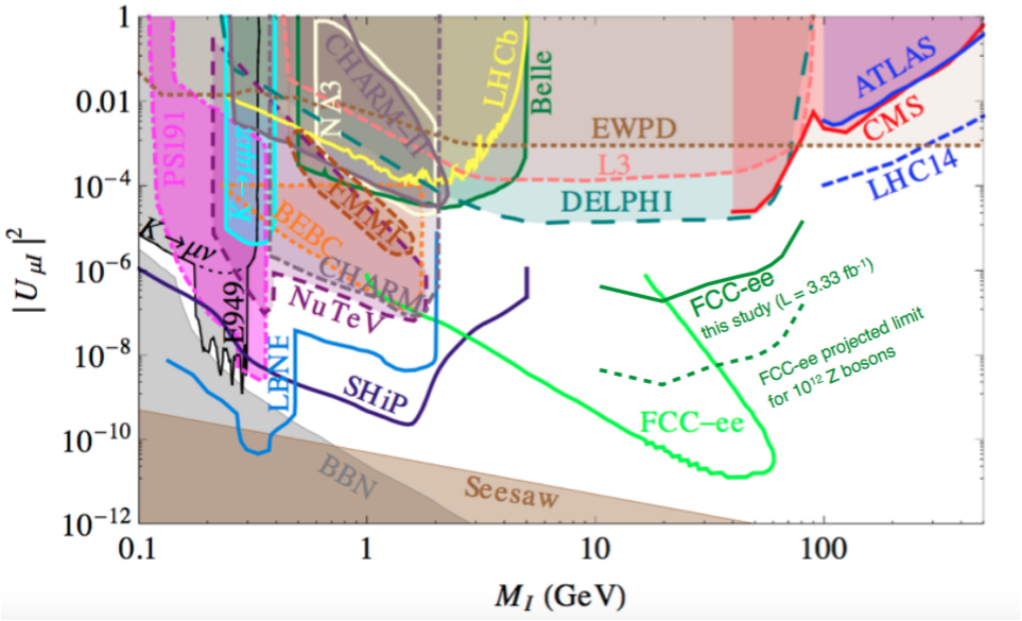

Figure 7.1: Sensitivity at 95% C.L. for the mixing angle $|\theta_{\mu N}|^2$ (here denoted $|U_{\mu I}|^2$), as function of the sterile neutrino mass M_N (here M_I), at the FCC-ee for sterile neutrinos with long lifetime (solid, light green) and sterile neutrinos with short lifetime (solid, green) in conjunction with previous limits. An extrapolated limit for sterile neutrinos with short lifetime in FCC-ee with 10^{12} Z bosons is drawn with a dashed green line.

A factor 30 is gained from the 30 times higher luminosity in this study compared to DELPHI. Since only one decay channel was chosen for this study, it was not sensitive to all decay channels, as DELPHI was, and thus a factor of two in difference from the branching ratio $BR(N \to \mu^{\pm} q\bar{q}') \simeq 0.5$ under the assumption of N mixing only via the ν_{μ}.

7.2 Discussion of Search for Sterile Neutrinos with Short Lifetime

The background estimate is one of the limiting factors for this analysis. An approach could be to cluster the correlated cuts, then estimate the selection factor for each uncorrelated sequence of cuts, and finally scale the background. A toy simulation with the estimated background and a Poisson distribution could then be made to obtain the uncertainty on the

background.

However, a better statistical precision would not necessary lead to a more accurate result, due to certain caveats with presumed systematic errors: The analysis relies on the generators, PYTHIA and WHIZARD, for very rare decays, which are not necessary the complete description, and relies on a rough detector parametrisation, with parameters not yet well determined. With these caveats, this analysis gives an estimate on a 95% CL limit for sterile neutrinos with short lifetime at a luminosity of $L = 3.33\ \text{fb}^{-1}$ at FCC-ee. In case of an analysis with real data, the Monte Carlo simulations would have been tuned to data.

A more rigid calculation of the results are calculated with Poissonian distribution and profile likelihood ratio in appendix A.2, and expose only a deviation on $2 - 3\%$. The simple and more straightforward Gaussian approximation is chosen for the calculations, due to the presumably relatively large systematic uncertainties.

Regarding the remaining three $Z \to q\bar{q}$ events, two of them were $c\bar{c}$ events and one $b\bar{b}$ event. This background could be reduced even more by flavour-tagging, as illustrated in figure 7.2, especially when considering that the signal has a very low probability of containing b quarks, due to the smallness of V_{cb} from the CKM-matrix. With the very efficient heavy flavour tagging as a modern detector in FCC-ee would have, a large amount of this background could potentially be removed. A similar procedure could be done for τ-tagging, to reduce that background. This strategy requires an assumption on very short lifetime of the sterile neutrino, since flavour tagging is evaluated from the time-of-flight of the particles in the vertex detector.

Through this preliminary study an estimate was made for the sensitivity of the sterile neutrino mixing angle $|\theta_{\mu N}|^2$ in the FCC-ee, obtained from the decay channel $N \to \mu q\bar{q}$. An analysis considering all possible decay modes of the sterile neutrino, hadronic, and leptonic, could potentially improve the limit almost by a factor two.

All together the projected limit from this study has potential of improvements, however with the caveat of the analysis is based on the current expertise of the generators PYTHIA and WHIZARD.

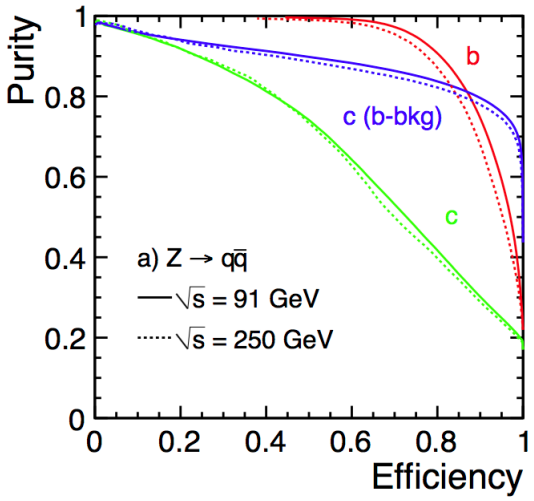

Figure 7.2: Flavour tagging performance for $Z \to q\bar{q}$ at $\sqrt{s} = 91$GeV and $\sqrt{s} = 250$GeV from [41].

7.3 Extrapolated Sensitivity for 10^{12} Z decays

In respect to the outlined production of 10^{12} Z bosons at the FCC-ee, corresponding to a factor 10^4 more events than generated for this study, a simple scaling was done in order to extrapolate the limit achieved in this study.

Assuming background-free samples for a factor 10^4 higher statistics would result in a scaling of the limit proportional to $1/N$ with a factor 10^4 better limit. This is though very(!) optimistic, especially considering the four-fermion background $e^+e^- \to q\bar{q}\mu\nu$, that with a factor 10^4 becomes, for this analysis, an irreducible background. Even though the $e^+e^- \to q\bar{q}\mu\nu$ background is reduced by 99.986% – 99.936%, it is not adequate to achieve a background-free sample with a factor 10^4 higher luminosity. As seen in figure 6.17a and 6.17b, the distributions for missing momentum and reconstructed mass are relatively flat. With sufficient signal events, a peak would form around its given mass and missing momentum.

When assuming irreducible background, a more realistic but perhaps slightly conservative scaling by $1/\sqrt{N}$ would result in a factor 100 better limit, as shown in figure 7.1. The analysis could possibly be optimised and potentially give a better limit than that.

Chapter 8

Conclusion

In this preliminary study, the first part outlined how the Neutrino Minimal Standard Model, *νMSM*, provides an extension to the Standard Model (SM), by explaining phenomena yet unexplained by the SM, neutrino oscillations, dark matter, and baryon asymmetry. In the *νMSM*, three heavy, sterile, right-handed neutrinos are added to the Standard Model with almost no coupling to matter, and only couple through a small mixing angle θ to the active left-handed neutrinos.

The FCC-ee, a proposed future circular e^+e^- collider, is expected to produce 10^{12} Z bosons during the time of operation. With this large amount of statistics, very rare events can be probed, as for this study, sterile neutrinos. The sensitivity to sterile neutrinos in the FCC-ee was explored with two main studies, one for long lived sterile neutrinos, and one for short lived.

In the study for long lived sterile neutrinos, the expected limit for the mixing angle $|\theta|^2$ was computed with a 95 % confidence level in the mass range $10 - 80$ GeV. Based on the discussion in section 5.1 the background is negligible for this search. FCC-ee has prospects of setting limits or finding sterile neutrinos with mixing angles $|\theta|^2$ down to 10^{-11}.

For the short lived sterile neutrinos a Monte Carlo study was performed. Background samples were generated corresponding to a total of $1.43 \cdot 10^8$ Z events at a center of mass energy at 91.2 GeV, corresponding to a luminosity of 3.33 fb^{-1}. Two cut-based analyses were made, one for low masses at $10 - 30$ GeV, and one for high masses at $30 - 80$ GeV. For all of the eight signal samples (10, 20, 30, 40, 50, 60, 70, and 80 GeV), except two, background-free samples were obtained. The contributing backgrounds

were $Z \to \tau^+\tau^-$ (1 event) and $Z \to q\bar{q}$ (3 events). For this study 95 % C.L. was reached at a mixing angle on $|\theta_{\mu N}|^2 \sim 10^{-7} - 10^{-6}$ for all masses, corresponding to a branching ratio on $BR(Z \to \nu N)$ with $N \to \mu q\bar{q}$ on $\sim 10^{-8}$. For the 80 GeV signal the limit was decreased to $|\theta_{\mu N}|^2 \sim 10^{-5}$, due to constraints by the phase space and by the hard discrimination of signal versus background.

The search reach for short lived sterile neutrinos, based on the Monte Carlo study, is almost two order of magnitude better than the current best limit for the same mass range, obtained by DELPHI. The result is summarised in figure 7.1.

The statistics of Z bosons expected from the FCC-ee is four orders of magnitude larger than the statistics generated in the Monte Carlo study for the short lived sterile neutrino analysis. With this amount of statistics, the four-fermion background $q\bar{q}\mu\nu$ becomes an irreducible background (see table 6.6). With sizable background the limit scales with $1/\sqrt{N}$, where N is number of events. With this conservative estimate and 10^{12} Z bosons the limit would scale by a factor 100. Suggestions for improvements of the analysis are discussed in section 7.2 in order to gain an even better limit.

Appendix

A.1 Generation of signal in PYTHIA

For generation of signal events in PYTHIA, all strings are parsed to `pythia.readString()`. The `id:new` and `addChannel` function is given the following parameters, where the branching ratio, `bRatio`, is calculated due to the CKM-matrix for all quarks except for the top quark:

$$BR(W^+ \to q_i q_j) = \frac{|V_{ij}|^2}{\sum_{i,j} |V_{ij}|^2}$$

```
id:new = name antiName spinType chargeType colType m0 mWidth mMin mMax tau0
         isResonance mayDecay doExternalDecay isVisible doForceWidth

id:addChannel = onMode bRatio meMode product1 product2 ....
```

Generation of signal:

```
"WeakSingleBoson:ffbar2gmZ = on";
"5000000:new = N2 N2 2 0 0 xx. 0.0 0.0 0.0 0.0 0 1 0 1 0";
"5000000:isResonance = false";
"5000000:addChannel = 1 0.4652853137 91 -1 2 13";      // Du mu
"5000000:addChannel = 1 0.2477664259e-1 91 -3 2 13";   // Su mu
"5000000:addChannel = 1 0.8201559847e-5 91 -5 2 13";   // Bu mu
"5000000:addChannel = 1 0.2372986153e-1 91 -1 4 13";   // Dc mu
"5000000:addChannel = 1 0.4853957884 91 -3 4 13";      // Sc mu
"5000000:addChannel = 1 0.8041922597e-3 91 -5 4 13";   // Bc mu
```

```
"5000000:mayDecay = on");
"23:onMode = off");
"23:addchannel = 1 1. 103 12 5000000");
```

A.2 Results calculated with Poisson statistics and profile likelihood ratio

From the event selection, a background-free sample was optained for most of the signals samples. Considering fluctuations from the low statistics, the few background events are expected to follow a Poissonian distribution. For events with 0 background events, less than 3 background events are expected with 95% confidence, for 1 background event; 4.74, and for 3 background events, less than 7.75 events are expected [57]. To compare results with DELPHI [1] a 2σ significance was chosen, calculated by:

$$Z = \sqrt{2\left((s+b)\cdot \ln(1+\frac{s}{b}) - s\right)} \geq 2 \tag{A.1}$$

Based on profile likelihood ratio from [58], where s and b are number of signal and background events. The required number of produced signal events varies depending on the signal efficiency, $N_{sig}^{gen} = N_{sig}^{obs}/\epsilon_{sig}$, which values are given in table A.1 together with the branching ratio for each signal.

The expression for the mixing angle between the sterile neutrino mixing and the muon flavour $|\theta_{\mu N}|^2$ is obtained using $BR(Z \to \nu N) = \Gamma(Z \to \nu N)/\Gamma_Z$ with the expression of $\Gamma(Z \to \nu N)$ from equation (2.30). The relation $BR(Z \to \bar{\nu}_\mu \mu q\bar{q}) = BR(Z \to \bar{\nu}_\mu N) \cdot BR(N \to \mu^\pm q\bar{q}')$ is used since only decay channels including a muon are considered and has a branching ratio on $BR(N \to \mu^\pm q\bar{q}') \simeq 0.5$ obtained from figure 2.6.

$$|\theta_{\mu N}|^2 = \frac{3\sqrt{2}\pi}{G_F \cdot m_Z^3} \cdot \frac{1}{\Pi\left(\frac{M_N}{m_Z}\right)} \cdot \Gamma_Z \cdot \frac{BR(Z \to \bar{\nu}_\mu \mu q\bar{q})}{BR(N \to \mu^\pm q\bar{q}')}, \tag{A.2}$$

from which points in the parameter space M_N, $|\theta_{\mu N}|^2$ can be calculated in order to estimate a limit. Values are given in table A.1.

M_N [GeV]	ϵ_{sig} [%]	N_{bkg}	$N^{\text{sig}}_{\text{obs}}$	$N^{\text{sig}}_{\text{prod}}$	$BR(Z \to \nu N \to \mu^{\pm} q\bar{q})$	$\lvert\theta_{\mu N}\rvert^2$
10	37.3	0	3	11.0	$7.66 \cdot 10^{-8}$	$5.88 \cdot 10^{-7}$
20	67.8	0	3	6.0	$4.22 \cdot 10^{-8}$	$3.42 \cdot 10^{-7}$
30	74	1	4.74	6.7	$4.71 \cdot 10^{-8}$	$4.23 \cdot 10^{-7}$
40	49.7	0	3	8.2	$5.74 \cdot 10^{-8}$	$6.05 \cdot 10^{-7}$
50	52.1	0	3	7.8	$5.48 \cdot 10^{-8}$	$7.34 \cdot 10^{-7}$
60	47.4	0	3	8.6	$6.02 \cdot 10^{-8}$	$1.16 \cdot 10^{-6}$
70	37.7	0	3	10.8	$7.57 \cdot 10^{-8}$	$2.61 \cdot 10^{-6}$
80	21.9	3	7.75	28.3	$1.98 \cdot 10^{-7}$	$2.03 \cdot 10^{-5}$

Table A.1: Table with values of the sterile neutrino masses, signal efficiency and number of remaining background events obtained from table 6.6. The number of observed signal events $N^{\text{sig}}_{\text{prod}}$ of $Z \to \bar{\nu}N$ with $N \to \mu^{\pm} q\bar{q}'$ is obtained from equation (A.1) based on Poisson statistics and profile likelihood ratio, and the number of required signal events produced is obtained from $N^{\text{sig}}_{\text{obs}}$ and the efficiency. The branching ratio of $Z \to \nu N \to \mu^{\pm} q\bar{q}$ is from the ratio $N^{\text{sig}}_{\text{prod}}/N_{\text{tot}}$ and the mixing angle $|\theta_{\mu N}|^2$ is obtained from equation (7.2).

Bibliography

[1] DELPHI collaboration. **Search for Neutral Heavy Leptons Produced in Z Decays**. *Z. Phys.*, C74:57–71, 1997. [Erratum: Z. Phys.C75,580(1997)].

[2] Sheldon L Glashow. **Partial-symmetries of weak interactions**. *Nuclear Physics*, 22(4):579–588, 1961.

[3] Abdus Salam. **Weak and Electromagnetic Interactions**. *Conf. Proc.*, C680519:367–377, 1968.

[4] Steven Weinberg. **A model of leptons**. *Physical review letters*, 19(21):1264, 1967.

[5] Mark Thomson. ***Modern particle physics***. Cambridge University Press, 2013.

[6] Particle Data Group. **Review of Particle Physics**. *Chin. Phys.*, C40(10):100001, 2016.

[7] Max Baak et al. **GFitter**. 2008 (accessed 19.08.2017). http://gfitter.desy.de/Standard_Model/.

[8] QR Ahmad et al. **Measurement of the Rate of $\nu + d \rightarrow p + p + e^-$ Interactions Produced by ^8B Solar Neutrinos at the Sudbury Neutrino Observatory**. *Physical Review Letters*, 87(7):071301, 2001.

[9] Gianfranco Bertone, Dan Hooper, and Joseph Silk. **Particle dark matter: Evidence, candidates and constraints**. *Physics Reports*, 405(5):279–390, 2005.

[10] Laurent Canetti et al. **Dark matter, baryogenesis and neutrino oscillations from right-handed neutrinos**. *Physical Review D*, 87(9):093006, 2013.

[11] Bruce T. Cleveland et al. **Measurement of the Solar Electron Neutrino Flux with the Homestake Chlorine Detector**. *The Astrophysical Journal*, 496(1):505, 1998. http://stacks.iop.org/0004-637X/496/i=1/a=505.

[12] Super-Kamiokande Collaboration. **Evidence for Oscillation of Atmospheric Neutrinos**. *Phys. Rev. Lett.*, 81:1562–1567, Aug 1998. https://link.aps.org/doi/10.1103/PhysRevLett.81.1562.

[13] MINOS Collaboration. **Measurement of Neutrino Oscillations with the MINOS Detectors in the NuMI Beam**. *Phys. Rev. Lett.*, 101:131802, Sep 2008. https://link.aps.org/doi/10.1103/PhysRevLett.101.131802.

[14] KamLAND Collaboration. **Publisher's Note: Precision Measurement of Neutrino Oscillation Parameters with KamLAND [Phys. Rev. Lett. 100, 221803 (2008)]**. *Phys. Rev. Lett.*, 101:259901, Dec 2008. https://link.aps.org/doi/10.1103/PhysRevLett.101.259901.

[15] Particle Data Group. **Chapter 14: Neutrino Mixing**. *Chin. Phys.*, C40:100001, (2016) and 2017 update.

[16] Kismalac. **Neutrino mass hierarchy**. 2011 (accessed 07.09.2017). https://commons.wikimedia.org/wiki/File:NeutrinoHierarchy.svg.

[17] Peter AR Ade et al. **Planck 2015 results-XIII. Cosmological parameters**. *Astronomy & Astrophysics*, 594:A13, 2016.

[18] The SLD Electroweak, Heavy Flavour Groups, ALEPH Collaboration, DELPHI Collaboration, L3 Collaboration, OPAL Collaboration, SLD Collaboration, and LEP Electroweak Working Group. **Precision electroweak measurements on the Z resonance**. *Physics Reports*, 427(5):257–454, 2006.

[19] C Jarlskog. **Neutrino counting at the Z-peak and right-handed neutrinos**. *Physics Letters B*, 241(4):579–583, 1990.

[20] Peter Minkowski. $\mu \to e\gamma$ **at a rate of one out of 109 muon decays?** *Physics Letters B*, 67(4):421–428, 1977.

[21] Rabindra N. Mohapatra and Goran Senjanović. **Neutrino Mass and Spontaneous Parity Nonconservation**. *Phys. Rev. Lett.*, 44:912–915, Apr 1980.

[22] Takehiko Asaka, Steve Blanchet, and Mikhail Shaposhnikov. **The νMSM, dark matter and neutrino masses**. *Physics Letters B*, 631(4):151–156, 2005.

[23] SN Gninenko, DS Gorbunov, and ME Shaposhnikov. **Search for GeV-scale sterile neutrinos responsible for active neutrino oscillations and baryon asymmetry of the Universe**. *Advances in High Energy Physics*, 2012, 2012.

[24] Carlo Giunti and Marco Laveder. **Neutrino mixing**. *arXiv preprint hep-ph/0310238*, 2003.

[25] Alexey Boyarsky, Oleg Ruchayskiy, and Mikhail Shaposhnikov. **The role of sterile neutrinos in cosmology and astrophysics**. *Annual Review of Nuclear and Particle Science*, 59:191–214, 2009.

[26] Georges Aad et al. **Observation of a new particle in the search for the Standard Model Higgs boson with the ATLAS detector at the LHC**. *Physics Letters B*, 716(1):1–29, 2012.

[27] CMS collaboration. **Observation of a new boson at a mass of 125 GeV with the CMS experiment at the LHC**. *arXiv preprint arXiv:1207.7235*, 2012.

[28] Fedor Bezrukov and Mikhail Shaposhnikov. **Standard Model Higgs boson mass from inflation: Two loop analysis**. *Journal of High Energy Physics*, 2009(07):089, 2009.

[29] Stefan Antusch and Oliver Fischer. **Testing sterile neutrino extensions of the Standard Model at future lepton colliders**. *arXiv preprint arXiv:1502.05915*, 2015.

[30] Alain Blondel, E Graverini, N Serra, and M Shaposhnikov. **Search for Heavy Right Handed Neutrinos at the FCC-ee**. *arXiv preprint arXiv:1411.5230*, 2014.

[31] Michael Gronau, C. N. Leung, and Jonathan L. Rosner. **Extending limits on neutral heavy leptons**. *Physical Review D*, 29:2539, 1 June 1984.

[32] M Bicer et al. **First look at the physics case of TLEP**. *Journal of High Energy Physics*, 2014(1):164, 2014.

[33] FCC ee collaboration. **The FCC-ee design study**. accessed 01.08.2017. http://tlep.web.cern.ch.

[34] S Dawson et al. **Higgs working group report of the Snowmass 2013 community planning study**. *arXiv preprint arXiv:1310.8361*, 2013.

[35] Ilaria Brivio and Michael Trott. **The Standard Model as an effective field theory**. *arXiv preprint arXiv:1706.08945*, 2017.

[36] Brian Henning, Xiaochuan Lu, and Hitoshi Murayama. **How to use the Standard Model effective field theory**. *Journal of High Energy Physics*, 2016(1):23, 2016.

[37] Patrick Janot. **Academic Training: Physics Perspectives for a Future Circular Collider: FCC-ee**. 2017. https://indico.cern.ch/event/666889/.

[38] SuperKEKB collaboration. **SuperKEKB Project**. accessed 06.12.2017. http://www-superkekb.kek.jp.

[39] Christian Lippman. **ALICE matters**. 2012, (accessed 28.08.2017). http://alicematters.web.cern.ch/?q=Lip_PID.

[40] CLIC collaboration. **CLIC detector**. accessed 01.08.2017. http://clicdp.web.cern.ch/content/clic-detector.

[41] Ties Behnke et al. **The international linear collider technical design report-volume 4: detectors**. Technical report, 2013. http://www.linearcollider.org/ILC/Publications/Technical-Design-Report.

[42] Lucie Linssen et al. **Physics and detectors at CLIC: CLIC conceptual design report**. *arXiv preprint arXiv:1202.5940*, 2012.

[43] Sergey Alekhin et al. **A facility to Search for Hidden Particles at the CERN SPS: the SHiP physics case**. *Reports on Progress in Physics*, 79(12):124201, 2016.

[44] Stefan Antusch, Eros Cazzato, and Oliver Fischer. **Displaced vertex searches for sterile neutrinos at future lepton colliders**. *arXiv preprint arXiv:1604.02420*, 2016.

[45] Joseph A Formaggio and GP Zeller. **From eV to EeV: Neutrino cross sections across energy scales**. *Reviews of Modern Physics*, 84(3):1307, 2012.

[46] M Honda et al. **Atmospheric neutrino flux calculation using the NRLMSISE-00 atmospheric model**. *Physical Review D*, 92(2):023004, 2015.

[47] N. J. Baker et al. **Total cross sections for $\nu_\mu n$ and $\nu_\mu p$ charged-current interactions in the 7-foot bubble chamber**. *Phys. Rev. D*, 25:617–623, Feb 1982. https://link.aps.org/doi/10.1103/PhysRevD.25.617.

[48] D.S. Baranov et al. **Deep inelastic neutrino interactions in the bubble chamber skat at 2–30 GeV**. *Physics Letters B*, 81(2):258 – 260, 1979. http://www.sciencedirect.com/science/article/pii/0370269379905379.

[49] S. Ciampolillo et al. **Total cross section for neutrino charged current interactions at 3 GeV and 9 GeV**. *Physics Letters B*, 84(2):281 – 284, 1979. http://www.sciencedirect.com/science/article/pii/0370269379903034.

[50] SciBooNE Collaboration. **Measurement of inclusive charged current interactions on carbon in a few-GeV neutrino beam**. *Phys. Rev. D*, 83:012005, Jan 2011. https://link.aps.org/doi/10.1103/PhysRevD.83.012005.

[51] S. Mrenna T. Sjöstrand and P. Skands. **PYTHIA 8.1**. *JHEP05 (2006) 026, Comput. Phys. Comm. 178 (2008) 852*.

[52] Wolfgang Kilian, Thorsten Ohl, and Jürgen Reuter. **WHIZARD—simulating multi-particle processes at LHC and ILC**. *The European Physical Journal C-Particles and Fields*, 71(9):1–29, 2011.

[53] Matt Dobbs and Jorgen Beck Hansen. **The HepMC C++ Monte Carlo event record for High Energy Physics**. *Comput. Phys. Commun.*, 134:41–46, 2001.

[54] Matteo Cacciari, Gavin P Salam, and Gregory Soyez. **FastJet user manual**. *The European Physical Journal C*, 72(3):1896, 2012.

[55] Colin Bernet and Benedikt Hegner. **FCC software**. 2016 (accessed (11.07.2017). https://github.com/HEP-FCC/fcc-tutorials/blob/master/FccSoftwareGettingStartedFastSim.md.

[56] Torbjörn Sjöstrand. **High-energy-physics event generation with PYTHIA 5.7 and JETSET 7.4**. *Computer Physics Communications*, 82(1):74–89, 1994.

[57] Roger J Barlow. ***Statistics: a guide to the use of statistical methods in the physical sciences***. John Wiley & Sons, 1989.

[58] Glen Cowan and Eilam Gross. **Discovery significance with statistical uncertainty in the background estimate**. 2008. http://www.pp.rhul.ac.uk/~{}cowan/stat/notes/SigCalcNote.pdf.